The first analysis of very-high-energy gamma rays from the Large Magellanic Cloud with a novel analysis technique

Die erste Analyse
sehr hoch energetischer Gammastrahlung
aus der Großen Magellanschen Wolke
mit einer neuartigen Analysetechnik

Der Naturwissenschaftlichen Fakultät
der Friedrich-Alexander-Universität Erlangen-Nürnberg
zur Erlangung des Doktorgrades Dr. rer. nat.

vorgelegt von
Domenico Tiziani
aus Fürth

Als Dissertation genehmigt von
der Naturwissenschaftlichen Fakultät der
Friedrich-Alexander-Universität Erlangen-Nürnberg

Tag der mündlichen Prüfung:	30.10.2020
Vorsitzender der Promotionkommission:	Prof. Dr. Wolfgang Achziger
Erstberichterstatter:	Prof. Dr. Christopher van Eldik
Zweitberichterstatter:	Prof. Dr. Manami Sasaki

Abstract

The Cherenkov Telescope Array (CTA) represents the next generation of instruments for the measurement of gamma radiation from galactic and extragalactic sources in the range between several tens of GeV to few hundred TeV. It will consist of two arrays of different types of Imaging Atmospheric Cherenkov Telescopes (IACT) at two sites and is currently in a pre-construction phase. One important calibration of an IACT is the pointing, which is necessary for a precise angular reconstruction of gamma-ray signals.

The first part of this thesis introduces the SingleCCD concept, the favoured pointing solution for the medium size telescopes of CTA. This method makes use of an optical CCD camera that is mounted to a telescope and that records images of the night sky and the Cherenkov light detector. These images can be used for precise measurements of the alignment of the telescope and its internal deformations.

The results of extensive tests of this method are presented together with a new software solution that can be used the analysis of the recorded CCD images. With the help of simulations and a test setup at an operating IACT, it could be shown that the introduced software provides an efficient way to reach pointing precisions of $< 10''$.

In the second part of the thesis, the 3D likelihood method is used for the analysis of gamma radiation from the Large Magellanic Cloud (LMC) that was observed with H.E.S.S., a contemporary IACT located in Namibia. The application of the 3D likelihood method in the analysis of IACT data is rather novel but is on the rise with the upcoming CTA and provides a straightforward way of analysing complicated regions with overlapping gamma-ray sources.

In the analysis, spatial and spectral descriptions of the known point sources in the LMC were obtained that are, within some limitations, compatible with results of earlier analyses with more established methods. Furthermore, the advantages of the 3D likelihood method were used to search for a diffuse gamma-ray signal within the LMC. Indication for this was found within the 30 Doradus region, spatially coincident with emission at lower gamma-ray energies that was detected by the spaceborne gamma-ray telescope Fermi-LAT.

Zusammenfassung

Das Cherenkov Telescope Array (CTA) repräsentiert die nächste Generation von Instrumenten zur Messung von Gammastrahlung von galaktischen und extragalaktischen Quellen im Bereich von einigen zehn GeV bis zu wenigen hundert TeV. Es wird aus zwei Anordnungen von unterschiedlichen Typen von Abbildenden Cherenkov Teleskopen (IACT) an zwei Standorten bestehen und befindet sich aktuell in einer Voraufbau Phase. Ein wichtiger Aspekt der Kalibrierung solcher Teleskope ist das Pointing, welches für die präzise räumliche Rekonstruktion von Gammastrahlungssignalen wichtig ist.
Im ersten Teil der vorliegenden Arbeit wird das SingleCCD Konzept vorgestellt, welches die bevorzugte Lösung für das Pointingproblem der mittelgroßen CTA-Teleskope darstellt. In dieser Methode wird eine optische CCD-Kamera genutzt, die so am Teleskop montiert ist, dass sie Bilder vom Nachthimmel und vom Cherenkovlichtdetektor aufnehmen kann. Die so gewonnenen Fotos können für präzise Messungen der Ausrichtung des Teleskops und seiner internen Verformungen genutzt werden.
Die Ergebnisse ausführlicher Tests dieser Methode werden gemeinsam mit einer neuen Software vorgestellt, welche für die Auswertung der Fotos genutzt werden kann. Mithilfe von Simulationen und einem Testaufbau an einem momentan operierenden IACT konnte gezeigt werden, dass die vorgestellte Software eine effiziente Möglichkeit darstellt, Präzisionen $< 10''$ zu erreichen.
Im zweiten Teil der Arbeit wird die Anwendung der 3D-Likelihood-Methode bei der Analyse von Gammastrahlung von der Großen Magellanschen Wolke (GMW) präsentiert. Die Daten dafür wurden mit H.E.S.S. genommen, einem aktuellen IACT das sich in Namibia befindet. Die Verwendung der 3D-Likelihood-Methode bei der Analyse von IACT-Daten stellt einen neuartigen Ansatz dar, der allerdings, vor allem für zukünftige CTA-Daten, immer mehr an Bedeutung gewinnt und eine geradlinige Möglichkeit bietet, komplizierte Himmelsregionen mit sich gegenseitig überlappenden Quellen zu analysieren.
In der Analyse ergaben sich positionelle und spektrale Beschreibungen der bekannten Punktquellen in der GMW, die bis auf einige Einschränkungen mit den Ergebnissen bisheriger Analysen mit etablierten Methoden vereinbar sind. Ferner wurden die Vorteile der 3D-Likelihood-Methode genutzt, um die GMW nach Signalen diffuser Gammastrahlung zu untersuchen. Hinweise auf ein solches Signal wurden in einem Bereich der 30 Doradus Region gefunden, räumlich koinzident mit einem vom satellitengestützten Gammastrahlenteleskop Fermi-LAT bei niedrigeren Photonenenergien detektierten Signal.

Contents

1 Astrophysics of cosmic rays and cosmic gamma rays **9**

1.1 The detection of cosmic rays 9

1.2 Generation of cosmic gamma rays 10

1.3 Acceleration mechanisms of relativistic particles 12

1.4 Astrophysical sources of gamma rays 14

2 Imaging Atmospheric Cherenkov Telescopes **19**

2.1 Detection principle 19

2.2 Two gamma-ray instruments 21

2.3 Components of IACTs 23

2.4 Low level analysis of IACT data 27

2.5 High level analysis of IACT data 31

3 A pointing solution for the MST **43**

3.1 Reasons for mis-pointing 43

3.2 Pointing at H.E.S.S. 44

3.3 The SingleCCD concept 45

3.4 Camera hardware 47

3.5 Thermal tests of the housing 49

3.6 Long term test at MAGIC telescope 53

3.7 Summary 55

4 Pointing image analysis **57**

4.1 Functionality of libPointingMST 58

4.2 Verification of libPointingMST with simulated data 67

4.3 Analysis of the test campaign at MAGIC 72

4.4 Conclusion 82

5 3D likelihood analysis of the Large Magellanic Cloud 85

5.1 Introduction to the region 86

5.2 Data selection 89

5.3 Modelling of point sources 91

5.4 Analysis of residuals 94

5.5 Search for diffuse emission 97

5.6 Limits of the analysis 99

5.7 Conclusion 102

Introduction

Astronomy, from Greek αστρονομια (which literally translates to "law of stars"), is a part of natural science that deals with the understanding of phenomena outside of the Earth's atmosphere. Despite its translation to English, this not only includes studies of stars, but also of other astrophysical objects like e.g. galaxy clusters, neutron stars, black holes, and supernovae. To carry out these studies, scientists have invented more and more advanced instruments to make use of the different messenger signals that originate from sources of interest and that can be detected at Earth. A part of these messengers is massive. Their scales range from macroscopic objects called meteorites over heavy atomic nuclei down to subatomic particles like protons and electrons. The highly energetic particles are also called cosmic rays. Even astrophysical neutrinos have been detected. Another field of astronomical research has become very popular over the last years with the first measurements of gravitational waves. Apart from the above described messengers, the whole range of the electromagnetic spectrum is being exploited by scientists. Having originally started with observations in the part of the spectrum that is visible to the human eye, astronomers came up with instruments that could extend the accessible wavelength band. Infrared, microwave, and radio detectors have been built to investigate larger wavelengths and therefore lower photon energies. To account for higher energies, ultraviolet, x-ray, and gamma-ray telescopes have been developed. The high energetic gamma-rays are of special interest because they can not be produced thermally but only in particle processes in the vicinity of astrophysical sources involving cosmic rays. Gamma-ray signals can be used for studying the origin of cosmic rays due to the fact that the electrically neutral gamma rays are not deflected by interstellar magnetic fields in contrast to the charged cosmic rays. Since the Earth's atmosphere is in-transparent for gamma rays, it is not possible to measure these high energetic photons directly at ground level. One possibility to circumvent this fact is to deploy a suitable detector to an orbit around Earth. Given the fact that the active volume that can be deployed on a satellite is limited to few cubic meters due to technical reasons, these kinds of detectors are only suitable for studies of the lower-energetic gamma-rays. This energy range is usually referred to as the high-energy (HE) domain that ranges from several MeV to several hundreds of GeV. The very-high-energy (VHE) domain, that follows the HE domain, is not accessible to these instruments as the flux of higher energetic photons decreases rapidly with increasing energy. One technique that enables scientists to study the VHE energy range represent the so called "Imaging Air Cherenkov Telescope" (IACT) technique. This type of telescope uses the Earth's atmosphere itself

as detector volume and images the Cherenkov light that is produced upon entry of gamma-ray photons. After first experiments with different instruments dating back to the 1950's [Galbraith et al. 1953], the first detection of a cosmic gamma-ray source was accomplished with the Whipple telescope [Weekes et al. 1989]. This system and other second generation instruments like HEGRA [Mirzoyan et al. 1994] and CAT [Barrau et al. 1998] did pioneer work in further developing the IACT technique. Currently, third generation Cherenkov telescopes are in operation and have proven to be very successful in detecting new gamma-ray sources. Mainly thanks to H.E.S.S., MAGIC, and VERITAS, more than 200 emitters of cosmic gamma-rays are known. In the early days of these experiments, researchers also came up with the idea of a major instrument to be built by practically all gamma-ray astronomers together, making use of their combined expertise. This project, representing the fourth generation of IACTs, was given the name CTA, the Cherenkov Telescope Array. This instrument will be composed of multiple telescopes of varying sizes, each specially designed for the measurement of a specific range of the complete energy spectrum.
One important aspect in the calibration of an IACT is the pointing. This term describes the ability to transform a position in the focal plane of a telescope to a sky position. For the different experiments, various ways have been invented to perform this calibration which is crucial for a precise determination of the spatial origin of measured gamma-rays. Mechanical imperfections of the telescope structure make this calibration a nontrivial task. The favoured pointing solution for the medium size telescopes (MSTs) of CTA is the so called SingleCCD pointing concept. This technique makes use of one optical CCD camera that is attached to a telescope and that takes images which are used to derive the necessary pointing information. In the first main part of this thesis, the adoption of the SingleCCD pointing concept is described and extensive tests of pointing hardware and software are discussed.
The second main part of this thesis is dedicated to the analysis of VHE gamma rays from the Large Magellanic Cloud (LMC) detected with H.E.S.S. The analysis was carried out with the 3D likelihood technique whose application is rather novel for data from an IACT. The LMC is a dwarf galaxy that part of the Local Group of galaxies and close to our own galaxy, the Milky Way.

Chapter 1

Astrophysics of cosmic rays and cosmic gamma rays

This chapter gives an introduction to cosmic-ray astrophysics. In the first two sections, the phenomenon of the cosmic radiation and its connection to gamma-ray astronomy is presented. In the third section, the theory of diffusive shock acceleration is described. Some types of astrophysical objects that produce gamma radiation are discussed in the last section.
As main references, Longair [2011] and F. A. Aharonian [2004] were used.

1.1 The detection of cosmic rays

The history of cosmic-ray physics started when ionising radiation was detected in a series of manned balloon flights by Hess [1912]. This ionising radiation increases with increasing altitude and can therefore not be explained by terrestrial radioactivity. It was concluded that the signal could only originate from above the Earth's atmosphere. Auger et al. [1939] showed that the incoming radiation produces extensive showers of secondary particles in the air, which could reach transversal sizes of more than 100 m on the ground. Later, the signal of these secondary particles but also the newly developed technique of deploying artificial satellites into the Earth's orbit where used to study the cosmic rays further.
It was discovered that the ionising effects were caused by high energetic particles. Due to historic reasons, these particles that mainly consist of protons ($\sim 85\,\%$), helium nuclei ($\sim 12\,\%$), nuclei of heavier elements ($\sim 1\,\%$), and electrons ($\sim 2\,\%$) are still called *cosmic rays* or *cosmic radiation*. The differential energy spectrum, meaning the frequency of occurrence $N(E)$ of cosmic rays per energy interval $\mathrm{d}E$, follows a power law in the energy range between $10^9\,\mathrm{eV}$ and $10^{20}\,\mathrm{eV}$:

$$N(E)\mathrm{d}E \propto E^{-x}\mathrm{d}E. \tag{1.1}$$

The spectral index x is approximately 2.7 up to an energy of $\sim 10^{15}\,\mathrm{eV}$ and changes to a higher value of ~ 3.1 at this point, which is called the *knee*. At the so-called *ankle*

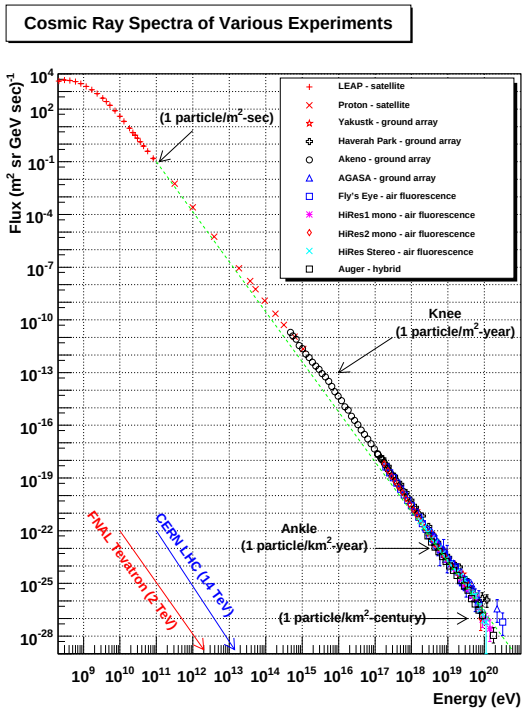

Figure 1.1: Differential energy spectrum of all cosmic-rays particles measured with different experiments. The spectral break features named *knee* and *ankle* are marked as well as energies that can be reached in current collider experiments. Image credit: W. Hanlon `https://www.physics.utah.edu/~whanlon/spectrum.html`

at $\sim 10^{18}$ eV, the spectral index rises again up to a cut-off that has been measured at $\sim 10^{20}$ eV. This differential energy spectrum has been measured by many different instruments, as it can be seen in Figure 1.1.
Due to deflections of the electric charged cosmic-ray particles in interplanetary and interstellar magnetic fields they arrive at Earth with great directional isotropy. An anisotropy with a dipole shape that was detected for the highest energy cosmic rays by Pierre Auger Collaboration et al. [2017] points towards an extragalactic origin of these particles. This is supported by an indication for an excess of these extremely energetic particles from strong extragalactic sources [Aab et al. 2018]. Besides these findings, the mystery of the origin of the cosmic rays is still not completely solved. One way of tackling the problem is provided by gamma-ray astronomy, as it will be discussed in the following sections.

1.2 Generation of cosmic gamma rays

Cosmic gamma-rays can be generated from ultra-relativistic particles in different processes. Usually, one discriminates between hadronic and leptonic production scenarios. In the leptonic scenario, ultra-relativistic electrons are subject to Inverse Compton (IC) scattering on lower energetic photons. These target photons may e.g. be part

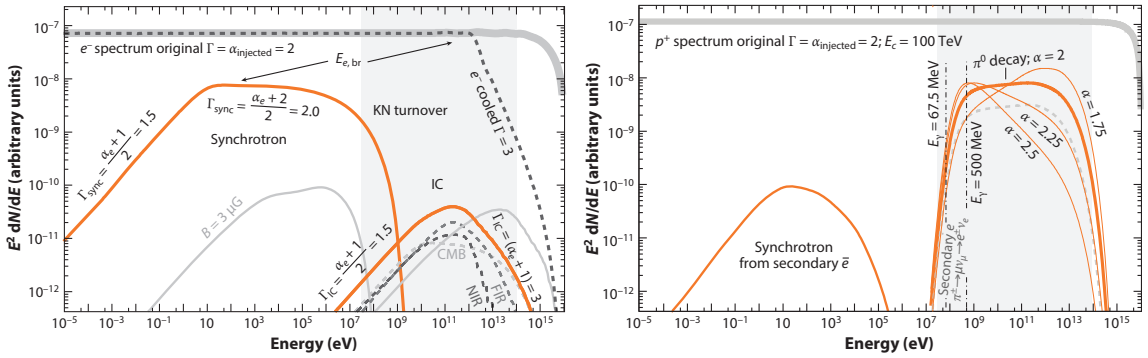

Figure 1.2: Spectral energy distributions of photons generated in interactions of accelerated particles for the leptonic and the hadronic scenario. The grey area denotes the range of sensitivity of current gamma-ray detectors (Fermi-LAT and IACTs). **Left:** Synchrotron and IC emission (orange) by an electron population with spectral index 2 (light grey) in a magnetic field of 100 µG. **Right:** Gamma radiation by pion decay and synchrotron radiation by secondary positrons (orange) caused by a proton population with spectral index 2 and a cut-off energy of 100 TeV (light grey). The light orange lines show the resulting gamma-ray spectrum for different spectral indices of the proton spectrum. Figures adopted from Funk [2015].

of the cosmic microwave background (CMB) or infrared or optical radiation fields. Written as a reaction equation, this gives [Lorenz et al. 2012]:

$$\mathrm{e} + \gamma_{\text{low energy}} \longrightarrow \mathrm{e}_{\text{low energy}} + \gamma_{\mathrm{VHE}}.$$

The energy gain of the photon in this process is directly proportional to γ^2, where γ is the Lorentz factor of the ultra-relativistic electron before the interaction.
In the hadronic scenario, high energetic atomic nuclei interact with interstellar matter. In these inelastic scatterings, various particles are produced which sooner or later decay to neutral and charged pions:

$$\text{nucleus} + \text{nucleus}_{\text{target}} \longrightarrow \text{nucleus}' + \ldots + \pi^0 + \pi^{\pm}.$$

Neutral pions themselves decay primarily into two gamma-ray photons:

$$\pi^0 \longrightarrow 2\gamma.$$

Charged pions on the other hand decay almost exclusively into a (anti-)muon and a(n) (anti-)muon-neutrino. The such produced (anti-)muons decay into electrons or positrons and (anti-)electron- and (anti-)muon-neutrino pairs:

$$\pi^+ \longrightarrow \mu^+\nu_\mu \longrightarrow \mathrm{e}^+\nu_\mathrm{e}\bar{\nu}_\mu\nu_\mu \quad \text{and} \quad \pi^- \longrightarrow \mu^-\bar{\nu}_\mu \longrightarrow \mathrm{e}^-\bar{\nu}_\mathrm{e}\nu_\mu\bar{\nu}_\mu$$

While the emerging neutrinos represent the messenger particles that are studied in neutrino astrophysics, the generated electrons may compete with primarily accelerated electrons and may themselves produce photons in leptonic processes. The hadronic scenario is of particular interest for astroparticle physics because detecting such processes provides unambiguous evidence for accelerated atomic nuclei which can be used

for the explanation of the cosmic rays that are measured at Earth. While the detection of a neutrino signal would provide direct evidence for a hadronic production process, the VHE-photons produced in the decay of neutral pions can be probed by gamma-ray astronomers because their energy spectra are predicted to differ from gamma-ray populations produced in leptonic processes (see Figure 1.2).

1.3 Acceleration mechanisms of relativistic particles

Since the first detection of cosmic rays, it has been a key question among astrophysicists how these particles can reach energies of up to $10^{20}\,\mathrm{eV}$ and how the power law shape of their energy spectrum comes into being. This section introduces the most important mechanisms that are proposed as an answer to this question.
In 1949, Enrico Fermi proposed a mechanism in which particles are multiply scattered between randomly moving "magnetic mirrors" [Fermi 1949]. These mirrors correspond to irregularities in the galactic magnetic field caused by clouds in the interstellar medium. In this picture, the average energy gain that a particle experiences in each collision is second-order in V/c:

$$\langle \Delta E/E \rangle \propto \left(\frac{V}{c}\right)^2 , \tag{1.2}$$

where V is the typical velocity of the moving mirrors and c the velocity of light in vacuum. Due to this dependence, this mechanism was given the name of *second-order Fermi acceleration*. It can be shown that the exponential increase of energy per particle results in a power-law energy spectrum where the exponent depends on V^2, the mean free path L between clouds along the magnetic field lines, and the time τ_{esc} that a particle remains within the acceleration region.
Although this mechanism can explain the power-law shape of the observed cosmic-ray energy spectrum, it has some limitations: The predicted energy gain of the particles is very slow given the small velocities of interstellar clouds of typically $V/c < 10^{-4}$ and the large mean free paths in the order of 0.1 pc. The theory is also unable to explain the experimentally derived exponent of the energy spectrum of roughly −2.5.
Another mechanism was proposed independently by different authors in the late 1970s (Axford et al. [1977], Krymsky [1977], Bell [1978], and Blandford et al. [1978]). Their acceleration model is based on strong shock waves that propagate through the interstellar medium. Such disturbances in a gas that move with supersonic velocities occur for example at the expanding shells of supernova remnants. In this picture, particles are accelerated when they cross the shock front either from upstream to downstream or the other way around. This is explained as follows: The shock front moves with the velocity u through the medium. When transforming to the reference frame in which the shock front is at rest, the upstream gas approaches with velocity $v_1 = |u|$. (The different reference frames are also visualised in Figure 1.3.) The downstream gas moves away with velocity v_2. By considering mass conservation at the discontinuity and by assuming that the gas can be described as fully ionised plasma, one obtains the

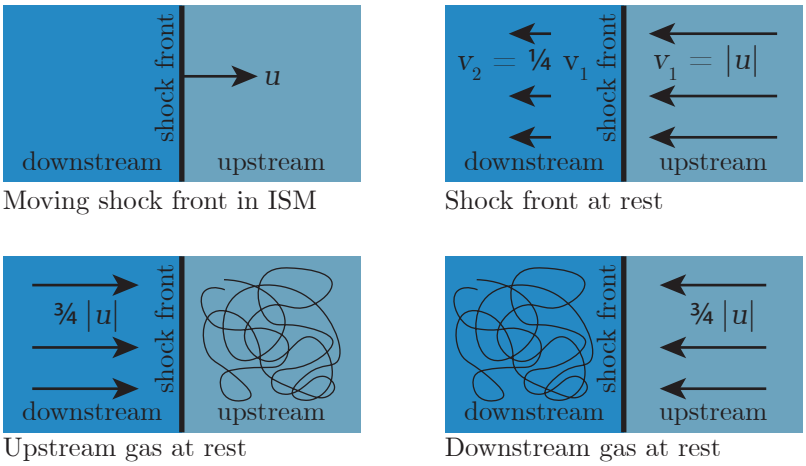

Figure 1.3: The kinematics close to a strong shock wave. **Top left:** The shock front discontinuity traverses the ISM with velocity u. **Top right:** Same situation in the rest frame of the shock front. The upstream and downstream gases move with velocities v_1 and v_2, respectively. **Bottom left:** In the rest frame of the upstream gas. A multiply scattered particle with isotropically random velocity sees the downstream gas approach with a velocity of $(3/4)\,|u|$. **Bottom right:** In the rest frame of the downstream gas. From the point of view of an isotropic particle, the upstream gas approaches with a velocity of $(3/4)\,|u|$.

relation $v_2 = (1/4)v_1$. When transforming now to the reference frames where either the gas in the upstream region or in the downstream region is at rest, one sees that the gas in the opposite region moves with a velocity of $(3/4)|u|$ towards the shock front. A particle that is multiply scattered at magnetic irregularities in the upstream region of the shock front moves randomly with velocities isotropically distributed in the rest frame of the upstream gas. If this particle now happens to cross the discontinuity and is diffused into the relatively moving reference frame, it receives a small increase in energy that is proportional to u/c in a Lorentz boost. From the downstream region, the particle can again traverse to the upstream region and gain more energy. This process repeats until the particle leaves the acceleration region. One can show that in this model, a differential energy spectrum of accelerated particles with a power-law shape with exponent -2 is produced. This exponent is obtained without making any assumptions on the physical details of the shock front and the gas, rendering the *diffusive shock acceleration* adoptable to many different astrophysical objects where strong shock fronts are present. Due to the linear dependence on u/c, the process is also called *first-order Fermi acceleration*. It is more suitable for explaining the cosmic ray flux measured at Earth as opposed to second-order Fermi acceleration and is therefore currently the most accepted theory for this problem.

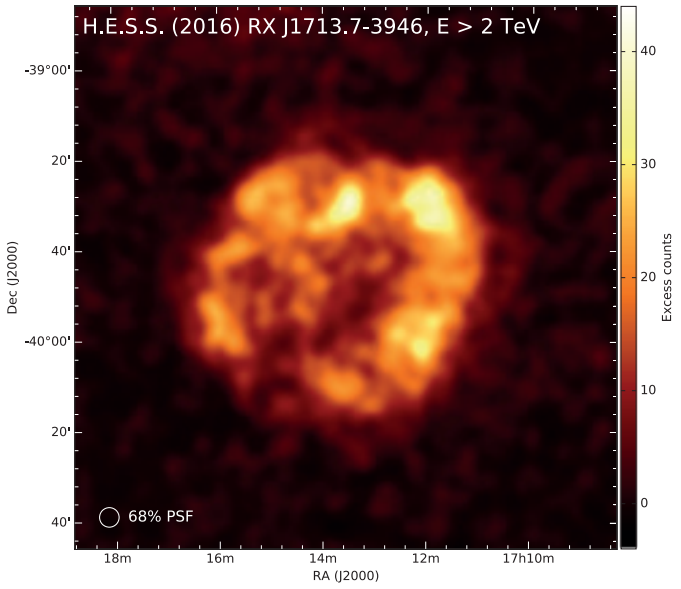

Figure 1.4: Excess counts map of photon energies > 2 TeV from the shell-like SNR RX J1713.7–3946 as measured with the gamma-ray observatory H.E.S.S. [H.E.S.S. Collaboration et al. 2018b]

1.4 Astrophysical sources of gamma rays

Supernova remnants

At the end of the lifetime of a star, when it runs low in the elements fuelling the fusion reaction, the thermal pressure that counteracted gravity ceases and the star collapses. The stable states in which the collapsing star can end up include white dwarfs, neutron stars, and black holes. Which one is reached depends on the initial mass of the star and the amount of matter it looses before the collapse. The central iron core of very massive stars can collapse within a few seconds. In this process, a neutron star is formed when the protons and electrons in the core combine to neutron via inverse beta-decay. The energy that is released in the collapse gives rise to a *supernova*, in which the star explodes and its outer layers are ejected into the interstellar medium. Besides these core-collapse supernovae, another type of these explosions can occur, when a white dwarf accretes mass from a companion star and excels the mass limit where it is gravitationally stable. These events are referred to as Type Ia supernovae. This type and all sub-types of core-collapse supernovae can be discriminated via their optical spectrum and their temporal evolution of luminosity. The brightnesses of these violent events are so high that they can be observed with the naked eye during daytime if they are located close enough to Earth, like it was the case on 4th July 1057, when a supernova gave rise to the Crab Nebula.
In a supernova, a radial shock wave is formed that travels outwards with velocities of about $(10 \text{ to } 20) \times 10^3\,\mathrm{km\,s^{-1}}$ and sweeps up mass of the interstellar medium. Due to the high temperatures that arise, shell-like structures can be observed in optical,

infrared and x-ray wavebands. In the vicinity of the shock wave, charged particles with relativistic energies can be created via first-order Fermi acceleration. While relativistic electrons can produce detectable radio emission via synchrotron radiation and gamma rays via inverse Compton scattering, relativistic protons can give rise to gamma rays via hadronic processes (see 1.2). An example for a shell-like supernova remnant (SNR) is RX J1713.7–3946, which has been detected in gamma rays (see Figure 1.4). The motion of the shock front is practically undecelerated until the swept up mass exceeds the initially ejected mass. In the stage that follows, the dynamics of the SNR can be described with the adiabatic blast wave solution introduced in Taylor [1950a], Taylor [1950b], and Sedov [1959]. From here, the expansion decelerates while the temperature in the outer shells declines until the expansion becomes subsonic and the residual movement diffuses into the interstellar medium.

Pulsar wind nebulae

Another kind of supernova remnant that also emits VHE gamma rays is the pulsar wind nebula (PWN). In contrast to shell-like SNR, this class of astrophysical objects exhibits a maximum of emission at its centre and shows no shell structure. In such an object, the neutron star that was formed in the preceding supernova has a strong magnetic dipole field and rotates at high speeds around an axis that is at an angle to the symmetry axis of the magnetic field. Such strong magnetic fields in the range of (10^6 to 10^9) T can be produced during the collapse of the star as the field strength scales proportional to r^{-2} due to magnetic flux freezing, where r is the radius of the star. Because of the conservation of angular momentum, the same dependence on the radius holds for the angular speed. Due to the pulsating signal in different wavelength bands, this kind of neutron star is called *pulsar*. Powered by its rotational energy, the pulsar ejects a wind of relativistic particles, mainly electrons and positrons. Models assume that this relativistic wind terminates at a standing shock wave caused by the interaction with the surrounding supernova remnant [Rees et al. 1974], [Kennel et al. 1984]. At this shock front, relativistic particles can gain energies up to 10^4 TeV via diffusive shock acceleration. The emerging particles can then produce VHE gamma rays via inverse Compton scattering of photons which are part of the CMB or of synchrotron radiation produced by leptons in the pulsar wind.
The most prominent example for a PWN detected in VHE gamma rays is the Crab Nebula. In Figure 1.5, a disk of x-ray emitting material can be seen surrounding the pulsar together with two jets of relativistic particles that emerge from its poles.

Gamma-ray binaries

Most of the most massive stars in our galaxy and beyond are part of a binary star system (or part of a system with even more stars), meaning that two stars are gravitationally bound to each other and orbit a common centre of gravity [Zinnecker 2003]. When one of the companions in such a system reaches the end of its lifetime and explodes in a supernova, a system of massive star and a neutron star can emerge. There

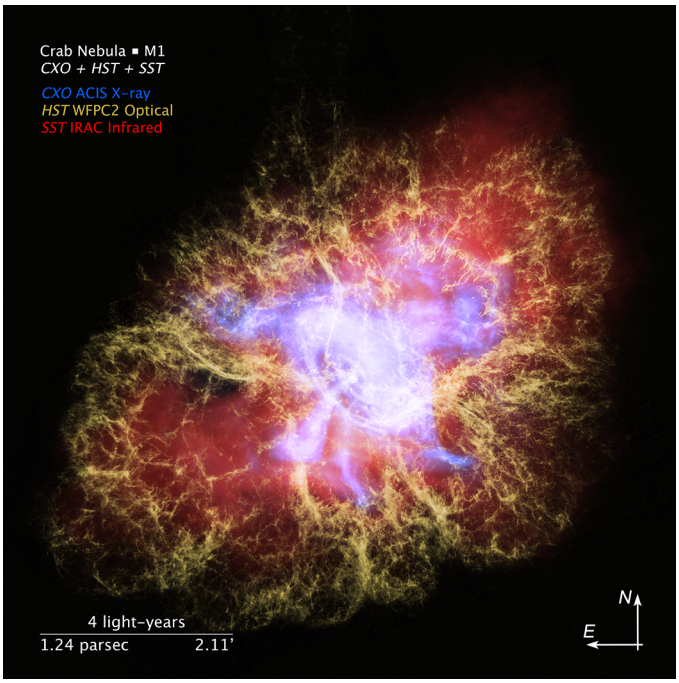

Figure 1.5: Multiwavelength image of the Crab Nebula with combined data from multiple instruments. The different colour layers are: x-ray radiation, measured by the Chandra X-ray Observatory (blue), visible light, detected with the Hubble Space Telescope (yellow), and infrared emission as seen by the Spitzer Space Telescope (red). Image credit: NASA, ESA, J. DePasquale, and R. Hurt. `https://hubblesite.org/contents/media/images/2020/03/4601-Image`

is evidence that some of these compound objects emit electromagnetic radiation in the VHE regime. One example is the pulsar PSR B1259–63 [F. Aharonian et al. 2005]. There are two proposed scenarios, how the gamma radiation can be produced in these gamma-ray binaries: In the first scenario, relativistic particles that produce gamma rays are accelerated at shocks that form at the intersection of pulsar winds from the neutron star and stellar winds from the massive star companion [G. Dubus 2006]. The second scenario proposes that the particle acceleration happens in or at the ends of relativistic jets that are produced in the accretion of matter from stellar winds to the neutron star or at the accretion disc itself (see e.g. Fender [2006]). The first scenario is considered more likely due to indirect evidence by measurements in different wavelength regimes. For a more detailed discussion see Guillaume Dubus [2013].
One notable feature of gamma-ray binaries is the expected periodic intensity-variation. This variation is caused by the changing distances and therefore also the interaction between the compact object and the massive star when they orbit each other. These variations are often difficult to detect in the VHE regime because of the limited time-windows in which corresponding instruments can observe the sources but are evident in other wavelengths.

Diffuse gamma-ray emission

In addition to spatially confined sources, HE and VHE gamma rays can also be produced in large regions in the interstellar space. This emission occurs when cosmic rays interact with the interstellar medium far away from the location where they were generated. It can be detected in the VHE gamma-ray regime as a diffuse signal, like it is the case for the galactic plane of the Milky Way [H.E.S.S. Collaboration et al. 2014].
The production mechanisms to be considered are again hadronic and inverse Compton emissions. The hadronic components originates from the decay of neutral pions that are created in the interaction of cosmic-ray nuclei with interstellar gas. The candidates for target material include primarily atomic, ionised, and molecular hydrogen, while the latter is predominantly found in molecular clouds. The leptonic part of the population of cosmic rays can loose energy in inverse Compton scatterings with radiation fields in the interstellar space which mainly consists of stellar photons and the CMB.
Detected diffuse emission is in a sense ambiguous as it can always be partly or completely produced in a set of spatially confined sources that can not be resolved individually by the instrument.

Chapter 2

Imaging Atmospheric Cherenkov Telescopes

This chapter gives an introduction to the detection principle of Imaging Atmospheric Cherenkov Telescopes (IACTs). Some important components of these instruments will be highlighted and the H.E.S.S. telescopes and the future CTA will be introduced and used for concrete comparisons. The second half of the chapter is dedicated to the methods of analysing the data that is acquired by such telescopes.

2.1 Detection principle

Atmospheric particle showers

When a cosmic gamma-ray photon enters the atmosphere, it interacts with the present atomic nuclei. The dominant process at high energies is electron-positron pair production. The resulting electrons and positrons loose energy in further interactions with the atoms in the atmosphere. For high energetic leptons, bremsstrahlung is the primary process. The two described processes occur repeatedly and a cascade of highly energetic, charged particles develops. The basic principles of this phenomenon are illustrated in a simple toy model by Heitler [1954] (see Figure 2.1) . This model assumes that the number of shower constituents (electrons, positrons, and photons) duplicate after passing through one collision length λ. So after n branchings, the number of constituents is

$$N(X) = 2^n = 2^{X/\lambda}, \tag{2.1}$$

where X is the slant depth along the axis of the cascade. It can also be seen that at not too small n the number of electrons and positrons is

$$N_e(X) = N(X) - N_\gamma(X) = \frac{2}{3}N(X),$$

where $N_\gamma(X)$ is the number of photons in the shower. The model further assumes that the energy is distributed evenly between the products of each interaction. Thus,

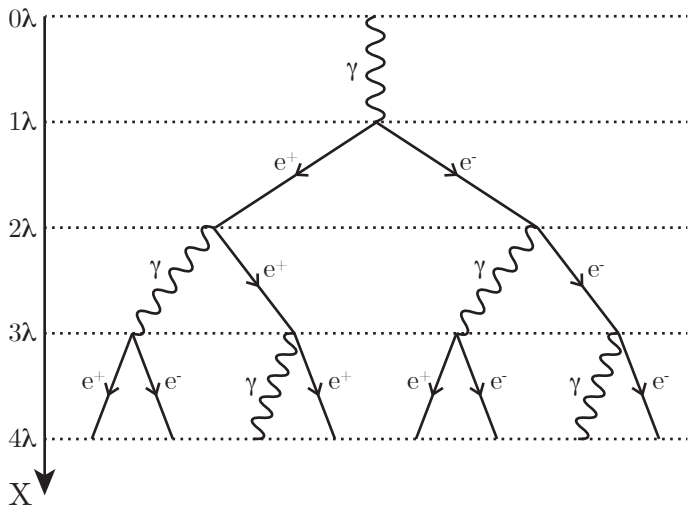

Figure 2.1: Schematic drawing of a gamma-ray shower in the atmosphere.

the energy per constituent is

$$E(X) = E_0/N(X),$$

where E_0 denotes the energy of the primary photon that induced the shower. The cascade continues up to the point where the critical energy $E(X) = E_c$ for one of the processes is reached. For bremsstrahlung in air, this critical energy is $E_c \approx 87\,\mathrm{MeV}$. Below this value, other energy loss processes become dominant and the electrons and positrons are eventually stopped. At this point at depth $X_{\max}$, the number of shower constituents is

$$N(X_{\max}) = E_0/E_c. \tag{2.2}$$

From 2.1 and 2.2 follows

$$X_{\max} = \lambda \frac{\ln(E_0/E_c)}{\ln 2}.$$

Although this model is rather crude, some important characteristics of atmospheric showers can be derived from it. First, the maximum number of particles is proportional to the energy of the primary photon. Second, the depth of the shower maximum is proportional to the logarithm of the energy of the initial photon.
Naturally, an atmospheric particle shower can also be induced by a cosmic ray electron or positron. Such showers differ from gamma-ray cascades only in their depth of their first interaction because the collision length of an electron or positron is a factor of about 9/7 larger than that of a photon. The typical altitude of the start of a gamma-ray shower is 20 km above sea level. For a primary photon with an energy of 1 TeV, the shower develops its maximum at about 8 km above sea level.
Cosmic-ray nucleons, which also induce particle showers, constitute the main background for ground based gamma-ray astronomy. These showers develop differently because they include hadronic interactions which have different momentum transfers.

Such cascades are typically more laterally extended and show a less homogeneous profile. The challenge of discriminating between photon and hadron induced showers will be discussed in 2.4.

Cherenkov radiation

The high energetic charged particles in the showers described above move through the atmosphere with velocities greater than the local speed of light

$$c_{\mathrm{loc}} = \frac{c}{n}, \tag{2.3}$$

where n denotes the refractive index of the medium and c the speed of light in vacuum. This leads to net polarizations of the surrounding molecules that the particle passes by. As these polarisations move through the medium, electromagnetic waves are radiated. This radiation is known as Cherenkov radiation, named after its first observer Cherenkov [1937]. The Cherenkov light is radiated in forward direction of the moving particles in a cone with an opening angle of

$$\theta = \cos^{-1}\left(\frac{c_{\mathrm{loc}}}{v}\right),$$

where v is the speed of the particle. Because the refractive index of the atmosphere is dependent on the altitude h and follows approximately

$$n(h) = 1 + 0.00283\frac{\rho_{\mathrm{air}}(h)}{\rho_{\mathrm{air}}(0)},$$

with the density of air ρ_{air}, the opening angle also changes with the altitude at which the Cherenkov photons are emitted. This fact and different emission heights lead to illuminated circular areas on the ground with radii in the order of 100 m.

Detection of Cherenkov light

The Cherenkov radiation that hits the ground can be detected with suitable instruments. For such a device, the main challenges are the ability to collect enough photons of the Cherenkov cone and to be sensitive for the short light pulses in the order of nanoseconds. Therefore, large mirror surfaces are used which collect the light and image it to specially designed Cherenkov cameras. Due to this imaging process, such instruments are called “Imaging Air Cherenkov Telescopes” (IACTs).

2.2 Two gamma-ray instruments

H.E.S.S.

H.E.S.S. (High Energy Stereoscopic System) is a very successful gamma-ray telescope that is located in the Khomas Highland in Namibia at 1800 m a.s.l. [F. Aharonian et

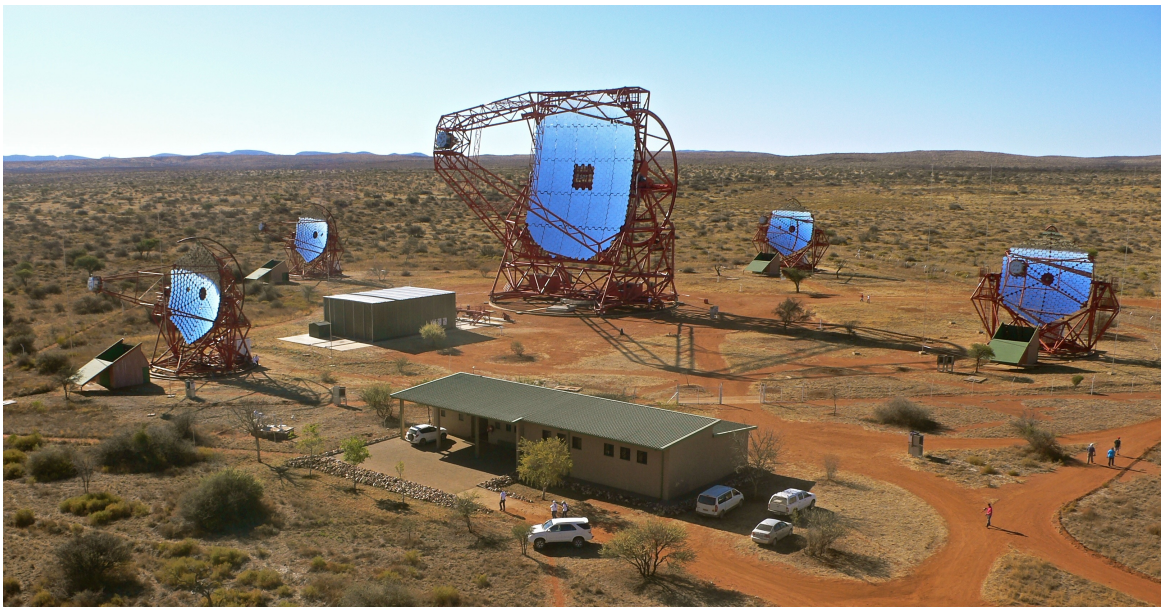

Figure 2.2: Photograph of the complete H.E.S.S. telescope array with the four smaller telescopes CT1-4 and its large telescope CT5 in the centre. Image credit: H.E.S.S. Collaboration.

al. 2006]. It consists of five individual Cherenkov telescopes: four smaller telescopes at the corners of a square on the ground with a side length of 120 m and larger telescope in the centre of the square (see Figure 2.2). The first of the smaller telescopes started taking data in 2002. Phase I of the experiment, which denominates the complete array of the four smaller telescopes, started operation in 2003. These telescopes are referred to as CT1-4 (Cherenkov Telescope 1-4). The larger telescope (CT5) joined the data acquisition in 2012, heralding Phase II [Holler et al. 2013]. Observations in H.E.S.S. are carried out in runs of 28 min or less during which the telescopes track one source of interest over the sky.

CTA

CTA (Cherenkov Telescope Array) is the future ground based gamma-ray observatory that is designed to have improved sensitivity, better resolution, and increased detection efficiency compared to current IACTs [CTA Consortium 2019]. It will consist of two arrays of Cherenkov telescopes, one on the northern hemisphere (La Palma, Spain) and one on the southern hemisphere (Paranal, Chile) with the aim of making the whole sky observable. Each of the two arrays will consist of multiple telescopes of varying sizes (see Figure 2.3). The three major classes are called LST, MST, and SST, which stands for Large, Medium, and Small Size Telescope, respectively.

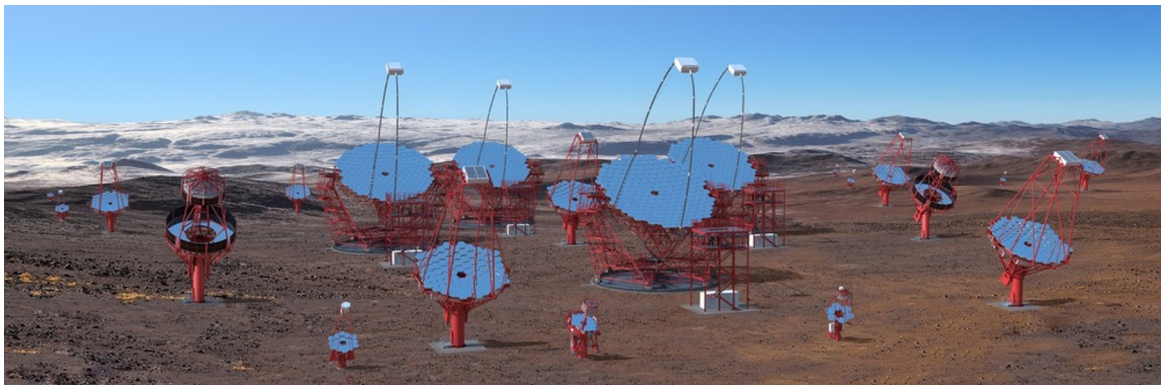

Figure 2.3: Artist's impression of the southern site of the future gamma-ray observatory CTA. Cherenkov telescopes of three different sizes and in different proposed implementations are placed in the Atacama Desert in Chile. Image credit: Gabriel Pérez Diaz, IAC / Marc-André Besel, CTAO.

2.3 Components of IACTs

Optics

Due to better optical performance in comparison to refractive optics, larger IACTs are exclusively constructed with light reflecting mirrors that focus the Cherenkov light onto the camera focal plane. The main characteristics of such a reflector system are the light collection capability, the field of view, the point spread function (PSF), and the time dispersion. The number of photons that is collected by a reflector naturally scales with its area. Because air showers induced by lower energy gamma rays emit less Cherenkov light, larger mirror diameters decrease the lower energy threshold of a telescope. In order to achieve energy thresholds of several tens of GeV, reflectors with diameters of up to 30 m are applied. Such large mirrors are usually constructed from smaller facets, which make the optics mechanically simpler and more cost efficient. The field of view is both dependent on the size of the sensitive area in the focal plane and on the optical properties of the refracting system which determine the maximum distance to the optical axis where an acceptable PSF is guaranteed. An acceptable PSF in this context means that incoming, parallel light is focussed to an area that is small in comparison to the pixel size of the camera. To improve the PSF at the edges of the field of view, the ratio between telescope focal length and mirror diameter f/d can be increased. There are also different geometrical design types of telescope reflectors. One of them is the Davies-Cotton design [Davies et al. 1957]. Mirrors with this design consist of spherical facets with the focal length f, equal to the focal length of the telescope. This focal length corresponds to a radius of curvature of $2f$ for the facets. These are mounted on a spherical dish with a radius of f. With this design, a good PSF can be achieved within a wide field of view. It is therefore used for the smaller H.E.S.S. telescopes and the MST where a large field of view is desired. Since the time dispersion for this type of reflector is larger than for other types due to varying lengths of the light paths for different distances to the optical axis, this

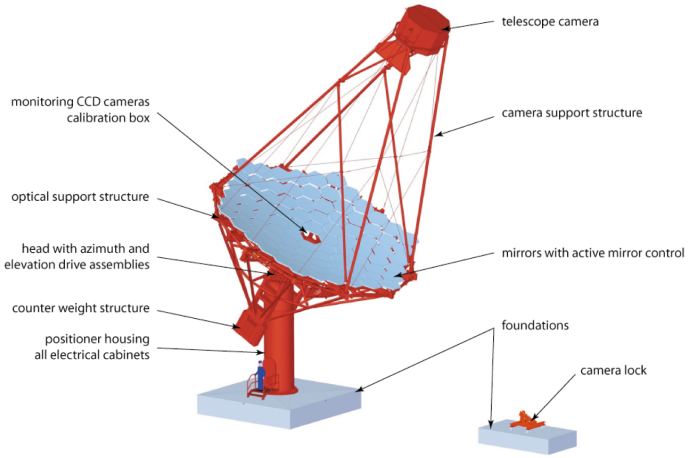

Figure 2.4: Drawing of the MST design with its main components. [Garczarczyk 2016]

design is not suitable for IACTs with the largest mirror diameters like e.g. CT5 and the LST with 28 m and 23 m mirror diameters, respectively. For these telescopes, a parabolic reflector design is used, which has virtually no time dispersion at the cost of a reduced field of view. Another design, the so called Schwarzschild-Couder design, uses two aspherical mirrors to reduce the focal length while increasing the resolution over a large field of view. This concept is currently investigated for the usability in some designs of the SST and in the SCT, an alternative to the MST. The problem of the significantly increased complexity of the optical system is compensated by the fact that the focal plane of a Schwarzschild-Couder telescope can be much smaller, which makes the use of smaller and cheaper cameras possible.

Telescope mount

The ability of slewing to sources of interest in the sky and following their apparent motion is a key feature of pointed telescopes like IACTs. In general, there are two main types of tracking mounts for telescopes: equatorial and azimuthal mounts. In an equatorial mount, the instrument is rotated around two axes, whereof one (the right ascension axis) is parallel to the earth's axis of rotation and the other one (the declination axis) is perpendicular to that. In this setup, the instrument has to be rotated solely around the right ascension axis to follow an astrophysical object over the sky. Due to its mechanical complexity, this type of telescope mount is mainly used for smaller instruments. In contrast to this, azimuthal mounts are mechanically rather simple. They also use two axes but the first one (the azimuth axis) is vertical and points to the zenith. The second one (the altitude or elevation axis) is perpendicular to that and therefore parallel to the ground. To move the instrument along with the apparent motion of a source over the sky, the angles of both axes have to be adjusted at varying speeds. Since astronomical objects apparently only move around the right ascension axis (not considering proper motion, radial speed and parallax) and an instrument with an azimuthal mount around two different axes, all positions

in the field of view of such an instrument are subject to rotation around its optical axis. In the field of gamma-ray astronomy, azimuthal mounts are preferred. Two main realizations for this type of mount are used in current instruments. A circular rail system for example is used for all H.E.S.S. telescopes [Bernlöhr et al. 2003]. The elevation axis is supported by two towers which can move on wheels around a central bearing. It is positioned in a way that balances the telescope. This design provides easy access to the camera at ground level because of the low elevation angles that can be reached. A different and more compact realization of an azimuthal mount uses a central positioner, i.e. the telescope mirror dish is attached to the top of a tower with two bearings. One of them allows the telescope to rotate around the tower, the other one is used to adjust the observed altitude. To move the center of gravity to the central, vertical axis of the tower and therefore balance the system, counterweights have to be applied. It is also possible to support negative elevation angles for camera maintenance if the elevation axis is moved away from the center of the tower. The advantages of this mount technique are the reduced on-site construction and maintenance efforts because the tracking mechanics are confined inside the central tower and the foundation for a telescope with such a mount is smaller and easier to build. Due to the large number of individual telescopes that will be built, this realization is chosen for all designs of the MST and SST. A drawing of the current MST design with its central positioner can be seen in Figure 2.4.

Cherenkov light detector

When designing a Cherenkov light detector (also called Cherenkov camera) for a telescope, one has to take into account different requirements. First, the photon detecting units of a pixelated camera have to be both sensitive enough to detect even single photons and also fast enough to resolve the short Cherenkov pulses with lengths in the range of several nanoseconds. The detector of choice for the majority of current IACTs therefore has been the photomultiplier tube (PMT). In this kind of sensor, incident photons are converted into electrons at a photo cathode. The emerging electrons are then successively accelerated to several dynodes via applied high voltages. At the dynodes, single electrons are converted into multiple electrons, which add up to a measurable charge at the last anode of the detector. Another type of sensor, that is investigated for its application in CTA telescopes is the silicon photomultiplier (SiPM). The application of this kind of sensor for Cherenkov telescope has been pioneered by the FACT collaboration [Bretz et al. 2013]. A single pixel of a SiPM consists of many semiconductor photodiode cells which are operated in Geiger mode [Buzhan et al. 2002]. It can also detect single photons and reaches sufficient temporal responses for Cherenkov pulses. SiPMs have the advantage over PMTs that they are less susceptible to high photon rates and that they do not need high voltages for operation at the downside of increased dark count rates which require effective cooling of the sensor.
Another important property of a Cherenkov camera is the size of individual pixels. They have to be small enough to achieve images of the particle showers with sufficient

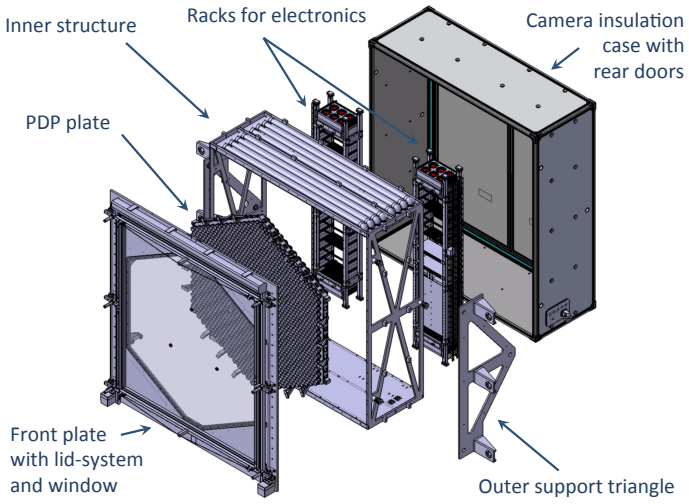

Figure 2.5: Exploded view of FlashCam, a Cherenkov detector for the MST [Pühlhofer et al. 2015].

resolution for the given optics of the telescope. The desired angles of the sky that should be covered by one pixel are in the range of 0.1° to 0.25° depending on the type of telescope and targeted gamma-ray energies. For a single mirror telescope, these angles translate to 40 mm to 35 mm of pixel size, which is in the range of available PMT sizes. For a two-mirror optics design, the focal plane gets much smaller and pixel sizes of ~ 6 mm are necessary. These are right now only achievable with SiPMs. To be able to use the characteristics of the waveform of the signal of the individual pixels, the output of the sensors has to be sampled over time. In principle there are two strategies to achieve this. In one approach, the signal is continuously sampled in an analogue memory. From there, it is read out and digitized via an analogue-to-digital converter (ADC) when the trigger system detects an interesting event. This technique is used for a variety of IACTs including the H.E.S.S. I telescopes [Giavitto et al. 2016]. The second approach includes the signal being continuously digitized using fast flash analogue-to-digital converters (FADCs) and written to digital buffer memory where it can be read out. This method is being adopted for CTA with the FlashCam [Pühlhofer et al. 2012] project and makes use of recent advances in power consumption and cost efficiency of FADCs. A camera with this technique has been designed for the use in the MST [Pühlhofer et al. 2015]. It contains focal plane detectors (1764 PMTs) and digitization and readout electronics in a 2.9 x 3 x 1.1 m^3 casing (see Figure 2.5). An alternative design for a camera for the MST that uses analogue sampling is NectarCam [Glicenstein et al. 2015]. It is also an integrated camera with similar dimensions of 2.9 x 2.9 x 1.5 m^3 [Moulin et al. 2015].

Camera support structure

Of course, the Cherenkov camera has to be mounted to the telescope in such a way that its photon detecting elements reside in the focal plane of the optical system. This

is done via the camera support structure (CSS) which is some kind of mast that holds the camera in place. When designing a CSS, a compromise between two properties has to be found: rigidness to keep the detector at the same location relative to the dish and reduced shadowing of the Cherenkov light that has to transverse the CSS to be collected by the mirror. Currently applied designs are either built as massive but stable steel structures like for the MST or of a combination of carbon fibre and aluminium which is more flexible but also lighter. Latter design is used for example for the LST [Cortina et al. 2015].

2.4 Low level analysis of IACT data

Once raw data of cosmic gamma-ray emitting sources has been acquired by an IACT, there are still many more steps to undertake in order to reduce the data to only contain information that is needed for the study of astrophysical sources. This section introduces these steps using the example of the H.E.S.S. experiment utilizing F. Aharonian et al. [2006] as the main reference.

Data quality selection

H.E.S.S. observations are organized in so called runs of nominally 28 min. Selection cuts are applied at the run level, meaning that observations which do not meet certain quality requirements are sorted out. For example, runs which are shorter than 10 min due to technical issues during data taking are not used. Also runs with strongly varying or lower than expected trigger rate are excluded. The trigger rate is dominated by cosmic-ray introduced background events and depends primarily on the zenith angle and atmospheric conditions and is therefore a good indicator of suitable observation conditions. Another criterion is the number of inactive pixels in the camera of a telescope. Single PMTs can be switched off due to technical issues or because of unexpected light sources like meteors or aeroplanes triggering the over-current protection. Too few active pixels would increase uncertainties in the analysis of the images. Therefore, individual telescopes are excluded from an observation if the number of inactive pixels is too large.

Calibration of the instrument

Because the primary energy of air showers directly depends on the amplitude of the signals of the PMTs in the Cherenkov camera, it is crucial to calibrate their response to incident photons. One step of this calibration is the measurement of the pedestal and the signal from a single photoelectron (p.e.). These values are determined via specific calibration runs [F. Aharonian et al. 2004]. The signal for the single p.e. response is provided by an LED flasher that illuminates the camera focal plane while pedestal runs are carried out without any light exposure. To also correct for differing light collection

and photocathode efficiencies over the focal plane, so called flat-field coefficients are derived for the individual pixels of a camera in dedicated flat-field runs. During the latter, the camera is illuminated uniformly by LED flashers which are mounted at the telescope dishes. The deviations of individual pixel signals from the mean signal in the camera is then used for the determination of the flat-field coefficients. The optical efficiency, i.e. the reflectivity and collection efficiency of the telescope mirrors, is measured via the signal of local muons that originate from hadronic particle showers and that pass a telescope close to the optical axis [Bolz 2004]. The expected number of Cherenkov photons that an atmospheric muon produces can be calculated by few simple parameters of their ring-shaped images. This number is then compared to the measured quantity and is used for calibration. Another important calibration task is the pointing which will be discussed in more detail in Chapter 3.

Image cleaning

Before further analysis of features of the images of measured particle showers is carried out, the acquired images are subject to cleaning procedures. These serve the purpose of removing the signal of photons that do not originate from the measured particle shower. For H.E.S.S., this is done by setting the signal of pixels to zero that do not have a minimum signal of 5 p.e. and at least one neighbour pixel with a minimum of 10 p.e. or vice versa. This way, spatially correlated features in the images which correspond to the particle showers are selected while signals that originate from night sky background are discarded.

Event reconstruction

The two most relevant properties of a gamma-ray induced air shower are its direction of propagation and the energy of the incident photon. To determine the former, the geometrical shape of the imaged shower is analysed. A typical gamma ray shower produces an image with an elongated, elliptical form. The semi-major axis corresponds to the longitudinal direction, whereas the semi-minor axis corresponds to the lateral direction of the shower. If one shower is detected by several telescopes simultaneously, like it is done in all IACT arrays that are operated in stereoscopic mode, information in these images taken from different angles can be combined (see Figure 2.6). There are multiple methods to derive the shower geometry from these images [Hofmann et al. 1999]. The most basic among these first describe the shower images by the so-called Hillas parameters. These include the angle and the distance from the center of the focal plane but also the length and width of the image which are defined as the r.m.s. spread of pixel values parallel and perpendicular to the semi-major axis [Hillas 1985]. Once these parameters are known and the images of multiple telescopes have been transformed to a common coordinate system, the intersection point of all semi-major axes can be determined. This point corresponds to the origin of the gamma-ray shower.

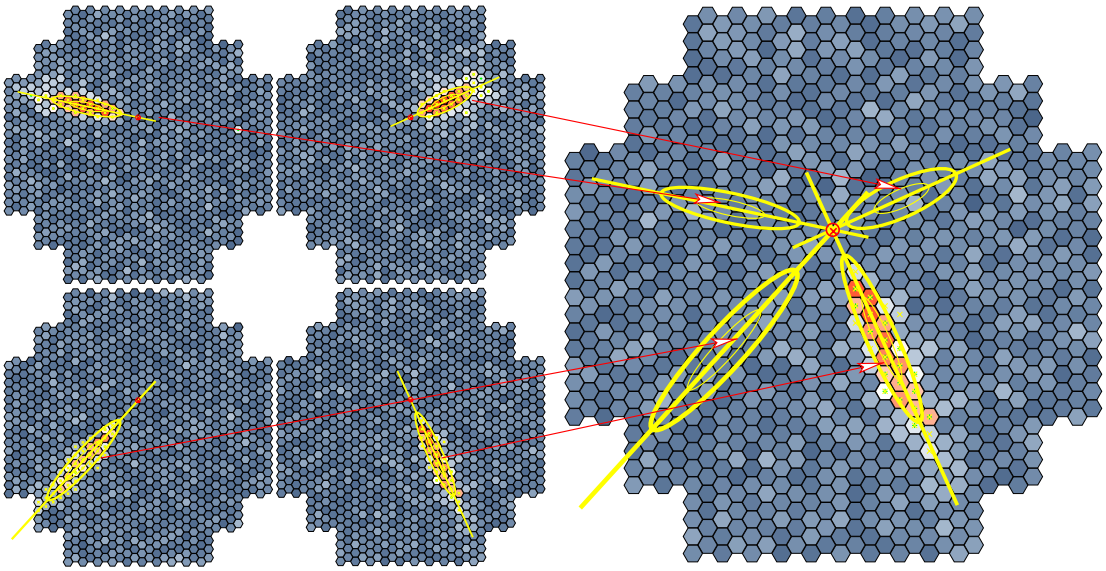

Figure 2.6: Schematic drawing of the images of one gamma-ray shower as seen from four different Cherenkov telescopes in stereoscopic mode. The approximately elliptical shapes can be transformed to a common coordinate system and the intersection point of the semi-major axes indicates the origin of the photon that induced the shower. Image credit: K. Bernlöhr.

The uncertainty of this reconstructed direction is expressed by the point spread function (PSF). It is defined as the distribution of the angular distance between the reconstructed and the true origin of a gamma-ray event. The relevant uncertainties are caused both by the instrument, like optical and pointing capabilities of the telescope, and by fluctuations in the development of the air shower itself. The shape of the PSF depends on the conditions during the observation: The zenith angle, the angular separation between pointing position and the detected photon, the energy of the latter, the optical efficiency of the telescope, and the number of telescopes taking part in the detection are the primary parameters. The shape of the PSF is typically determined by detailed simulations of the whole data acquisition process. Its size, as a measure of spatial resolution, is often expressed as the 68% containment radius. Typical values for H.E.S.S. are in the order of 0.1°.
As shown in Section 2.1, the number of charged particles and hence the amount of Cherenkov light scales with the energy of the original photon. It also scales with the shower's impact parameter (the distance between a telescope and the intersection point of the main axis of the shower with the ground). Because of this, the energy of a photon is reconstructed with the help of lookup tables that contain the mean energy of simulated photons for different image amplitudes and impact parameters. The energies are determined with these lookup tables for each telescope that participated in the detection individually and the average energy for all telescopes is calculated. The distribution of the reconstruction error $E_\Delta = (E_{\mathrm{reco}} - E_{\mathrm{true}})/E_{\mathrm{true}}$ defines two important properties of the energy reconstruction: its width equals the energy resolution with typical values of $\sim 15\%$ and its mean value defines the energy

bias E_{bias}. Below a certain primary energy, gamma-ray induced showers are only detected if their development fluctuates to higher brightnesses. This leads to a rising energy bias at low energies. Therefore, this quantity is used for the definition of a lower energy threshold down to which spectral analyses are sensible. The energy bias of two exemplary H.E.S.S. observations that were carried out at different zenith angles is visualised in the left panel of Figure 2.8 for two different offset angles.
More sophisticated methods besides the classical Hillas parameter approach use semi analytical models or camera pixel data from simulations which are fit to the camera images [Naurois et al. 2009], [Parsons et al. 2014]. With these methods, better energy resolutions and narrower PSFs can be achieved.

Gamma-hadron separation

Another important task of the analysis methods is the separation of gamma-ray events from background events caused by cosmic-ray particles. That is, the measured events have to be differentiated into gamma-ray like and hadron like events. The most basic approach in doing so is achieved by introducing scaled parameters e.g. for width and length of shower images. A scaled parameter is defined as

$$p_{\text{sc}} = (p - \bar{p})/\sigma_p \tag{2.4}$$

with $\bar{p}$ the mean value and σ_p the scatter of the parameter p [F. Aharonian et al. 2006]. The mean and scatter of the parameters are dependant on the integrated image intensity, the impact distance of the event, and the zenith angle of the observation. They are derived from simulations for different configurations and filled into lookup tables in order to be used during reconstruction. By averaging over individual telescope images of the same air shower, *mean reduced scaled width* (MRSW) and *mean reduced scaled length* (MRSL) can be calculated. Selection cuts that have been optimised with the help of simulations are then applied to these parameters to filter out background events that differ from gamma-ray events in their shape.
A more advanced method for discriminating between signal and background uses *boosted decision trees* (BDT) [Ohm et al. 2009]. These trees are built such that the events are classified in multiple consecutive binary decisions. Each of these decisions is based on one particular parameter of the shower images like e.g. MRSW. After traversing a tree, an event is assigned a classification parameter ζ which is a measure for the event being more gamma-ray like or hadron like. The trees are then "trained" with sets of simulated data of signal and background events. To make the classification algorithm less sensitive to fluctuations in the test data, multiple trees are build with different weightings of the events in the training data set and combined to so called *forests*. This procedure is called *boosting*. During analysis, one event is then fed through multiple trees and is classified by the average value of the ζ parameter.
All methods for gamma-hadron separation can only reach a certain degree of efficiency. Some hadron-induced air showers that are too similar to gamma-ray showers will always pass the cuts. To account for the residual contamination of background events

in the data is one important task of the high level analysis, which will be presented in the next section.

2.5 High level analysis of IACT data

After the data taken by an IACT has been reduced to individual events with direction and energy information by the lower-level analysis, higher-level tools are applied to derive astrophysically meaningful information. One key aspect of these tools is the estimation of the residual background events that cannot be sorted out due to their similarity to gamma-ray events. The tools are also responsible for calculating detection significances of sources and their spatial and spectral properties.
This section introduces the methods of these tools and also discusses the software framework *GammaLib/ctools* [Knödlseder et al. 2016], which has been used for the analysis in this thesis, in detail.

Estimation of residual background

The primarily used methods in H.E.S.S. for estimating the residual background in a given observation use information from the same observation. In the observed field of view, on-regions are defined, which are expected to contain all gamma-ray emission from the source of interest. Off-regions on the other hand, are spatial areas where no gamma-ray signal is expected. In addition to that, exclusion-regions can be defined, which correspond to areas where other known sources are expected to emit gamma rays or where the presence of emission is unknown. The following paragraphs give an overview how these on-off region based methods work and contrast them to the on-off observation procedure and the novel template background method.

Reflected background model

This very simple technique makes use of the assumption that the acceptance of background events is radially symmetric in the field of view [F. Aharonian et al. 2006]. This background modelling works only for data acquired in wobble mode which means that the telescope was not pointed directly at the source of interest, but at a position with a small offset to it, such that the source is still in the field of view. The on-region is "reflected" to the other side of the pointing position and an off-region with a solid angle equal to the on-region is placed at that position. Other off-regions of the same size are also placed at equal distances to the pointing direction (see Figure 2.7 left). They are distributed such that they intersect neither with any exclusion-region nor with the on-region. The background at the on-region is estimated as the sum of events from the off-regions, scaled by the ratio between the total solid angle of all off-regions and the solid angle of the on-region.
This background model is especially suitable for the spectral analysis of point sources,

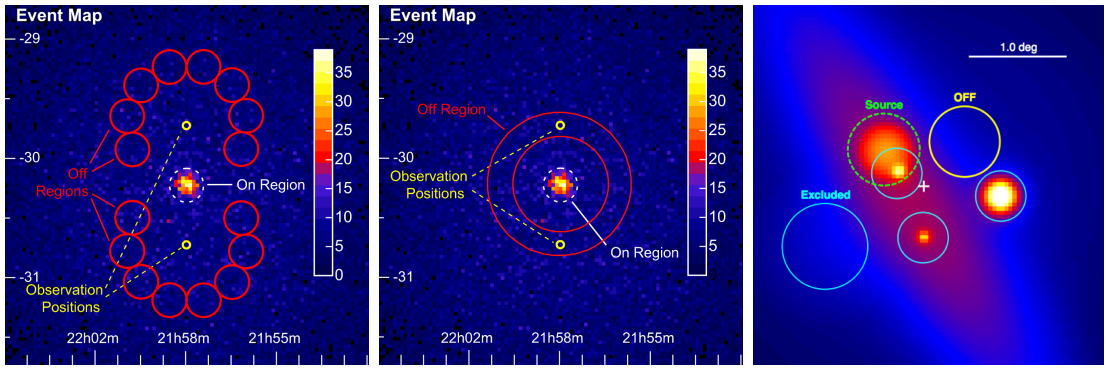

Figure 2.7: Left: Skymap that shows the positioning of on- and off-regions for the reflected background method. The source in the on-region was measured in wobble mode with two different pointing positions [Berge et al. 2007]. **Centre:** Skymap that illustrated the ring background method. The background in the on-region is estimated with the measured signal inside a ring shaped region around the source [Berge et al. 2007]. **Right:** Simulated field of view that contains many different overlapping sources. It is impossible to find an off-region that includes the same emission from other sources than the source of interest inside the on-region (green dashed circle). The template model background method provides a possibility to estimate the background in this complicated field of view [Mayer 2015].

which can be enclosed in on-regions rather easily. Furthermore, systematic uncertainties in the acceptance of the telescope can be counteracted by combining multiple observations with wobble offsets in different directions.

Ring background model

The Ring background model is primarily used for the generation of sky maps and for morphological studies. For each position in the field of view, the background counts are estimated by the counts within a ring-shaped off-region, centred around the position in question (see Figure 2.7 centre). The inner ring radius is chosen such that it is considerably larger than the on-region in order to minimise the influence by signal leakage from the source. For the outer radius, a value is chosen that results in an area of the ring of about seven times the area of the on-region. This factor was determined empirically. The background counts contained by the ring are scaled with the ratio between the solid angles of the on-region and the ring and with a correction factor that accounts for different background acceptances in the field of view. If the ring intersects with the on-region or an exclusion-region, this intersection area is excluded from the ring.
If the source of interest is quite large compared to the field of view, it may be challenging to construct a suitable ring for the background estimation, making this method unsuitable for largely extended sources.

On-off observations background method

In the early days of gamma-ray astronomy, a common way of estimating the background was to perform dedicated observations of a region of the sky where no source is expected. These off-observations were done temporally close to the observation of the source of interest. This makes for conditions as similar as possible so that the background acceptance in the off- and on-observation can be assumed equal. With one or multiple off-observations for an on-observation, the background counts at a given position in the latter can be estimated directly with the total counts in the off-observations at the same position in the field of view, scaled by the number of off-observations.
The advantage of this method is that it makes the analysis of arbitrarily large sources possible. The downside is that much more observation time is needed in order to perform the additional off-observations. In some cases it might also be impossible to do these because of fast varying conditions or regions in the sky that exhibit strong night sky background.

Template background model

An alternative to the on-off background model that does not need dedicated runs for background analysis but still enables the analyser to estimate the background in a given observation without using source-free regions in the same observation is the template background model. The application of this technique in IACT data analysis is rather novel. The idea of this method is to generate a template for the expected background rate in the whole field of view of a given observation by using data from source-free regions of observations that are taken under similar conditions. For H.E.S.S., this is possible as a large number of archival observations exist in whose fields of view no or just a few extragalactic sources are present which can be excluded before generating the template.
The creation of the model that is the base for the one used in this thesis is described in detail in Mohrmann et al. [2019]. This model uses 7063 runs from the H.E.S.S.-I Phase where all four telescopes participated in the data acquisition, equal to a total observation time of approximately 3240 h. In the first step, the runs are separated by their observation conditions into eight zenith angle and two azimuth angle bins. For each bin, a map is generated in a field of view coordinate system, where the origin corresponds to the pointing direction and the axes are aligned with the azimuth and altitude axes of the telescope. These maps consist of pixels with a size of $0.1^\circ \times 0.1^\circ$ and extends 7.5° in each direction. They are also binned in energy intervals using bin widths that are determined for each map individually such that all energy bins contain a sufficient number of background events. For large energies, where the number of background counts gets very low, this criterion is weakened a bit in order to avoid too large bins that would not represent the spectral shape of the background sufficiently. The maps are filled with all counts from the runs that fall into the same zenith-azimuth bin, excluding regions with known sources. The exclusion of these regions

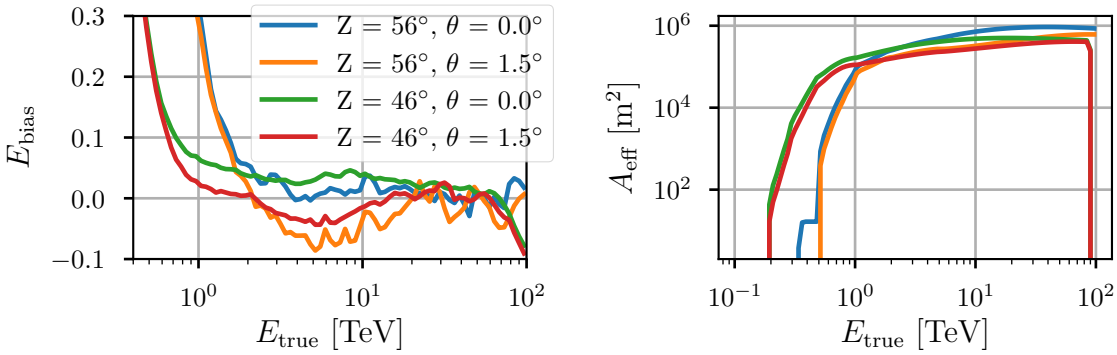

Figure 2.8: Left: Energy bias for two H.E.S.S. observations with different zenith angles Z at two different offsets θ from the pointing position. **Right:** Effective area for the same observations and configurations.

is compensated by applying appropriate weighting factors to the exposure when the average background rate is calculated from the data of different observations. After these maps have been filled, an individual background template can be generated for each run for which a background estimation is needed by rotating the coordinate system from the altitude-azimuth alignment to a right ascension-declination aligned system. The resulting templates are refined by applying scaling factors that account for additional observation-specific parameters like the optical efficiency of the telescope and the transparency of the atmosphere. As the last step, a smoothing algorithm is applied that attenuates statistical fluctuations in the model that exist due to the finite number of counts that were used in the model construction.
In order to improve the prediction power of the model for runs in which only three telescopes participated in the data acquisition, an additional model is generated that uses runs where the same telescope was also not active. As using only these runs would result into too few counts and too strong statistical fluctuations, artificial 3-telescope runs are generated by discarding data from one telescope in the event reconstruction. The background model template that was used for the analysis presented in Chapter 5 was created by L. Mohrmann and was made available for this thesis via private communication.

Instrument response functions

In order to perform a maximum likelihood analysis (described in the next Section), the instrument response functions (IRFs) have to be known. These functions, consisting of PSF, energy dispersion, and effective area, describe how an actual, physical signal is converted to data by the telescope and the low level analysis. They are determined via simulations. While PSF and energy dispersion have already been introduced above, the effective area will be discussed in the following paragraph.
The effective area is the component of the IRFs that is used to convert a number of detected counts into a physical flux. Monte Carlo simulations yield the effective area

as the number of detected events over the number of simulated events times the area where events have been simulated:

$$A_{\text{eff}} = \frac{N_{\text{det}}}{N_{\text{MC}}} A_{\text{MC}}. \tag{2.5}$$

The effective area is dependent on the true energy E_{true} of the photon, the instrument direction $\boldsymbol{p}$ (i.e. its direction relative to the pointing direction of the instrument), and numerous observation conditions like the zenith angle, the optical efficiency of the telescopes, and atmospheric properties. Therefore, the effective area is derived for every observation individually. The right panel of Figure 2.8 shows the effective area as a function of true energy for two runs and two different offset angles each. It can be seen that the effective area drops faster at low energies for observations with a larger zenith angle.

3D likelihood method

The main idea of the 3D likelihood analysis approach, which is described e.g. in Knödlseder et al. [2016], is to construct a likelihood function that expresses the likelihood that the observed data is compatible with a given model that depends on a set of parameters. This in done in two spatial and one spectral dimension, hence the "3D" in the name of the method. These parameters can be varied in a minimisation procedure to find the values that maximise the probability. Let i index individual observations in a dataset. Then the log-likelihood for one run can be written as:

$$-\ln L_i(M) = e_i(M) - \sum_k \ln P_i(\boldsymbol{p}'_k, E'_k, t'_k|M), \tag{2.6}$$

where the probability density $P_i(\boldsymbol{p}', E', t'|M)$ that, in observation i, an event with instrument direction $\boldsymbol{p}'$, measured energy E', and trigger time t' is observed given the model M, is logarithmically summed over all events k.
This likelihood function corresponds to an unbinned analysis approach, where the sum over individual events is calculated. In an alternative method, the likelihood is calculated as a sum of discrete spatial and spectral bins. Because photon properties and the IRFs are considered equal within each bin, this approach is an approximate method that approaches the unbinned method in the limit of infinitesimal small bins. In this thesis, solely the unbinned technique was applied. Therefore, the binned version will not be discussed further in the following.
The total number of events that is predicted by M during observation i is defined as $e_i(M)$:

$$e_i(M) = \int_{\text{GTI}} \int_{\text{Ebounds}} \int_{\text{ROI}} P_i(\boldsymbol{p}', E', t'|M)\ \mathrm{d}\boldsymbol{p}'\ \mathrm{d}E'\ \mathrm{d}t', \tag{2.7}$$

where the integral of the probability density is calculated over the whole observation time, divided into *Good Time Intervals* (GTI) of continuous data acquisition, the

complete energy range, and the *Region of Interest* (ROI). The total log-likelihood for a dataset can be obtained by summing over all runs:

$$-\ln L(M) = -\sum_i \ln L_i(M). \tag{2.8}$$

A full model description of a dataset can consist of multiple model components, indexed with j. The overall probability density is then calculated as the sum over all components:

$$P_i(\boldsymbol{p}', E', t'|M) = \sum_j P_i(\boldsymbol{p}', E', t'|M_j). \tag{2.9}$$

These components can either be celestial models $M_j^{\mathrm{S}}(\boldsymbol{p}, E, t)$ that describe sources in the sky or data models $M_{j,i}^{\mathrm{D}}(\boldsymbol{p}', E', t')$, which represent measured quantities that can depend on a specific observation. An example for a data model is the background model for residual, non-gamma events. Its event probability function is directly given by the model:

$$P_i(\boldsymbol{p}', E', t'|M_j) = M_{j,i}^{D}(\boldsymbol{p}', E', t'). \tag{2.10}$$

The probability density of a celestial model is derived by convolving the model with the instrument response function of the corresponding observation:

$$P_i(\boldsymbol{p}', E', t'|M_j) = \int_{\boldsymbol{p},E,t} R_i(\boldsymbol{p}', E', t'|\boldsymbol{p}, E, t) \times M_j^{\mathrm{S}}(\boldsymbol{p}, E, t)\ \mathrm{d}\boldsymbol{p}\ \mathrm{d}E\ \mathrm{d}t. \tag{2.11}$$

Here, the IRF $R_i(\boldsymbol{p}', E', t'|\boldsymbol{p}, E, t)$ denotes the probability that an event $(\boldsymbol{p}, E, t)$ is measured as $(\boldsymbol{p}', E', t')$ in observation i. It factorises into its individual components, namely effective area, PSF, and energy dispersion:

$$R_i(\boldsymbol{p}', E', t'|\boldsymbol{p}, E, t) = A_{\mathrm{eff},i}(\boldsymbol{p}, E, t) \times \mathrm{PSF}_i(\boldsymbol{p}'|\boldsymbol{p}, E, t) \times E_{\mathrm{disp},i}(E'|\boldsymbol{p}, E, t). \tag{2.12}$$

A celestial model itself may be factorised into a spatial, a spectral and a temporal component:

$$M_j^{\mathrm{S}}(\boldsymbol{p}, E, t) = M_{\mathrm{S},j}(\boldsymbol{p}|E, t) \times M_{\mathrm{E},j}(E|t) \times M_{\mathrm{T},j}(t) \tag{2.13}$$

A spatial model can either depict a point source or extended sources with e.g. a radially Gaussian shape:

$$M_{S,\mathrm{Gauss}}(\boldsymbol{p}|E, t) = \frac{1}{2\pi\sigma^2} \exp\left(-\frac{1}{2}\frac{\theta^2}{\sigma^2}\right), \tag{2.14}$$

where θ is the angular separation from the centre of the distribution and σ is the width of the source component. An important example for a spectral component is the power law model:

$$M_{S,\mathrm{PLaw}}(E|t) = k_0 \left(\frac{E}{E_0}\right)^{\gamma}, \tag{2.15}$$

where k_0 denotes a pre-factor or normalisation, E_0 the pivot energy, and γ the spectral index.

Data analysis procedure

The usual approach for the science analysis of a given gamma-ray dataset with the maximum likelihood method is the stepwise construction of a model that describes the data. One starts by performing a maximum likelihood fit with using only a template model background as a model description where the normalisations of the template of each run are used as optimisation parameters. After the fit, it is checked whether the data is well described by the model. If this is not the case, further components can be added to the model which describe additional gamma-ray sources in the field of view. These celestial model components can either be motivated by information from earlier analyses or observations in other wavelengths or by the observed residuals between model and data. With the new, extended model, a second fit can be carried out that varies both the free parameters of the previously used model and the parameters of the newly added components. When the parameters that maximise the likelihood have been found, the statistical significances of the newly identified sources are derived. This step is important because it prevents the analyser from falsely interpreting statistical fluctuations in the data as physically meaningful effects. The process of extending the model, fitting, and evaluating continues until the data is sufficiently described and no further statistically significant sources can be found. In the following paragraphs, the above mentioned steps are described in more detail.

Statistical significance of model components

The statistical significance of an added model component is evaluated via a likelihood ratio test. The likelihood ratio λ is defined as

$$\lambda = \frac{L_{\max}(M_0)}{L_{\max}(M_1)}, \tag{2.16}$$

with two maximised likelihoods of a model M_0 with m parameters and a more general model M_1 with h parameters. According to Wilks [1938], the test statistic $\mathrm{TS} = -2\ln(\lambda)$ is distributed like χ^2_k with $k = h - m$ degrees of freedom. In the case of a gamma-ray analysis, where a more general model M_1 means a model with an additional source, the parameter that represents the flux normalisation has some implications for this: Firstly, this parameter dominates the likelihood because if it is set to zero, the likelihood degenerates such that it does not depend on other spatial or spectral parameters of the added source any more. That means that the shape of the distribution of the TS can still be described well by χ^2_1 as Monte Carlo simulations have shown [Mattox et al. 1996]. Secondly, as sources with negative flux values are considered physically not sensible, the flux normalisation can not reach negative values and negative fluctuations in the likelihood are not possible. This leads to the fact that only over-fluctuations can occur in the likelihood ratio test and the distribution is best described with $\frac{1}{2}\chi^2_1$.
The probability of obtaining a test statistic of TS or more can be calculated as

$$p = \int_{\mathrm{TS}}^{\infty} \frac{1}{2}\chi^2_1(\zeta)\mathrm{d}\zeta = \int_{\mathrm{TS}}^{\infty} \frac{e^{-\zeta/2}}{2(2\pi\zeta)^{1/2}}\mathrm{d}\zeta. \tag{2.17}$$

By substituting $\eta = \zeta^{1/2}$, one obtains

$$p = \int_{\sqrt{\mathrm{TS}}}^{\infty} \frac{e^{-\eta^2/2}}{(2\pi)^{1/2}} \mathrm{d}\eta. \tag{2.18}$$

This is equal to the integral of the standard normal distribution from $\sqrt{\mathrm{TS}}$ to ∞. Because it is common practise to express significances in terms of numbers of standard deviations σ of the standard normal distribution, the significance of the additional component of M_1 can in this case be written as

$$S = \sqrt{\mathrm{TS}}\,\sigma. \tag{2.19}$$

Residual significance

In order to evaluate how good a model describes a given dataset, residual significances can be calculated. The idea is to compare a number of observed counts to a number of predicted model-counts. These counts can either be integrated over small spatial bins, with the aim of creating a residual significance map, or over a larger area to search for residual excess in a given region of the sky. The significance gives the $1 - p$ quantile of the standard normal distribution where p is the probability that the number of observed counts can be explained by the model. Li et al. [1983] describes the calculation of the significance by using a number of on-counts and a number of off-counts. While in the case described in the article, both numbers are affected by statistical fluctuations, the model prediction in a maximum likelihood analysis is considered to be exact. For this reason, the derivation given in the following is modified to be valid for a number of measured counts N_D and a number of predicted counts N_{pred}. The likelihood for the null-hypothesis that the observed counts can be described by model M_0 equals

$$L(M_0) = P(N_D|\langle N_D\rangle = N_{\mathrm{pred}}) = \frac{{N_{\mathrm{pred}}}^{N_D}}{N_D!} e^{-N_{\mathrm{pred}}}, \tag{2.20}$$

where $\langle N_D\rangle$ denotes the expectation value of N_D and a Poissonian distribution of the counts is assumed. The likelihood for the alternative hypothesis that there is an additional source that accounts for $N_S = N_D - N_{\mathrm{pred}}$ counts can be written as

$$L(M_1) = P(N_D|\langle N_S\rangle = N_D - N_{\mathrm{pred}}) = P(N_D|\langle N_D\rangle = N_D) = \frac{{N_D}^{N_D}}{N_D!} e^{-N_D}. \tag{2.21}$$

Applying 2.19, the significance is

$$S = \sqrt{-2\ln(\lambda)}\ \sigma = \sqrt{-2\ln\left(\frac{L(M_0)}{L(M_1)}\right)}\ \sigma = \sqrt{-2\ln\left(\frac{{N_{\mathrm{pred}}}^{N_D}}{{N_D}^{N_D}} e^{-N_{\mathrm{pred}}+N_D}\right)}\ \sigma \tag{2.22}$$

$$= \sqrt{2}\sqrt{N_D \ln\left(\frac{N_D}{N_{\mathrm{pred}}}\right) + N_{\mathrm{pred}} - N_D}\ \sigma. \tag{2.23}$$

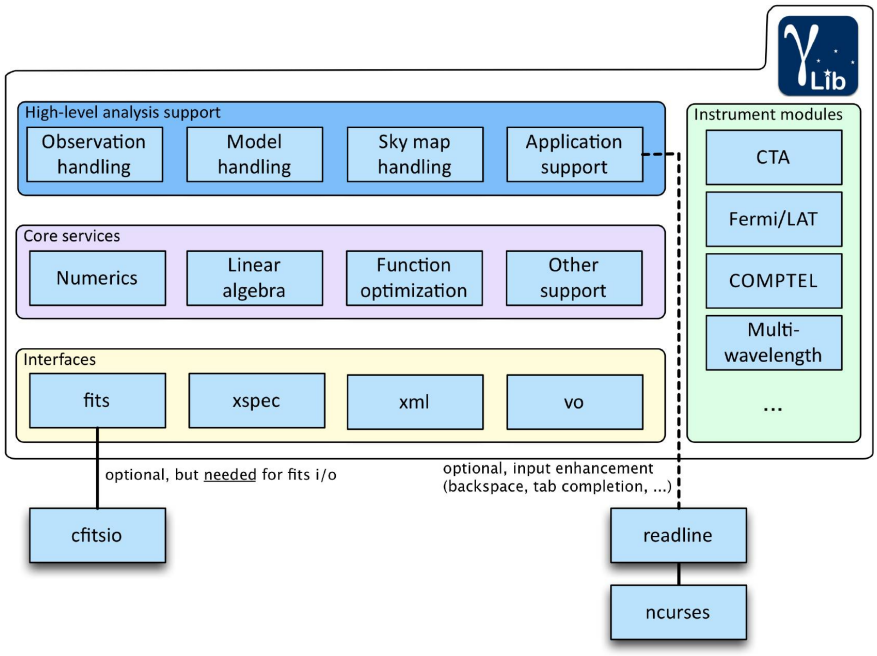

Figure 2.9: Structure of the software library GammaLib. Image credit: Knödlseder et al. [2016]

To also allow for negative significances if the model over-predicts the measured counts, a sign function is added:

$$S = \mathrm{sign}(N_D - N_{\mathrm{pred}}) \quad \sqrt{2}\sqrt{N_D \ln\left(\frac{N_D}{N_{\mathrm{pred}}}\right) + N_{\mathrm{pred}} - N_D}\ \sigma. \tag{2.24}$$

If $N_D = 0$, the significance is calculated as:

$$S = -\sqrt{2N_{\mathrm{pred}}}. \tag{2.25}$$

If $N_{\mathrm{pred}} = 0$, the calculation of a significance is meaningless because it is impossible to detect any counts if the number of expected counts is exactly zero.

GammaLib and ctools

GammaLib is an open-source software library that is written in C++ but also supports a Python interface and implements a framework of basic features that can be used for the analysis of gamma-ray data [Knödlseder et al. 2016]. On top of this foundation, the software package *ctools* is built. It consists of several tools or applications that are written in C++ and Python and can be run either in their binary form or via a Python interface. These tools can be combined to a complete gamma-ray analysis. ctools is one of the proposed analysis software solutions for high level analysis of future CTA data.

Structure of GammaLib

Gammalib is structured into different modules which can be grouped into three layers (see Figure 2.9). The bottom layer handles the interfaces to different input and output formats. Most of the data, like event lists and IRFs, are accessed from and saved to FITS-files [Wells et al. 1979]. For this, the library *CFITSIO* by NASA's HEASARC is used. This software library is the only external dependency of GammaLib that is required for data analysis. Another frequently used format is XML, which is chosen to ease human editing of certain files like e.g. the definition of models or the specifications of observations. The medium layer of GammaLib is dedicated to core services like numeric calculations, linear algebra, and function optimisation. The top layer contains modules that constitute the higher levels of gamma-ray analysis. In these, models, observations, celestial and data models, and sky-maps are handled. Additionally, another module contains the framework for applications like the ones in ctools. Besides these three layers, whose modules work independent of the instrument that obtained the analysed data, there is also a module for each supported instrument. Besides the CTA-module, which can be used for data from all IACTs, other instruments like Fermi-LAT and COMPTEL are supported. This multi-instrument approach can be used to carry out multi-wavelength analyses.

Components of ctools

The design of ctools is based on *ftools* [Pence et al. 1993] and its modular work flow. The software consists of a number of individual tools that each perform a well-defined step in a gamma-ray analysis. The modularity enables the analyser to construct a work flow that is optimised for a specific data set and for a given physical problem. Each tool has defined inputs and outputs in which the latter can again be used as inputs for other tools. The tools can either be executed in their binary form by consecutive calls from the command line or, thanks to the Python interface, combined in a Python script or a *Jupyter notebook*[1]. An example for application of ctools is *ctlike*, which takes as input a container of observations with a model description and outputs the best fit model that is obtained via a maximum likelihood approach. A more in depth description of the capabilities of ctools is given in Knödlseder et al. [2016] and the ctools user documentation[2].

Status of the GammaLib/ctools software

Although the software is still being developed further by a large community, which the author of this thesis is also an active part of, it has already been applied to carry out analyses of different science cases. In Knödlseder et al. [2019] and Mohrmann et al. [2019] it was shown that an analysis of H.E.S.S. data with ctools yields results compatible with those derived with the established, proprietary software of the H.E.S.S.

[1] `https://jupyter.org`

[2] `http://cta.irap.omp.eu/ctools/users/index.html`

experiment. Such checks and also analyses like the one in this thesis are very valuable for the preparation of the software for analysis of CTA data that will be performed once this future instrument is in operation. The version that is used for the analysis in this thesis is 1.6.3.

Chapter 3

A pointing solution for the MST

The term *pointing* in the context of IACTs describes the ability to transform a position in the focal plane of a telescope to a point in the sky. Pointing or pointing direction sometimes also refers to the direction a telescope is aligned to. For an ideal telescope, the pointing could be calculated at any given time by taking into account the location and geometry of the telescope and the current angular displacement around the axes of its mount. In reality, telescopes are subject to construction imperfections, mechanical deformations, and measurement errors. Therefore, other means have to be applied to determine the actual pointing. An exact pointing calibration for a telescope is crucial for the directional reconstruction of gamma-ray showers and with that also for the morphological analysis of gamma-ray sources.
This chapter starts with the introduction of mechanical problems that can affect the alignment of a telescope. The second part deals with means that are applied to measure such pointing errors in current instruments using H.E.S.S. as an example. In the rest of the chapter, the so called SingleCCD pointing concept, which is the desired pointing solution for the MST, is introduced and the design and performance tests of a specific solution, which was developed in the scope of this thesis, are presented.

3.1 Reasons for mis-pointing

With *mis-pointing* the deviation between the nominal or expected pointing and the actual pointing is described. Mis-pointing can arise from different reasons [Lennarz 2012]. They can be divided in two categories, namely elastic and inelastic effects. Elastic effects are by definition reproducible, meaning that they do not or very slowly change over time. They can be measured and modelled for several observations. For example, a telescope can be built with an imperfect geometry such that the azimuth axis is not precisely vertical or not perpendicular to the altitude axis. The shaft encoders that are used for measuring the current angular displacements can exhibit offsets and non-linearities. The telescope structure can also be bent by gravity which leads to displacements and rotation of the Cherenkov camera or to deformations of the mirror dish. Examples for inelastic effects, which vary on short time scales

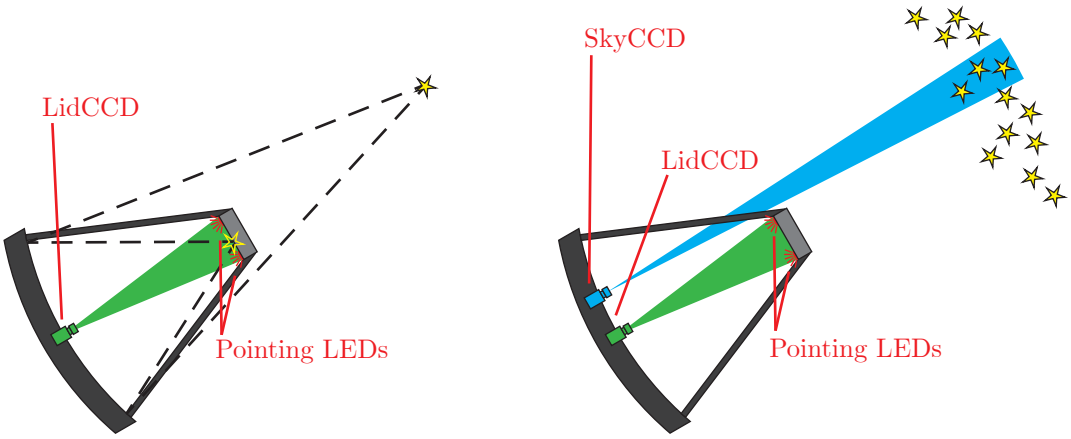

Figure 3.1: Left: Schematic drawing of a measurement during a pointing run. A star in the night sky is imaged to the closed lid of the Cherenkov camera by the mirror of the telescope. The positions of the star image and of the pointing LEDs are captured by the LidCCD camera. **Right:** Drawing of a precision pointing measurement. The LidCCD camera captures the positions of the pointing LEDs (green area) while the SkyCCD records images of a part of the night sky (cyan area).

and therefore can not be modelled, are deformations by wind load or temperature variations and the mechanical impact of dirt in the mechanics.

3.2 Pointing at H.E.S.S.

The pointing calibration of H.E.S.S. is carried out in two steps. Mis-pointing by elastic effects is measured in dedicated calibration runs called *pointing runs*. The deviation from the nominal pointing is measured as a function of azimuth and altitude for observation directions distributed isotropically over the hemisphere above the telescope. For that, the telescopes are pointed at bright stars in the sky. An optical camera, the *LidCCD*, that is mounted to the mirror dish of the telescope, then records an image of the focal plane of the telescope. During these measurements the focal plane instruments are covered by a diffusely reflecting lid. A schematic drawing of the setting can be seen in Figure 3.1 (left). At an ideal telescope, the image of the bright star, reflected by the mirror dish of the telescope, should be located exactly in the centre of the focal plane. The position relative to the focal plane can be determined via the recorded LidCCD image with the help of positioning light-emitting diodes, the so called *pointing LEDs*, that are attached to the Cherenkov camera. The deviation from the ideal central position defines the mis-pointing at the current pointing position. A mechanically motivated model is then fit to the acquired data for several telescope alignments. This model is then used for calculating the predicted mis-pointing at arbitrary observation directions without additional measurements during gamma-ray observations.

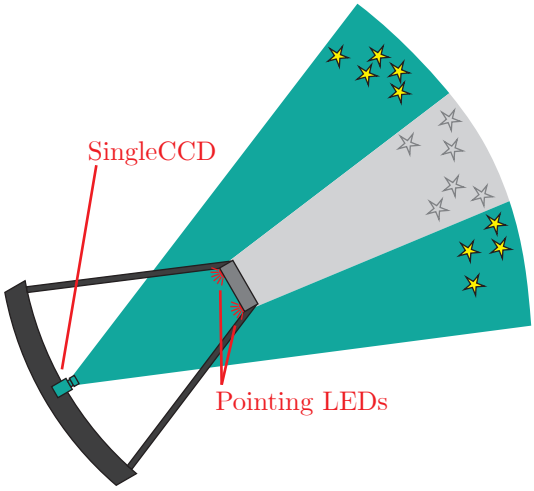

Figure 3.2: Schematic view of the setup of a SingleCCD camera. The field of view includes the Cherenkov camera and parts of the sky (turquoise area). Some areas of the sky are blocked by the telescope structure (light grey area).

To account for inelastic effects, pointing corrections can also be measured during observations. This procedure is called *precision pointing* and is used in addition to the standard pointing run technique for observations where high pointing precision is desired [Lennarz 2012]. The technique uses a second optical camera, the *SkyCCD* which is mounted to the mirror dish with a small offset from the telescope's optical axis, facing the same direction as the telescope (see Figure 3.1 right). With this camera, a small part of the night sky can be imaged. With the positions of identified stars in an image, the pointing direction of the telescope can be determined. At the same time, the LidCCD also takes an image in which the positions of the pointing LEDs and thereby the position of the Cherenkov camera can be identified. With this information, a momentary mis-pointing can be calculated. This technique is only used as a supplementary method and not in order to replace the standard pointing procedure because it is less reliable due to possible hardware failure or unusable SkyCCD images with too few identified stars. Furthermore, it is not possible to measure the imaging properties of the mirror dish. Therefore the assumption is made that the deformations of the mirror dish are solely elastic and completely described by the pointing model derived via pointing runs.

3.3 The SingleCCD concept

The *SingleCCD concept* is a novel technique for pointing measurements that uses only one camera for both off-line pointing calibration and on-line measurements. The SingleCCD replaces the LidCCD but it has a larger field of view. This enables it to capture not only the position of bright star spots on the closed Cherenkov camera lid but also both the position of the pointing LEDs and the bright spots of stars in the night sky that appear around the Cherenkov camera in one image. This eliminates

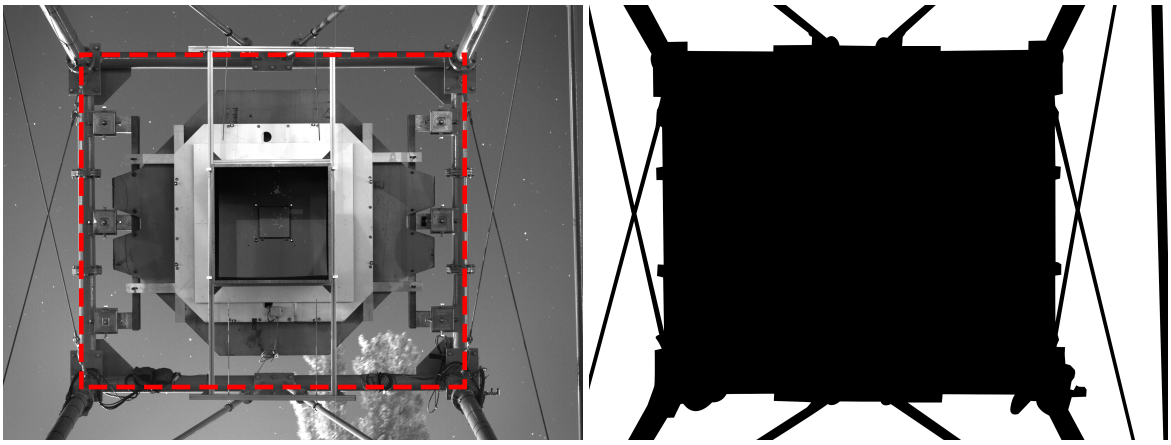

Figure 3.3: Left: Image recorded with the SingleCCD camera prototype at the MST prototype telescope in Berlin. The red dashed rectangle marks the area that will be covered by the camera. The brightness of the image was adjusted for better visibility. **Right:** Mask that is generated from the left image and that selects areas in the image where spots by stars can be used for the image analysis. These selected areas are drawn with white colour.

uncertainties that result from relative movements between SkyCCD and LidCCD in a two camera solution. Also maintenance and installation costs can be reduced. This comes with the expense of less resolution due to the larger field of view of the SingleCCD while using a CCD chip with equal numbers of pixels. The method has been tested at the H.E.S.S. telescopes [Lennarz 2012] and its feasibility for CTA has already been studied [Tiziani 2015].

Field of view

The SingleCCD camera is mounted roughly in the centre of the dish of the telescope, facing the Cherenkov camera and with that the observation direction of the telescope. The focal length of the optics is chosen such that both the Cherenkov camera and a certain area of the sky can be imaged simultaneously as shown in Figure 3.2.

During pointing runs i.e. outside of data acquisition, the part of the field of view that includes the Cherenkov camera can be used to track star spots on the closed lid of this camera as discussed in Section 3.2. For on-line pointing measurements, the images of stars in the outer parts of the images can be used for calculating the pointing direction of the telescope. For this, a large enough part of the camera field of view has to be not blocked by the Cherenkov camera and its support structure. This can be accomplished by using lenses with shorter focal length. The downside of shorter focal lengths is the reduction of resolution i.e. one pixel corresponds to a larger area in the sky. This leads to less precise reconstructions of the pointing direction of the telescope due to less precisely determined star-spots in the images. Another problem arises from the fact that merely stars close to the edges of the field of view and therefore far away from the optical axis of the lens are used for the reconstruction. In this regime, real lenses exhibit the largest image distortions which typically increase with shorter focal

length. The effects of radially symmetric distortions can be compensated if the field of view is chosen such that an equal amount of stars is observed next to all sides of the Cherenkov camera.
For the SingleCCD prototype camera for the MST, a lens with a focal length of 50 mm is used. This value is a good compromise between the above described pros and cons and a device with suitable specifications is available commercially (see 3.4). In the left part of Figure 3.3, an image recorded with such a lens at the MST prototype telescope in Berlin is shown. The camera support structure (CSS) and some focal plane instruments with a projection screen can be seen in front of a tree and the night sky. The actual Cherenkov camera had not been installed at the telescope at the time when the image was recorded. The inner part of the CSS that is marked in the image will be occupied by that camera during data acquisition. In the right part of Figure 3.3, a mask is shown that specifies for each pixel whether it shows a part of the night sky and whether it can be used for the reconstruction of the pointing direction of the telescope. This mask removes about 62 % of the image area. In Chapter 4, it will be shown that the remaining 38 % of the image are sufficient for the pointing calibration.

Pointing requirements for CTA

There are several properties that a pointing solution has to fulfil in order to be used at CTA telescopes. The whole system should be reliable, so that as few as possible components have to be exchanged. This especially makes demands on the utilised hardware. The camera itself should be capable of taking the required number of images. Named camera, if not weather-proof itself, has to be installed inside a housing that shields the optics and electronics from environmental impact like water and dust. The housing also has to have such thermal properties that the temperature of the camera stays within the operating range stated by the manufacturer when it is taking images. Outside of observations, when the system is not taking images, the temperature inside the housing has to stay within the specified survival temperatures. Additionally, the housing has to be mechanically rigid enough such that the camera does not move relative to the telescope mirror dish where it is mounted.
The software that is used for analysing the images should be able to derive the information that is needed for the pointing calibration. More specific, this means that the position of the Cherenkov camera, star spots on the latter, and the alignment of the telescope have to be derivable to a satisfying degree of precision. As stated by Hinton et al. [2018], the pointing precision of an MST should be $< 7''$ per axis for optimal observation conditions.

3.4 Camera hardware

One goal of this thesis is to develop a SingleCCD pointing device that can be mounted to an MST and connected to the telescope's systems in a plug-and-play like fashion. This ensures easy construction and replacement of the whole system in the case of

malfunctions. The following chapter describes such a system and reports about tests that have been carried out in order to show its applicability.

Camera

The camera that is used for the studies in this thesis is an astronomical camera *Aspen CG8050-S-G01-HSH* from *Apogee Imaging Systems*. It makes use of a *Kodak KAI-08050* interline, monochrome CCD (charge-coupled device) sensor. The sensor has a resolution of (3296×2472) pixels at an active image size of 18.13 mm × 13.60 mm, resulting in a pixel edge size of 5.5 µm. It supports electronic shuttering which eliminates the need for a mechanical shutter and with that also the abrasion effects of such a device. The camera has an internal, active chip cooling implemented via a Peltier device that is attached to the backside of the CCD chip. The other side of the thermoelectric cooler is connected to a heat sink that is ventilated by two fans. In this factory-provided setting, the camera can be operated at environmental temperatures between −20 °C and 40 °C according to the manufacturer. A C-mount mounting supports the attachment of compatible lenses to the camera. Lenses with other mounts like an F-mount can be used by interconnecting an adapter. The camera is operated at a voltage of 12 V and data can be transferred either by a USB 2.0 or a 2 MHz Ethernet interface. The free software library *libapogee* (version 3.0.3179-Fedora21-x64) is used on a *Scientific Linux* (version 6.6) virtual machine for communicating with the camera.

Optics

For imaging light to the chip of the camera, a *Nikon AF NIKKOR 50 mm f/1.8D* photographic lens is used. It is constructed with 6 diffracting elements in 5 groups and shows very little image distortion in comparison to other lenses with a similar fixed focal length [Rockwell 2014]. It shows some coma close to the image corners. Coma is an effect that is caused by spheric aberration and distorts bright spots to banana-like shapes. As this lens features an F-mount for the connection to the camera, an adapter to C-mount is used. The objective is focussed manually to the hyperfocal distance, using a chequerboard pattern at a distance of 32 m. With this lens, the camera can record images with a field of view of about $20^\circ \times 15^\circ$.

Housing

The housing that is developed in the scope of this thesis is based on the design of the one introduced by Tiziani [2015] with some modifications. A schematic drawing of the casing can be seen in Figure 3.4. The major part of its body is made from aluminium which is both reasonable lightweight and durable. The light entry window for the camera is covered by an anti-reflective coated glass plate, surrounded by an active heating element to counteract the formation of fog and ice on the glass. The

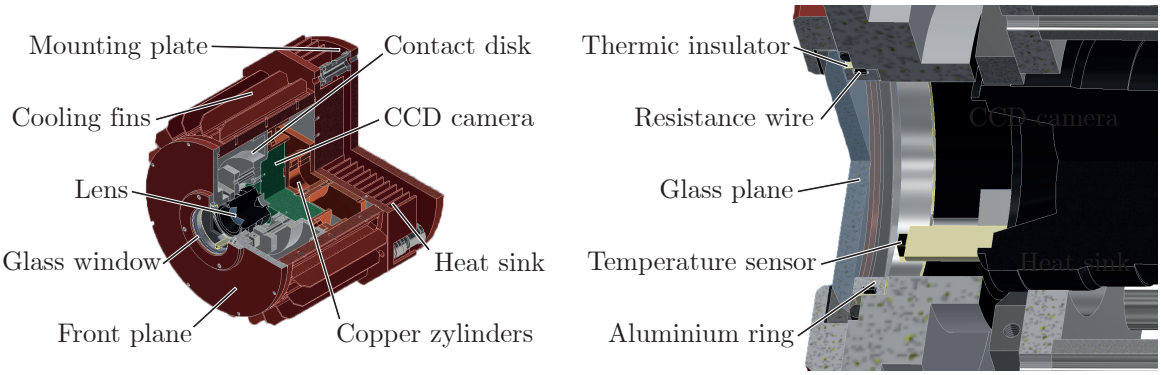

Figure 3.4: Left: Schematic drawing of the CCD camera housing. **Right:** Detailed drawing of the front part of the housing with the window heating element.

camera is mounted inside the housing on four steel rods and is also thermally coupled to the outer walls of the housing via a contact disk at the front of the camera. The heat sink and fans of the camera are removed so that the warm side of the Peltier device of the camera can be thermally connected to the backplane of the housing via an arrangement of two interlocking hollow cylinders of copper. The sides of the housing feature some cooling fins and the backplane itself is constructed as a heat sink that passively cools the device. In the front part of the housing, a small circuit board is located that hosts a temperature and a humidity sensor and is responsible for controlling the heating element of the front window. Three connector sockets are placed at the bottom of the housing. They are used for connecting the camera with a power supply, the network, and the programmable logic controller of the telescope for sensor readout. The backside of the housing is connected to a mounting plate via three screws and spherical washers and ball cups that allow for some tilt adjustment when fixing the casing to the telescope. The outer metal surfaces of the housing are coated red according to the steel structure of the MST for durability reasons and because this colour represents a good trade-off between absorption of stray light at night and reflection of daylight that would otherwise heat up the structure too much. All connections including the sockets on the bottom are sealed to protect the inside from dust and water.

3.5 Thermal tests of the housing

In the scope of this thesis, extensive tests of the thermal capabilities of a prototype of the housing have been carried out. One important goal is to show that the temperature inside the housing stays within the range where the manufacturer of the CCD camera guaranties a save operation of the imaging device. This has to be the case both at night during operation of the telescope and the pointing camera and during daytime when the device is not in use in order to ensure that the camera is not damaged. It is also important to check whether the recording of images could be disrupted by the formation of fog or ice on the front window. Lastly is has to be proven that the camera

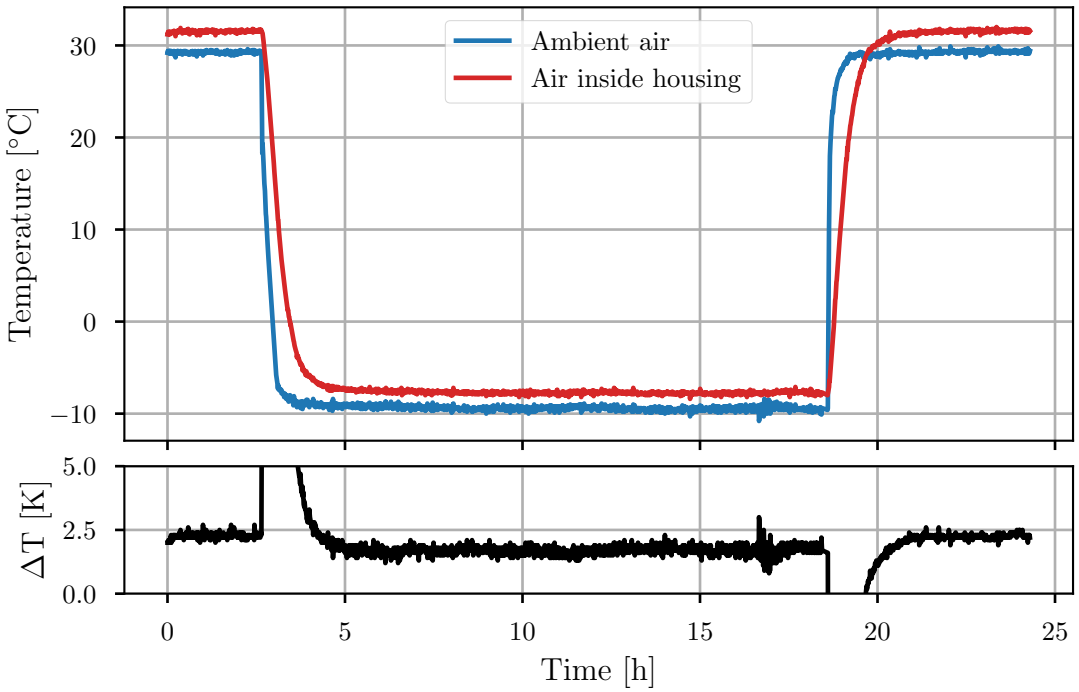

Figure 3.5: Top: Trend of the temperatures inside and outside of the housing prototype during a measurement in the temperature chamber. **Bottom:** The difference between the two temperatures.

chip can be kept at one stable temperature for the whole range of environmental temperatures. CTA requirements state that all components have to be operational at ambient temperatures between −5 °C and 25 °C.

Operating temperature

The extremal save temperatures at which *Aspen CG8050-S-G01-HSH* can be operated are −20 °C and 40 °C. It was tested by Wong [2018] in a laboratory set-up that the temperature inside the housing does not exceed this range. For this, the complete housing with the camera was put into a temperature chamber that made it possible to expose the construction to temperatures that are expected for the CTA construction sites. The temperature at different spots was monitored with a digital thermometer. The result of one of these measurements is shown in Figure 3.5. It is obvious that the air temperature inside the housing follows the environmental temperature in the chamber at a small, positive offset. When thermal equilibrium is reached, the air inside the housing is roughly 2.5 K warmer than the ambient air. This means that an internal temperature of more than 40 °C is not expected to be reached at environmental temperatures of lower than 35 °C.

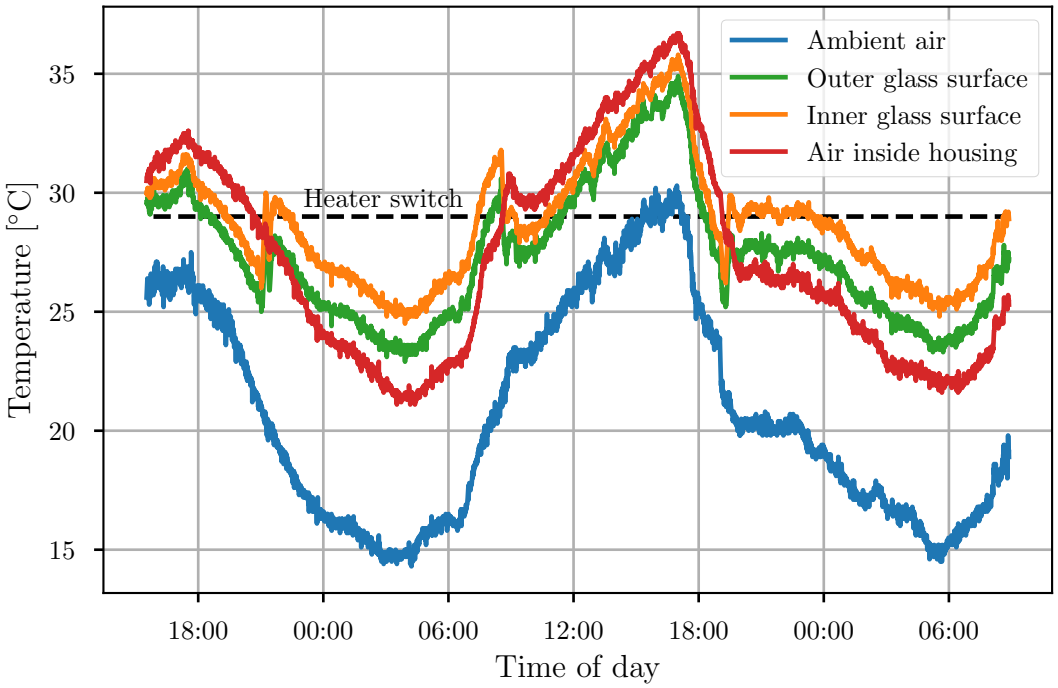

Figure 3.6: Thermal trend at different locations of the housing prototype in an outdoor measurement. The data was recorded during a warm period in summer. The temperature inside the housing at which the heating of the front window is toggled is indicated by the dashed black line.

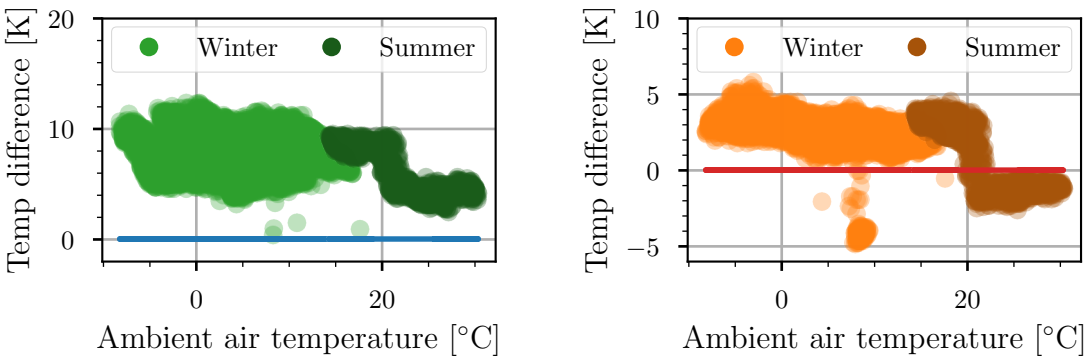

Figure 3.7: Temperature differences between window surface and the adjacent air as a function of the environmental temperature. The data was acquired in two measurement campaigns, one during winter and one during summer. **Left:** outer surface; **Right:** inner surface.

Fog and ice

During a test of an earlier version of the camera housing at the MST prototype telescope in Berlin [Garczarczyk 2016], some fog or ice formation was observed on the front window. This became manifest in the fact that no stars could be seen and also the usually visible telescope structure was dimmed in some images.
Water vapour condensates or deposits on a surface if the air-water mixture close to the surface is saturated. As the amount of water that a certain amount of air can hold increases with increasing temperature, water can not condensate or deposit on a surface that has a higher temperature than the gas. That means that one can exclude the formation of solid or liquid water on the glass window of the housing if one keeps its surface warmer than the adjacent air. This assumption is conservative in the sense that it also works in the worst case scenario where the relative humidity of the air is at 100%.
To ensure that the glass window is warmer than the adjacent air, a heating element is installed in the housing. This is illustrated in Figure 3.4. In comparison to earlier iterations of the housing prototype, the window is also scaled down to a minimum size allowed by the opening angle of the camera optics. This is advantageous because of the smaller area that has to be heated. The heating element itself is realised as a resistance wire that is coiled up around an aluminium ring which is installed adjacent to the glass window. This ring is thermally decoupled from the rest of the metal part of the front cover so that the heat is primarily transferred to the glass. A temperature sensor close to the inner surface of the glass is used as an input device for a small electronic board that controls the operation of the heating element. The logic of the control is kept very simple. The heating is switched on or off depending on whether the sensor measures a temperature below or above a given threshold. This control is needed to counteract overheating of the housing during daytime or very warm nights. The performance of the window heating has also been tested by Wong [2018]. During these tests, the temperatures of the inner and outer surfaces of the window are measured and compared to those of the adjacent air inside and outside the housing respectively. A realistic operation is simulated both inside a temperature chamber and under the open sky. Figure 3.6 shows the thermal trend of the measured points in an outdoor measurement. One can clearly see the points where the air temperature inside the housing crosses the threshold of ~ 29 °C and the window heating is turned on or off by the integrated control, depending on whether the temperature is rising or falling. When the heater had been switched on, the temperature of the inner glass surface raises above the inner air temperature and stays there until the heater is switched off again when the temperature falls below the threshold.
Figure 3.7 shows the measured temperature difference between the glass and the adjacent air. The data was recorded in two measurement campaigns, one in the winter and one in the summer. The heating switch on point can be clearly seen at ~ 22 °C ambient temperature. The outer surface of the window stays warmer than the surrounding air in the whole measured range. On the inside surface, the temperature rises above that of the air inside the housing when the heating is in operation. The points at ~ 8 °C where the surface temperature was detected lower are likely incorrect measurements

caused by a malfunction of the temperature logging device. A slight jump between the two measurement campaigns in winter and summer can be seen. This can have various reasons: Between the measurements, the temperature sensors where removed and reattached which results in slightly different thermal properties. Besides, the outer surface of the housing was painted between the measurements which changes its heat irradiation efficiency.

Chip temperature

It has been shown by Wong [2018] that a stable temperature of the CCD-chip is crucial for an exact pointing calibration. Laboratory measurements showed that a temperature change of 5 K can result in an inaccuracy of 1.6″ due to thermal expansion of the chip. The integrated electronics of Aspen CG8050-S-G01-HSH support a temperature control down to 60 K below ambient with a stability of 0.1 K. As this specification is not necessarily valid for the camera if its heat sink and cooling fans are removed and if it is integrated into the custom housing, the thermal controlling capabilities have been tested in this configuration. A suitable temperature at which the CCD chip can be operated at environmental temperatures in the whole range stated by the CTA requirements has to be determined. The minimum chip temperature that the camera electronics allowed when the housing was exposed to an ambient temperature of 30 °C was −23.5 °C [1]. At an ambient temperature of −10 °C, the maximum possible temperature that could be set by the cooling control was −22.6 °C. This can be explained with a minimum cooling power that is given by the electronics or software of the camera. Operating the chip at a temperature closer to that of the environment is only possible by switching of the cooling control completely.
The results of the described measurements suggest that a chip temperature should be chosen such that $-23.5\,°\mathrm{C} \leq \vartheta_{\mathrm{chip}} \leq -22.6\,°\mathrm{C}$. In further tests, it was confirmed that a chip temperature of −22.6 °C is suitable for the required range including a safety margin the CTA requirements of 5 K.

3.6 Long term test at MAGIC telescope

In order to test the housing prototype and imaging system under conditions as close to an application in CTA as possible, the prototype was also mounted to one of the two MAGIC telescopes [MAGIC Group 2020]. These telescopes are located on La Palma at the exact location where CTA-North is planned to be built. The SingleCCD prototype has been operated there for more than two years, starting on 7th July 2018, with the objective of obtaining images for tests of the analysis software and of identifying problems with the hardware.
The device is installed in the central region of the mirror dish (see Figure 3.8), pointing

[1] This measurement was performed with a preliminary version of the housing prototype with different window heating switch-on temperature and without the exterior paint.

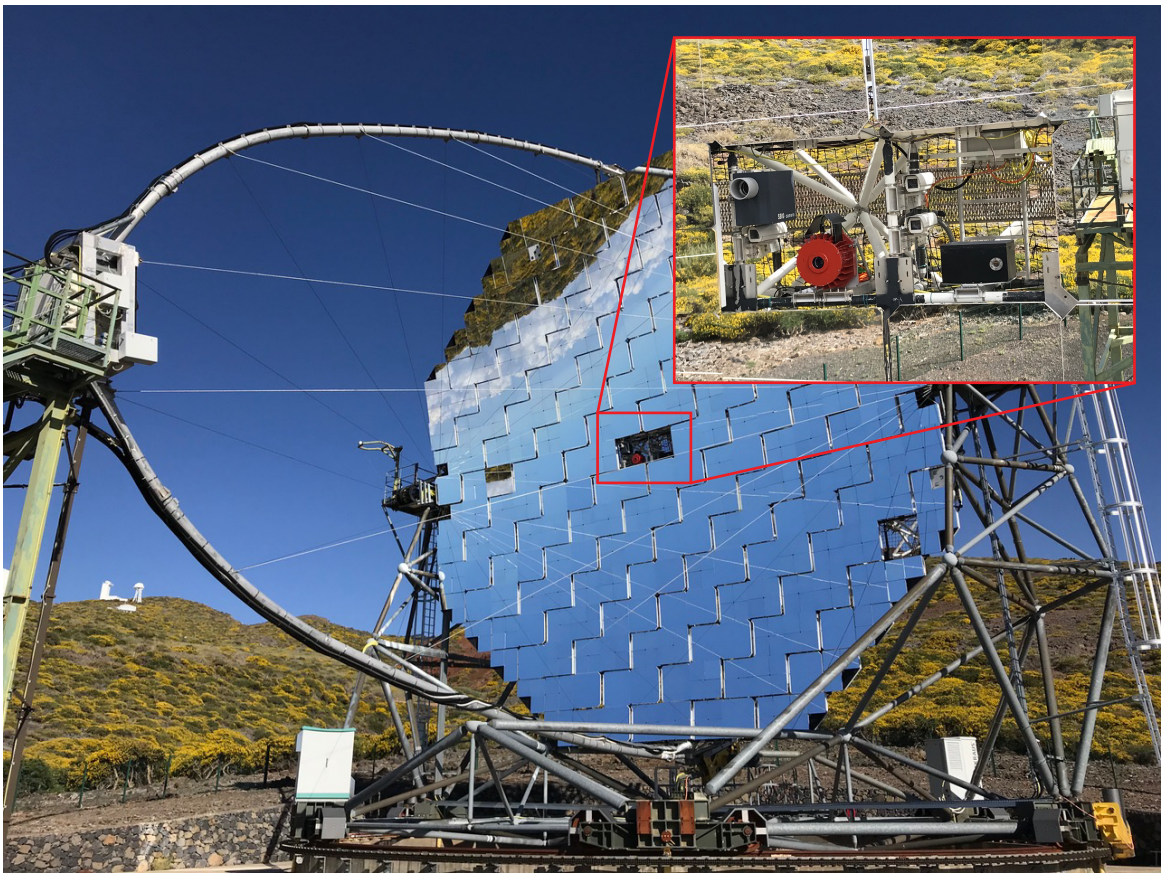

Figure 3.8: Photograph composition of one of the MAGIC telescopes with the red SingleCCD prototype installed in the centre of the dish. Image credit: Markus Garczarczyk

towards the Cherenkov camera. The camera is programmed to take images in fixed intervals during night time, independent of the operation of the Cherenkov telescope it is mounted on. The chip cooling is switched on at the beginning of the night and is set to −22.6 °C until the end of the night where it is switched off again. The measured temperature of the CCD chip is logged during day- and night-time. Figure 3.9 shows the cooling down procedure at the beginning of the night superimposed for multiple days, taking data into account that was acquired between 7th July 2018 and 10th January 2020. It can be seen that the desired temperature is always reached after ~ 30 min where it stays constant. On 28th October 2018, the frequency at which temperature values are recorded was decreased, which manifests itself in two vertical lines in the plot at ~ 400 s and ~ 750 s.
The images that were recorded during the measurement campaign at the MAGIC telescope are used for studies of the procedure of analysing the images and using them for pointing calibrations. This is discussed in detail in Chapter 4.

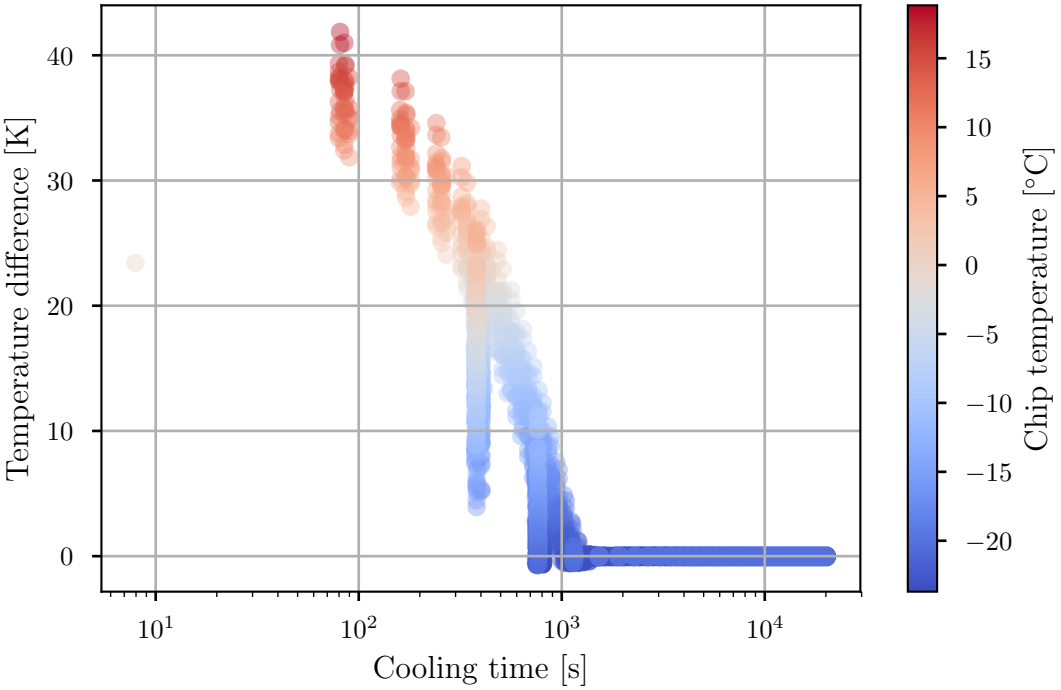

Figure 3.9: Temperature measurements for multiple cooling cycles of the CCD chip during the test run at MAGIC. The difference between measured and set temperature is plotted against the time since when the cooler is switched on. The colour scale denotes the measured temperature of the CCD chip.

3.7 Summary

In this chapter, a prototype of a complete SingleCCD pointing device that consists of an astronomical camera inside a custom built housing has been introduced. Laboratory and field tests have shown that the thermal properties of the construction ensure a save operation of the camera in environmental conditions corresponding to the requirements of CTA. Measurements indicate that the included heating device, that warms up the front window of the housing, keeps the glass plane free of fog and ice. Furthermore an optimal temperature to which the chip of the CCD camera can be cooled has been identified. A long term test at the MAGIC telescopes on La Palma has been discussed. This measurement campaign confirmed the stability of the CCD chip temperature and the functionality of the camera electronics.
During the investigations of the hardware, it turned out that the CCD chip that is built in Aspen CG8050-S-G01-HSH will no longer be produced by the supplier. That means that the pointing device as it is characterised in this thesis will not be applied for the production of CTA. Currently, the application of other cameras is under investigation. A new camera with a different form factor will make adjustments to the design of the housing necessary. As soon as a usable alternative is found, the tests described in this thesis will have to be repeated with the new hardware components.

Another test campaign at one of the H.E.S.S. telescopes is also planned.

Chapter 4

Pointing image analysis

Another key aspect of this thesis is to show that the images taken by a SingleCCD camera can be used to perform pointing calibrations that achieve the desired precision that is demanded by the requirements of CTA. In doing so, the main focus is on the reconstruction of the viewing direction of the pointing camera, i.e. the central pixel position of an image transformed to the sky, by analysing the positions of star spots in a given image. For simplification, this direction will be called *pointing direction* in the following.
The problem that has to be solved in order to derive the pointing direction from an image is the generation of a coordinate transformation between pixel coordinates in the image and celestial coordinates on the sky. There are some existing software solutions that implement algorithms for the construction of such a transformation. One example is *astrometry.net* [Lang et al. 2010]. The application of this software for SingleCCD images has been investigated by Tiziani [2015].
During the studies for this thesis, it was discovered that the precision of the solutions provided by astrometry.net is often not satisfying. This is likely caused by the fact that this software does not provide a proper way to deal with images where large parts of the sky are obstructed, like in the case of SingleCCD pointing images by the Cherenkov camera and its support structure. Although the source code of astrometry.net is publicly available, it is nearly impossible to adjust the software as most of it is written in a very complex and nested way with little documentation available.
In the first part of this chapter, a self-developed software library called *libPointing-MST*, which is based on the algorithms of astrometry.net, is introduced. In the second part, its capability of setting up the above-mentioned coordinate transformations is studied in detail.

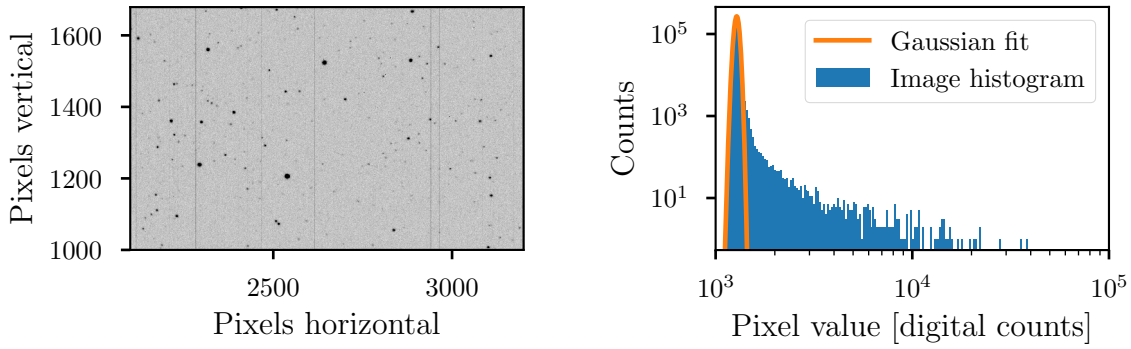

Figure 4.1: Left: Cut-out of a typical pointing image recorded during the test campaign at the MAGIC telescopes. Brightness values have been inverted and adjusted arbitrarily for better visibility. Right: Brightness histogram for the same image cut-out. A fitted Gaussian function that describes the background is also shown.

4.1 Functionality of libPointingMST

Overview

The algorithm of libPointingMST consists of three main parts. In the first part, the positions of star-spots in the image are determined, using the information of the brightness values of the pixels. The output of the spot extraction algorithm is a list of spots with measured positions and brightness values. This spot list is then passed to the field solving algorithm. This algorithm identifies spots in the list with stars whose positions are available through a pre-compiled index file. During this procedure, a coarse transformation between pixel and celestial coordinates is constructed. This transformation is then refined in the last part, the WCS fine fit. In this, all spots that can be identified with stars are used to obtain a transformation as precise as possible. In the following, analysis steps are discussed in more detail.

Spot extraction

The first step in calibrating a given SingleCCD pointing image is the extraction of star positions from spots of higher intensity than the surrounding pixels. In order to be able to detect these and to measure their intensity, the background level has to be estimated for every position in the image. Once the Cherenkov camera and other telescope structure is removed from the image, all background in the image is expected to be caused by the pedestal and thermal noise of the CCD chip and night sky background. The telescope structure is removed from the image via a mask image that is constructed beforehand. Pixel values of masked out areas are set to zero, which marks them as to be ignored in further analysis. Figure 4.1 (left) shows a cut-out of an exemplary pointing image and the corresponding brightness histogram. The majority of pixels in the image have brightness values at background levels. This is reflected

by the dominant peak at the left hand side of the histogram. Entries further right in the histogram correspond to the foreground objects in the image. To decide for each pixel whether it is part of background or foreground, its brightness value is compared to the local background level. A pixel, indexed with i, is considered as foreground if its brightness I_i fulfils

$$I_i > \mu_{b,i} + \sigma_b \cdot n_\sigma, \tag{4.1}$$

with $\mu_{b,i}$ the mean background value at the pixel position, σ_b the standard deviation of the background distribution, and n_σ a threshold level that can be adjusted to optimise the spot extraction. Otherwise, it is considered as background. For calculating $\mu_{b,i}$, the image is subdivided into smaller, rectangular parts using a regular grid. For each sub-image, the average background level is estimated via the mode of the brightness distribution. Next, an image of a size equal to the original image is constructed whose pixel values are set to the average background level in the rectangle of the grid in which they fall. This rather patchy image is then smoothed using a Gaussian filter, approximated by box blur filters, with a size corresponding to the width of the grid rectangles. The resulting image, whose pixel values correspond to $\mu_{b,i}$, is called the background image. The standard deviation of the background σ_b is calculated via a fit of a Gaussian function

$$f : I \mapsto a \cdot \exp\left(-\frac{1}{2} \cdot \frac{(I-b)^2}{\sigma_b^2}\right) \tag{4.2}$$

with free parameters a, b, and σ_b to the brightness histogram of the whole pointing image. After the background estimation, an algorithm is applied that searches for connected groups of foreground pixels in the image. The found groups are then converted to so called *image objects*. In the next step, the acquired objects are filtered by their size, which is defined as the number of foreground pixels in the object. Too small objects are sorted out mainly to exclude residual noise or hot pixels. Too large objects are removed in order to filter out parts of the structure of the telescope that have not been removed by the image mask or artificial light sources in the sky like planes or satellites. For each remaining image object, the integrated, background subtracted brightness

$$S = \sum_i S_i = \sum_i (I_i - \mu_{b,i}) \tag{4.3}$$

and the centre of gravity

$$\begin{pmatrix} x \\ y \end{pmatrix} = \frac{1}{S} \sum_i \begin{pmatrix} S_i \cdot x_i \\ S_i \cdot y_i \end{pmatrix} \tag{4.4}$$

are used to construct a *spot* object. Hereby x_i and y_i denote the horizontal and vertical pixel coordinate of pixel i respectively.

Index files

For the software to be able to identify detected spots in the image with actual stars, it is necessary to make a catalogue accessible that includes positions of known stars and

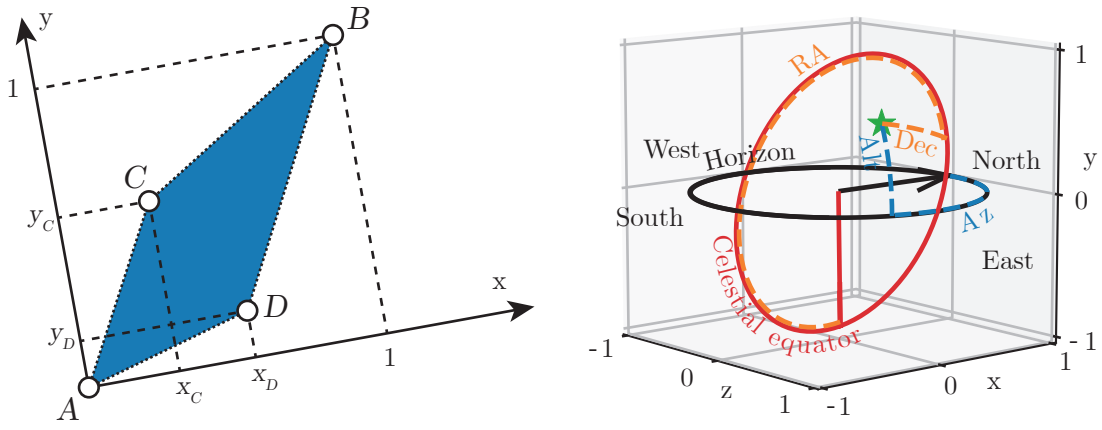

Figure 4.2: Left: Local coordinate system of a quad in which the geometric hash code $(x_C, y_C, x_D, y_D)^\top$ of a star constellation is calculated. **Right:** A position in the sky (green star) measured both in equatorial coordinates (right ascension and declination) and in horizontal coordinates (Azimuth and Altitude).

that makes an efficient way of searching for distinctive relative positions of neighbouring spots possible. As in astrometry.net, this is done via so called *index files*. These are constructed such that they include the equatorial position, visible magnitude, parallax, and proper motion of stars which are brighter than a defined threshold in visible magnitude $m_{\max}$. The index files also comprise a set of so called *quads*, which are groups of four stars with a typical size (angular distance between the two stars with the largest separation) r. For each quad, references for the underlying stars are stored together with a geometric hash code that makes an efficient search for quads with a similar shape possible. This code is, by construction, invariant under scaling, rotation, and translation. It is constructed as follows: The four stars are named A, B, C, and D. The positions of stars A and B define a local coordinate system in which their positions are $(x_A, y_A) = (0, 0)$ and $(x_B, y_B) = (1, 1)$. The positions of the other stars (x_C, y_C) and (x_D, y_D) are calculated relative to these in the planes that are defined by projecting stars A, B, and C and A, B, and D to the unit sphere. The local coordinate system is illustrated in Figure 4.2 (left). The stars A and B are chosen such that these two stars in the quad have the largest angular separation and that $x_C + x_D \leq 1$. Stars C and D are selected such that $x_C \leq x_D$. With this labelling of the stars, the geometric hash code that describes the shape of the quad is defined as the vector $(x_C, y_C, x_D, y_D)^\top$.
This geometric hashing system is well suited for comparing quads that are constructed from spots in an image with quads in an index, which are built with star positions from a reference catalogue, because small changes in the positions of the stars result in small changes in the hash code. Such small changes are introduced by projection effects caused by transforming from the spherical to the tangential plane coordinate system of the image and by uncertainties in the spot extraction and in the star catalogue.

The hash codes are organised in a multidimensional binary search tree, also called k-d tree [Bentley 1975]. In this data structure, the 4-dimensional code space is successively divided at the medians of the different dimensions into subsets until single codes, which represent the leaves of the tree, remain. With this, nearest neighbour searches can be carried out very efficiently. Such searches are needed in order to find quads in an index that are similar to a given quad in an image.
The stars in an index file are also sorted in a 3-dimensional tree with respect to their position on the unit sphere in Cartesian coordinates. This allows for an efficient retrieval of stars close to an already matched quad.
During the creation of an index file, it is taken care that the whole sky is isotropically populated by quads. This is achieved by using a HEALPix grid [Calabretta et al. 2007], which divides the celestial sphere into sectors of equal solid angles. An iterative algorithm tries to build a new quad for one sector after the other whose centre of gravity resides within the sector. When choosing stars for the creation of a new quad, brighter stars are preferred because they are more likely to be detected in an image. In order to counteract that only the brightest stars are used, the number of times a star is used for the generation of a quad is tracked, which enables the algorithm to also prefer more rarely used stars. This procedure of searching one new quad for each sector of the whole sphere is repeated for a specified number of times n_q. This value determines the density of quads in the final index.
The size of the quads is chosen such that the distance between stars A and B corresponds roughly to the pixel size of the HEALPix grid. Thus, the typical quad size of an index is given by the number of pixels per side (n_{side}) of this grid. The index files used by libPointingMST are saved in the Flexible Image Transport System (FITS) format [Wells et al. 1979]. Experience with the solution of real pointing images showed that indices with $n_q \in \{16, 32\}$ and $n_{\text{side}} \in \{32, 64\}$ provide good solving efficiencies. Therefore, four index files with all combinations of the above named n_q and n_{side} have been built which were used in all image analysis described in this thesis.

Solving the star field

When solving a set of spots in an image, i.e. identifying the spots with stars in an index, quads are built from adjacent spots. An algorithm successively selects sets of spots from which quads with a given size can be built. For each quad, a nearest neighbour search for geometrically similar quads in the index within a defined tolerance is performed. Each found correspondence represents a hypothesis that the spots in the image quad are caused by the stars in the sky quad. This hypothesis has to be tested because of possible false matches. This can only be accomplished by taking into account other stars that are close to the found quad and should be visible in the image if the match is correct. For this, a coordinate transformation between pixel and sky coordinates is set up. For this first transformation, a simple tangential (or gnomonic) projection is used. This means that points on the celestial sphere are projected to the tangent plane that touches the sphere at the tangent point $(x_t, y_t, z_t)^\top$ in Cartesian or $(\lambda_t, \beta_t)^\top$ in spherical coordinates. The used coordinate

system is sketched in Figure 4.2 (right). This tangent point defines the origin of an intermediate world coordinate system. In this 2-dimensional coordinate system, the coordinate u denotes the distance from the tangent point in horizontal direction, i.e. parallel to the celestial equator plane, while v denotes the vertical distance, orthogonal to u. An arbitrary point $(x, y, z)^\top$ can be transformed into the intermediate world coordinate system in two steps if it lies within the hemisphere that is confined by the plane which is parallel to the tangential plane and which goes through the centre of the unity sphere. The first step consists of the two rotations in xz- and xy-plane

$$\begin{pmatrix} x' \\ y' \\ z' \end{pmatrix} = R_z(-\beta_t) \cdot R_y(-\lambda_t) \cdot \begin{pmatrix} x \\ y \\ z \end{pmatrix}, \tag{4.5}$$

with

$$R_y(\lambda) = \begin{pmatrix} \cos(\lambda) & 0 & \sin(\lambda) \\ 0 & 1 & 0 \\ -\sin(\lambda) & 0 & \cos(\lambda) \end{pmatrix} \text{ and } R_z(\beta) = \begin{pmatrix} \cos(\beta) & -\sin(\beta) & 0 \\ \sin(\beta) & \cos(\beta) & 0 \\ 0 & 0 & 1 \end{pmatrix} \tag{4.6}$$

the rotation matrices in xz- and xy-plane respectively. These rotations would transform $(x_t, y_t, z_t)^\top$ to $(1, 0, 0)^\top$ and all other points to a coordinate system in which the tangent plane is orthogonal to the x-axis. In the second step, the rotated point is scaled by its x-coordinate, which effectively projects it to the tangent plane:

$$\begin{pmatrix} u \\ v \end{pmatrix} = \begin{pmatrix} z' \\ y' \end{pmatrix} \cdot \frac{1}{x'}. \tag{4.7}$$

The inverse transformation from intermediate world coordinates to celestial coordinates is

$$\begin{pmatrix} x \\ y \\ z \end{pmatrix} = R_y(\lambda_t) \cdot R_z(\beta_t) \cdot \begin{pmatrix} 1 \\ v \\ u \end{pmatrix} \cdot \frac{1}{\sqrt{1 + u^2 + v^2}}. \tag{4.8}$$

The axes of the intermediate world coordinates are aligned with right ascension and declination. As this does not hold for the coordinate system that is defined by the pixels of an image, a further transformation between pixel coordinates and intermediate world coordinates is needed. This transformation is defied by the position of the (transformed) tangent point in pixel coordinates $(x_c, y_c)^\top$ and a 2×2 matrix M_{cd} that accounts for any rotation, tilting, and scaling between the systems. An arbitrary point $(x, y)^\top$ in pixel coordinates is transformed as follows:

$$\begin{pmatrix} u \\ v \end{pmatrix} = M_{\mathrm{cd}} \cdot \left[\begin{pmatrix} x \\ y \end{pmatrix} - \begin{pmatrix} x_c \\ y_c \end{pmatrix} \right] = \begin{pmatrix} \mathrm{cd}_{11} & \mathrm{cd}_{12} \\ \mathrm{cd}_{21} & \mathrm{cd}_{22} \end{pmatrix} \cdot \begin{pmatrix} \tilde{x} \\ \tilde{y} \end{pmatrix}, \tag{4.9}$$

where the variables cd_{ij} are the entries of M_{cd} and $\tilde{x}$ and $\tilde{y}$ are the pixel coordinates relative to the tangent point. The inverse transformation is performed via the inverted matrix ${M_{\mathrm{cd}}}^{-1}$:

$$\begin{pmatrix} x \\ y \end{pmatrix} = \begin{pmatrix} x_c \\ y_c \end{pmatrix} + {M_{\mathrm{cd}}}^{-1} \cdot \begin{pmatrix} u \\ v \end{pmatrix} = \begin{pmatrix} x_c \\ y_c \end{pmatrix} + \frac{1}{\det(M_{\mathrm{cd}})} \cdot \begin{pmatrix} \mathrm{cd}_{22} & -\mathrm{cd}_{12} \\ -\mathrm{cd}_{21} & \mathrm{cd}_{11} \end{pmatrix} \cdot \begin{pmatrix} u \\ v \end{pmatrix}. \tag{4.10}$$

The initial coordinate transformation, that is set up with the stars of the found quad and the corresponding spots alone, is constructed assuming that the tangent point in the sky coincides with the centre of gravity of the stars and the projected tangent point in the image lies in the centre of gravity of the quad-spots. This means that the coordinates of the spots can easily be converted to relative pixel coordinates and the positions of the four stars can be transformed into the intermediate world coordinate system. The unknown entries of M_{cd} can be calculated by applying Equation 4.9 to each correspondence of a star and a spot. This yields an overdetermined system of inhomogeneous linear equations that can be expressed as:

$$\underbrace{\begin{pmatrix} u_A \\ v_A \\ u_B \\ v_B \\ u_C \\ v_C \\ u_D \\ v_D \end{pmatrix}}_{\boldsymbol{b}} = \underbrace{\begin{pmatrix} \tilde{x}_A & \tilde{y}_A & 0 & 0 \\ 0 & 0 & \tilde{x}_A & \tilde{y}_A \\ \tilde{x}_B & \tilde{y}_B & 0 & 0 \\ 0 & 0 & \tilde{x}_B & \tilde{y}_B \\ \tilde{x}_C & \tilde{y}_C & 0 & 0 \\ 0 & 0 & \tilde{x}_C & \tilde{y}_C \\ \tilde{x}_D & \tilde{y}_D & 0 & 0 \\ 0 & 0 & \tilde{x}_D & \tilde{y}_D \end{pmatrix}}_{S} \cdot \underbrace{\begin{pmatrix} \mathrm{cd}_{11} \\ \mathrm{cd}_{12} \\ \mathrm{cd}_{21} \\ \mathrm{cd}_{22} \end{pmatrix}}_{\mathbf{cd}}, \tag{4.11}$$

where indices A, B, C, and D correspond to the equally labelled stars and spots in the found quad. This system of equations is approximately solved by a **cd** that minimises

$$||S \cdot \mathbf{cd} - \boldsymbol{b}||. \tag{4.12}$$

This is achieved by performing a singular value decomposition of S. This yields a unitary 8×4 matrix U, a conjugate transpose of a unitary 4×4 matrix V^* and a diagonal 4×4 matrix Σ that fulfil $S = U\Sigma V^*$. The diagonal entries of Σ (σ_1, ..., σ_4) are called singular values of S. The pseudoinverse of S can now be calculated as [Horn et al. 1985]

$$S^+ = V\Sigma^+ U^*, \tag{4.13}$$

where

$$\Sigma^+ = \mathrm{diag}({\sigma_1}', ..., {\sigma_4}') \text{ with } {\sigma_i}' = \begin{cases} \frac{1}{\sigma_i} & \text{if } \sigma_i > 10^{-6} \\ 0 & \text{if } \sigma_i \leq 10^{-6} \end{cases}. \tag{4.14}$$

Setting the diagonal entries of Σ^+ to zero if the corresponding singular value is very small makes the method numerically stable. With S^+ **cd** can be calculated as

$$\mathbf{cd} = S^+ \cdot \boldsymbol{b}. \tag{4.15}$$

With that, the complete transformation between celestial and pixel coordinates is known and stars close to the found quad can be projected to the image.
With the information of where spots of stars are expected to appear in the image, a Bayesian decision test is applied that evaluates how well the hypothesised alignment defined by the found quad can predict other matches in the image. This procedure is covered in more detail in Lang et al. [2010]. The basic idea is to find for each spot in the image (in the order of their brightness) the closest expected spot. Their distance is then transformed into log odds, taking into account the spot's distance to the found quad and a jitter value that is derived from the image's resolution. These log odds are then compared to that of a random coincidence with a spot in a set of uniformly distributed spots. If the former log odds are higher, the correspondence is considered a match and is saved and the log odds are added to the total log odds of the hypothesis. Otherwise, the correspondence is considered no match and the log odds of random coincidence are added. After all spots have been taken into account, the resulting total log odds are compared to a predefined threshold. If they are lower, the hypothesised alignment is rejected and the procedure of building quads from adjacent spots in the image and searching for similar ones in the index continues with the next set of spots. If the log odds are higher than the threshold, the hypothesis is accepted and all found correspondences and the used coordinate transformation are stored in a *match* object which is used in further analysis steps. If all possible quads in a given image have been tried unsuccessfully, the whole matching procedure is tried with another index file that contains different quads. Only when all available index files have failed to deliver a match, the image is considered unmatchable.

Re-matching

After an image has been solved and a first coordinate transformation between pixel and sky coordinates has been set up, an advanced algorithm is applied that revisits all spots in the image and matches them to stars which are expected to be visible in the image. The difference between this algorithm and the matching procedure during the hypothesis test of a quad match is that it matches stars via the geometric arrangement of sets of stars whereas the first matching only searches for nearest neighbours. The first approach of nearest neighbour matching is quite fast but also has some limitations, especially when it handles spots that are located far away from the initially matched quad in the image. The further away from the matched quad the initial transformation is evaluated, the more errors become dominant which are introduced by the simplifying assumptions regarding the location of the tangent point in the image and on the sky. The situation after the initial match and the re-matching is illustrated in Figure 4.3 for an exemplary image. Most of the spots that could be matched during hypothesis testing are located close to the matched quad in the right part of the image. In the detail view, an obviously falsely matched star can be seen. This match is replaced with a correct one by the re-matching algorithm. This is possible because the latter algorithm utilises the fact that spots and stars close to each other are expected to be offset from another by nearly the same value and in

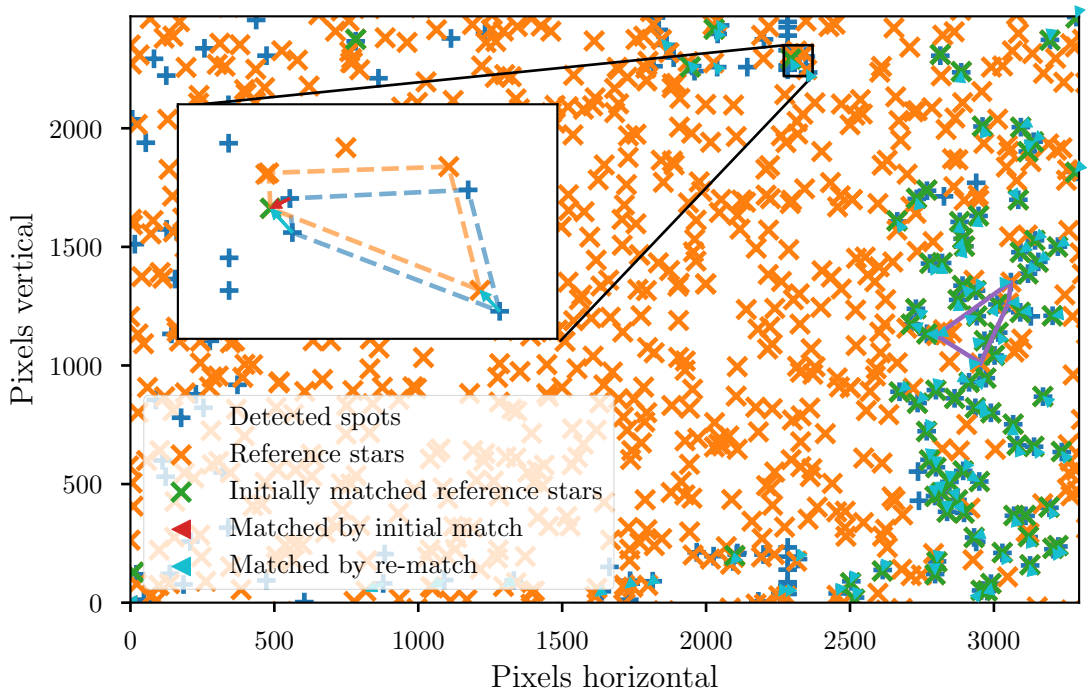

Figure 4.3: Illustration of the spot-star matching procedure during the analysis of a pointing image recorded during the test campaign at the MAGIC telescopes. The purple quadrangle corresponds to the initially matched quad. The detail view in the left shows an initially falsely matched star (red arrow). The re-matching that compares constellations of spots and stars (blue and orange dashed) removes these and adds correct identifications (cyan arrows).

nearly the same direction. This is achieved by selecting sets of four spots that form quads with a predefined size like the one indicated in the figure. Then the algorithm builds all possible quads from reference stars that occur in the area around the selected spots and searches for one similar to the spot-quad. If a quad is found, like indicated in the figure, the stars and spots can be identified. As it is considered to be more important that as few false identifications are made than to match as many stars as possible for a precise solution of an image, some means are applied that make the algorithm more conservative: For every spot, the number of different quads that support its identification with a certain reference star is tracked. Once this number equals 3 or more, the identification is considered as robust and the spot is not tested any more. On the other hand, every time no match in the references can be found for a quad built with a certain spot, this spot's fail count is increased by one. If this fail count reaches a value of 3, the spot is excluded from further matching attempts and is considered unidentifiable. A given spot-quad is also not used for the re-matching process if the most similar star-quad differs too little from the second most similar star-quad.

WCS fine fit

When the re-matching is completed and more supporting points than the four stars of the initial quad are available, an advanced fitting routine is applied. This fit minimises the squared distance between spot and reference star summed up over all identified pairs by varying the parameters of the transformation between pixel- and sky-coordinates:

$$\chi^2 = \sum_i (\boldsymbol{x}_{p,i} - \boldsymbol{x}_{s,i})^2. \tag{4.16}$$

Here $\boldsymbol{x}_{p,i}$ denotes the pixel position of spot i in the image and $\boldsymbol{x}_{s,i}$ the pixel position of the according reference star. For this fit, a different coordinate transformation is used, that transforms between the celestial system and the system of a virtual camera which is located at a specific location on Earth on an azimuthal mount and records images of the sky at a specified time. The transformation that is used is implemented in the H.E.S.S. software. Using this software has the advantage that also effects by refractions in the Earth's atmosphere and parallax and proper motion effects of stars are modelled. The refraction model which is used integrates refractions over the complete line of sight through different air layers of varying temperature, pressure, and density and is described in Seidelmann et al. [2010]. One downside of the H.E.S.S. coordinate transformations is their usage of small angle approximation.
For the minimisation, an algorithm implemented in *NLopt* [Johnson 2019] is used. This open-source software package contains many different optimisation algorithms and provides a convenient way to test different routines. Best results were achieved with a global optimiser that uses a controlled random search algorithm with local mutation as defined by Kaelo et al. [2006]. This minimiser searches for global minima in a defined parameter space by evaluating the function at points chosen with a certain degree of randomness. This makes the WCS fitting non-deterministic, meaning that each time it is performed, the result is slightly different.
Because of the fitting being non-deterministic, it is beneficial to apply the optimiser multiple times. This is done for 8 times. After each fit, each of which is terminated as soon as the improvement between two iterations within the algorithm falls below a given threshold, it is checked whether the achieved value of the optimised function divided by the number of used spot-star matches is smaller than after a previous fit. If this is the case, the fitted WCS is stored as the new best solution. If the number of the current fit iteration is even, an additional re-matching is performed with the goal of possible further matched pairs which are possible because of the improved precision. Independent of the fact whether a smaller value of the minimised function could be reached, if the number of the current fit is odd, a further routine calculates the root mean square (RMS) of the distances between spots and reference stars. All pairs whose distance is larger than this RMS are removed from the fit. This is done in order to remove outliers that can contain false matches. At the end of each fit iteration, it is checked whether the number of matched pairs is at least half the number of pairs in the initial match. If not, the initial match is used again for the next iteration. Between the fit iterations, the optimised parameters of the WCS are always passed to the next iteration. The whole fitting process is terminated when the

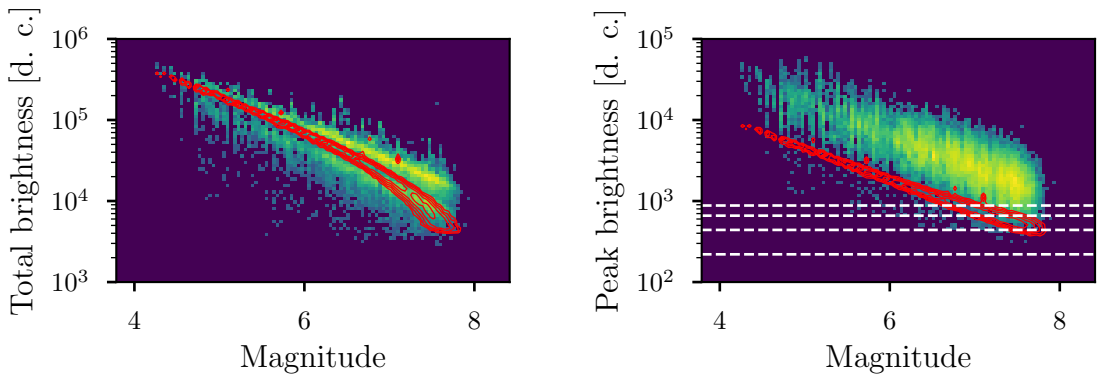

Figure 4.4: Brightness values for spots of stars with different magnitudes. The color coded histograms shows values from real images, while the red contour lines indicate spots in simulated images. **Left:** Summed up brightness of all pixels in a spot. **Right:** Largest brightness value in a spot. The dashed lines indicate the levels of the typical standard deviation of the background from top to bottom $4\sigma_b$, $3\sigma_b$, $2\sigma_b$, and $1\sigma_b$.

maximum number of iterations is reached or if the mean residual

$$\Sigma = \sqrt{\chi^2}/n \tag{4.17}$$

with n the number of matched pairs falls below a defined threshold.

4.2 Verification of libPointingMST with simulated data

The simulation software libCCDCamera

The software library *libCCDCamera*, which has been introduced by Tiziani [2015], was used in this thesis to simulate star fields and images which are the basis for verifying the performance of libPointingMST. It uses the same H.E.S.S. coordinate systems as the fitting routine of libPointingMST. The simulation software has been developed further in the scope of this thesis together with several students in their theses. In Egelkraut [2019] it was shown that the simulation reproduces the total brightness of real stars to a precision of 0.3%. The positional deviation between simulated spots and extracted spots in real images has been measured to be smaller than one pixel.
One limitation of the simulation is the approximation of the shape of star spots by a 2-dimensional Gaussian function. In real images, the intensity is much more concentrated in the central pixels of a spot. This results in the fact that the peak brightness (the largest pixel value in a spot) of a real star spot is significantly higher than that of a simulated spot, even if their total intensities are equal. This behaviour is illustrated in Figure 4.4. Consequently, simulated spots of stars with magnitudes larger than ~ 7 will not be detected by the spot extraction if a threshold level $n_b \geq 4$ is used, while the spot of the same star can be detected in a real image.

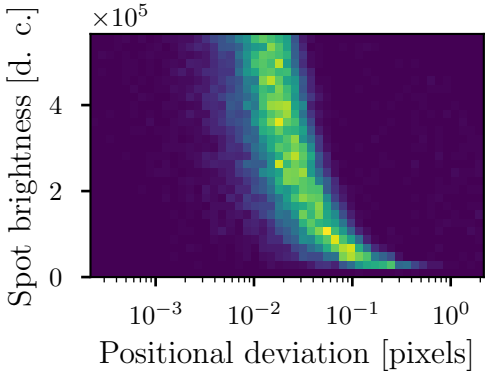

Figure 4.5: Dependence of the deviation between true and extracted spot positions on the brightness of the spots for simplified images. The number of entries in the 2-dimensional histogram is colour coded.

Spot extraction

For a first test of the precision of the spot extraction, a set of simplified pointing images with the same pixel size as real images from the pointing camera were generated. These images only contain a random background component that is similar to real images and randomly distributed spots with a 2-dimensional Gaussian shape with varying brightnesses. For the width of the Gaussian function, a value of 3 pixels is used. While distributing the spots over the images, it was made sure that they do not overlap. In particular, this means that the spots were forced to have a minimum distance of 30 pixels to each other. The resulting images were passed to the spot extractor of libPointingMST and the retrieved positions were compared to the values used in the generation of the images. The position of the spots could be reconstructed with a mean deviation of 0.04 pixels. In Figure 4.5, the correlation between spot brightness and precision of the extraction is shown. For brighter spots, the precision is higher than for fainter spots. The mean extraction precision of all spots with a brightness $> 4 \cdot 10^5$ is 0.014 pixels, while all spots fainter than a brightness value of $5 \cdot 10^4$ can be extracted with a precision of 0.17 pixels. This trend is expected because brighter spots yield better statistics due to their larger signal to noise ratio and their extraction is less susceptible to effects by clipping signal at the edges of the spots.

Exact star positions

In order to test the matching and fitting algorithms of libPointingMST, exact spot positions calculated with libCCDCamera were fed into them. This excludes any possible errors in the spot extraction. Stars with a maximum magnitude of 9 were used for this study. For this, a set of 1000 uniformly distributed pointing directions in the azimuth range of 0° - 360° and in the altitude range of 20° - 90° was randomly generated. For easier comparison with real images taken at one of the MAGIC telescopes, its location (28°45′42.9″ N 17°53′24.3″ W at 2200 m a.s.l.) was used for the

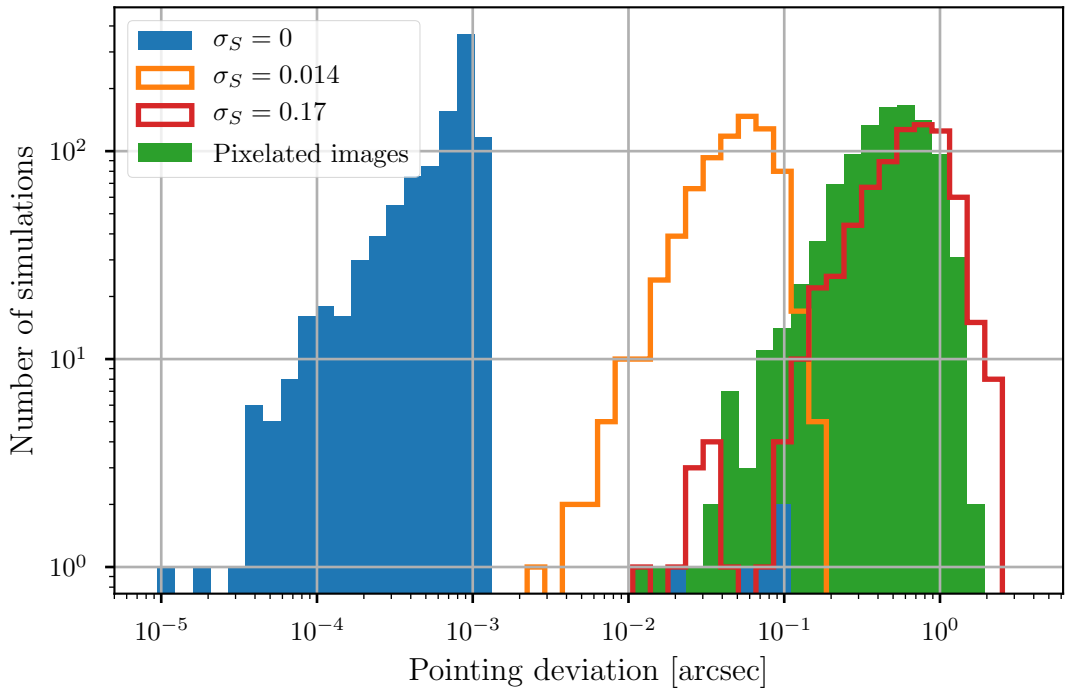

Figure 4.6: Distributions of pointing deviations for reconstructions of sets of 1000 simulated star fields with different random displacement widths σ_S and for reconstructions of a set of 1000 simulated, pixelated images.

position on earth where the virtual camera was placed. All star fields were simulated at the arbitrarily chosen observation time of 01.01.2000 12:00:00 UTC. The size of the CCD-chip was set to (3296×2472) like in the Apogee camera described in Chapter 3.4 and an ideally rectilinear lens with no distortions and a focal length of 51 mm was simulated. This focal length was chosen because experience with real images showed that using this value results in images that resemble better to images recorded with the real lens with a nominal focal length of 50 mm.
The spot positions and simulated brightnesses of these 1000 star fields were directly passed to the field solving and WCS fitting algorithms of libPointingMST. The angular distance between the simulated and the reconstructed pointing direction was then calculated for each field. This distance will be called *pointing deviation* in the following.
As the same code is used for the coordinate transformations for simulation and for reconstruction, it should in principle be possible to retrieve the coordinate transformations for a field of exactly known spot positions with a precision that is limited only by numeric uncertainties. For all of the 1000 star fields, a pointing solution could be found. Figure 4.6 shows the distribution of the obtained pointing deviations. The mean of this distribution is $0.001''$ while the maximum deviation is $0.1''$. An overview of all obtained pointing deviation values can be seen in Table 4.1. Noticeably, five star fields were solved with a pointing deviation larger by one order of magnitude

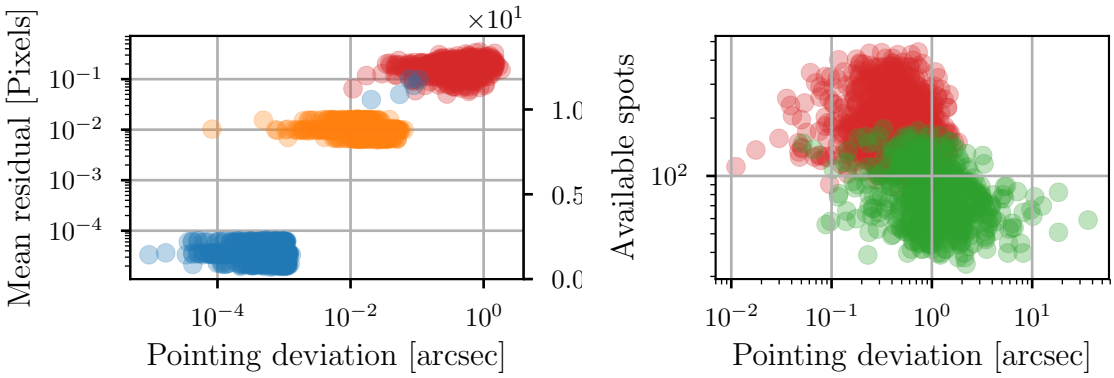

Figure 4.7: Left: Correlation between pointing deviation and mean residual for different simulation studies. Blue: exact spot positions; orange: spot positions with $\sigma_S = 0.014$; red: pixelated images. **Right:** Correlation between pointing deviation and number of extracted spots N_S for simulated images with FoV mask (green) and without mask (red).

compared to the others. In these cases, the WCS fit is assumed to have reached only a local minimum, which also results in mean residuals Σ larger by about three orders of magnitude as shown in Figure 4.7 (left).
To get an estimate on how the precision of the algorithm is influenced by uncertainties in the spot extraction, the above described study was repeated with spot positions with an artificial random displacement. This displacement was generated according to a Gaussian distribution with two different widths σ_S that correspond to the minimum and maximum extraction precisions acquired by the test described above. Additionally, the maximum magnitude of stars that are used for generating spot positions was set to a value of 7 in order to emulate the effect of undetectable stars in simulations with higher magnitudes. The resulting distributions of the pointing deviations are also shown in Figure 4.6. The mean deviation of the spots with the uncertainty of brighter stars is 0.054″ while the star fields of the spots with the larger uncertainty of fainter spots are reconstructed with a mean precision of 0.70″. The maximum observed deviations are 0.16″ and 2.3″, respectively.

Pixelated images

For the next tests, pixelated images were simulated. The parameters of the simulation algorithm of libCCDCamera were chosen such that the resulting images resemble real pointing images as closely as possible: Besides all settings as described in 4.2, which still apply, an aperture of $f/5.6$, an exposure time of 10 s, and a photon detection efficiency of 8.75 % [Egelkraut 2019] were used for generating the images. Of the simulated set of 1000 images, 999 could be solved successfully. For one image, the reconstruction failed. The reason for this failure, that occurs in rare cases, is not fully understood. It might be caused by an unfortunate set of extracted spots which can not be combined to quads that have correspondences in the used index files. The resulting distribution of pointing deviations is also plotted in Figure 4.6 for an easy

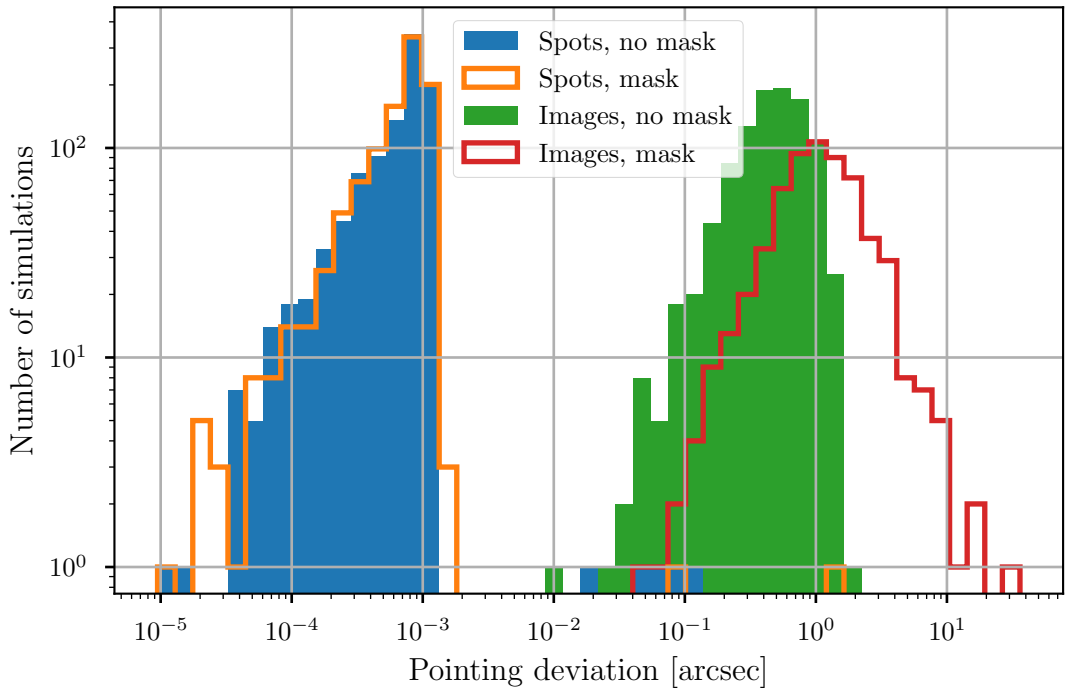

Figure 4.8: Comparison of distributions of pointing deviations for reconstructions of sets of pixelated images and exact star fields, with and without applied image masks.

comparison with the above described simulations of spot lists. The mean deviation of 0.53″ and the maximum deviation of 1.8″ fall between the values derived for the two simulation series of randomly displaced spots. The fact that pixelated images can be solved a little more precisely than star fields with an applied random displacement equal to the uncertainty of extracted spot positions of fainter stars suggests that the main precision-limiting factor is the named extraction uncertainties.

Field of view mask

As explained in 3.3, in a real application of the SingleCCD pointing, stars are only visible in about 38 % of the area of a given image. In order to check the performance of libPointingMST with this reduced field of view, the mask shown in Figure 3.3 was applied both on simulated spot lists and on simulated images. The resulting pointing deviation distributions are plotted in Figure 4.8. For 1000 simulated lists of exactly known spot positions, applying the field of view mask reduced the mean precision to 0.0024″ with a maximum deviation of 1.58″. All of these spot lists could be solved. The mean pointing deviation that was obtained with masked, pixelated images is 1.52″ and the maximum observed deviation is 35″. Of the simulated pixelated images, only 60 % could be solved. This poor performance is likely caused by the small number of stars that are extracted from the images. Due to the fact that the profile of the star spots is not modelled perfectly in the simulation as discussed in 4.2, a large part

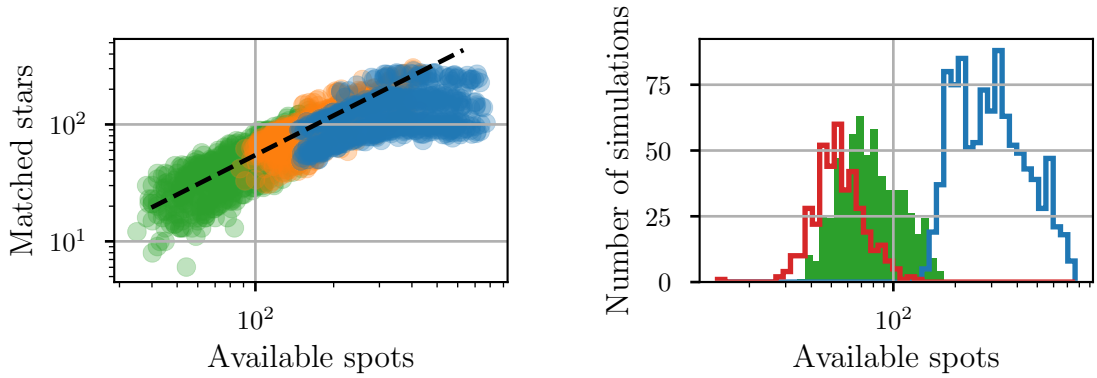

Figure 4.9: Left: Correlation between number of available spots for the reconstruction and number of matched stars for different simulation studies. Blue: sets of exact spot positions with applied FoV mask; orange: pixelated images without mask; green: pixelated images with applied FoV mask. A power law with index 1.1 is plotted with a black dashed line to guide the eye. **Right:** Distributions of spots available for the reconstruction algorithm of libPointingMST. Green: Extracted spots from simulated, pixelated images with applied FoV mask that could be solved; red: extracted spots of the same set that could not be solved; blue: sets of exact spot positions with applied FoV mask.

of spots from fainter stars is not detected. This leads to fewer stars available for the reconstruction. It can be seen in Figure 4.9 (left) that the number of available spots N_S is lower for the set of simulated images than compared to simulated star fields and images with no applied mask. A drop in this number results in a drop of the number of matched stars in the images N_M, which was found to be roughly proportional to ${N_S}^{1.1}$. This power law applies independent of the type of simulation (with or without mask, images or star fields) up to a break at $N_S \sim 300$ where N_M stays constant with further increasing N_S. Figure 4.9 (right) shows the distribution of N_S both in the solvable and in the not solvable subset of the simulated, masked images and additionally the distribution of the number of available spots in the masked star field simulations. It can be seen that unsolvable images start to occur at values of $N_S < 100$. As indicated by Figure 4.7 (right), the precision of the reconstruction also depends on the number of available spots as all masked images that were reconstructed with a precision of less than $4''$ also have $N_S < 100$.

4.3 Analysis of the test campaign at MAGIC

In this section, the performance studies of the libPointingMST algorithms with real images recorded during the measurement campaign at the MAGIC telescope are described. During this campaign, a total of 39891 images have been recorded with the SingleCCD prototype between 4th July 2018 and 6th August 2019. The used exposure time has been changed multiple times during that time while the aperture of $f/5.6$ stayed constant over the whole period. Due to technical reasons, the prototype camera plus a controlling computer could only be operated as a stand-alone system

Table 4.1: Overview over pointing deviations obtained via simulations.

Simulation	Mean pointing deviation	Max. pointing deviation
Exact spots	0.001″	0.1″
Spots with $\sigma_S = 0.014$	0.054″	0.16″
Spots with $\sigma_S = 0.17$	0.70″	2.26″
Pixelated images	0.53″	1.8″
Exact spots with mask	0.0024″	1.58″
Pixelated images with mask	1.52″	35″

without any exchange of information with the data acquisition software of MAGIC. Because of this, the camera was programmed to record images with a specified frequency in a time window that roughly covers the dark time at the site of the MAGIC telescope every night. Within these boundaries, images were recoded regardless of the weather and whether the telescope was carrying out observations or not. When the telescope is not in operation during daytime or because of unfavourable observation conditions, it resides in its parking position, aligned in northern direction and towards the ground.
In contrast to simulated images, the true pointing direction is not known for images taken at the MAGIC telescope. The CCD camera has been mounted such that its optical axis coincides only roughly with the optical axis of the telescope such that the pointing direction of the telescope is somewhere within the field of view of the camera. For the studies in this thesis, the requested pointing direction (i.e. the one that is specified by the observation plan) of the telescope was available in equatorial and azimuthal coordinates and the present or actual pointing direction was available in azimuthal coordinates. All coordinates were available with a time resolution of 1 s. In addition to that, the status of the drive system was also available, i.e. whether the telescope was tracking a source, slewing to a new position, in its parking position, etc. This information was used to obtain the pointing data of the telescope for the point in time in the middle of the exposure time of each recorded pointing image. A problem of this data is that the temporal offset between the clock of the computer that stored the images and that of the drive system that stored the pointing data is unknown. This offset is expected to be small ($\ll 1$ min) but it could not be determined exactly due to technical reasons.

Data selection

As the data acquisition of the SingleCCD prototype camera was not connected to the data acquisition of MAGIC, a lot of images have to be removed from the total data set to obtain sets of images that were taken under conditions similar to an observation of a future MST telescope and which can be used for the performance studies. Only images were used for which the stored status is "tracking source" throughout

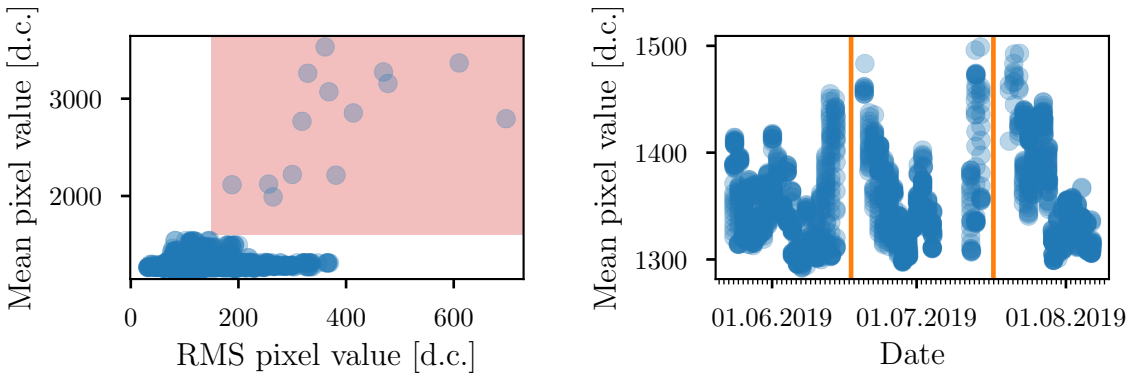

Figure 4.10: Left: Mean pixel values as a function of RMS values for images during the construction of Set10. The red overlay shows the parameter space of images that was excluded from the set. **Right:** Trend of the mean pixel value over time for images in SetT. The moments of full moon phase are indicated by orange lines.

the whole exposure time, which were taken at a pointing altitude $> 20^\circ$ and for which tracking data with a timing with a precision of $\leq 1\,\mathrm{s}$ is available.
To check the influence of different operation parameters of the camera and the temporal stability of the system, several subsets were created for further performance studies of libPointingMST.
For the first dataset, which will be called *Set10* in the following, images recorded with an exposure time of 10 s and a CCD chip that is cooled below $-20\,^\circ\mathrm{C}$ were selected. Images that were not taken during dark time are also removed from the subset. The 4076 images of the resulting subset were investigated in more detail. Figure 4.10 (left) shows their mean pixel value as a function of the RMS pixel value. Two disjunct populations can be seen in the plot. Manual checks of random samples of the upper right population, which is also marked in the plot, showed that these images have been taken when the telescope was in its parking position and aligned towards the ground. To sort out these images that have not been recoded under observation conditions, a further cut was applied that removes images that have both a mean pixel value of larger than 1600 and an RMS pixel value of larger than 150. The final dataset Set10 contains 4062 images that have been recoded in the nights between 6th and 25th July 2018.
A second dataset *Set20* with images with 20 s exposure time was constructed analogously. With the exception that for this dataset, no direct cuts on pixel information were applied but a temporal cut that selects images recorded between 16th and 21st August 2018 as other images with that exposure time have been taken during bad observational conditions and most of them when the telescope was in its parking position. In total, this subset consists of 909 images.
The third dataset *SetT* is constructed to evaluate the analysis of images recoded with inactive CCD chip cooling. The set contains images taken between 24th May 2019 and 6th August 2019 because during that time, the chip cooling was switched off. All images were recorded with an exposure time of 10 s. Furthermore the dataset is

Table 4.2: Overview over used datasets from the MAGIC campaign.

Dataset	Images	Time span [d]
Set10	4062	19
Set20	909	5
SetT	2220	74

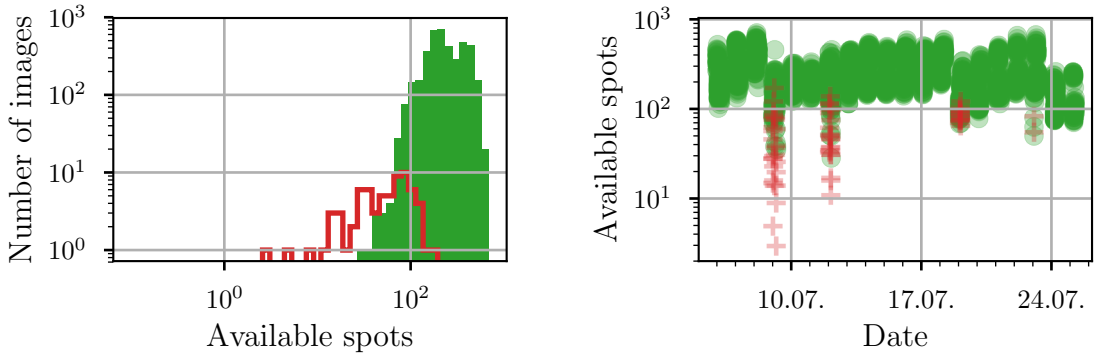

Figure 4.11: Left: Distributions of spots available for the reconstruction algorithm of libPointingMST after spot extraction and masking of the images in Set10. Green: solvable images; red: not solvable images; **Right:** Number of available spots for the reconstruction of images in Set10 as a function of the date when the images where taken. Solvable images are indicated with green dots while red crosses represent unsolvable images.

reduced to only contain images with a mean pixel value between 1290 and 1500 and with an RMS pixel value of less than 1000. These cuts have been found by examining random samples with the aim of again sorting out images taken in parking position when the telescope was not in operation due to moonlight or bad weather. SetT consist of 2220 images in total. Table 4.2 gives an overview over the three datasets.

Efficiency

The images of the three datasets were passed to libPointingMST, similar to the above described simulated images. The only difference to these previous studies is that a field of view mask was applied which removes both the structure of the MAGIC telescope visible in the images and the parts that would be obstructed by the MST structure if the camera was mounted to one of these future telescopes. Of the images in the three datasets Set10, Set20, and SetT, 97 %, 100 %, and 100 % respectively, could be reconstructed. Figure 4.11 (left) shows the distribution of the number of extracted spots, taking Set10 as an example. It can be seen that the field solving reconstruction algorithm tends to fail if the number of available spots is below ~ 100, similar to the studies with simulated images. Random samples of the unsolvable images revealed that they often exhibit areas of sizes in the order of 1/8 of the total

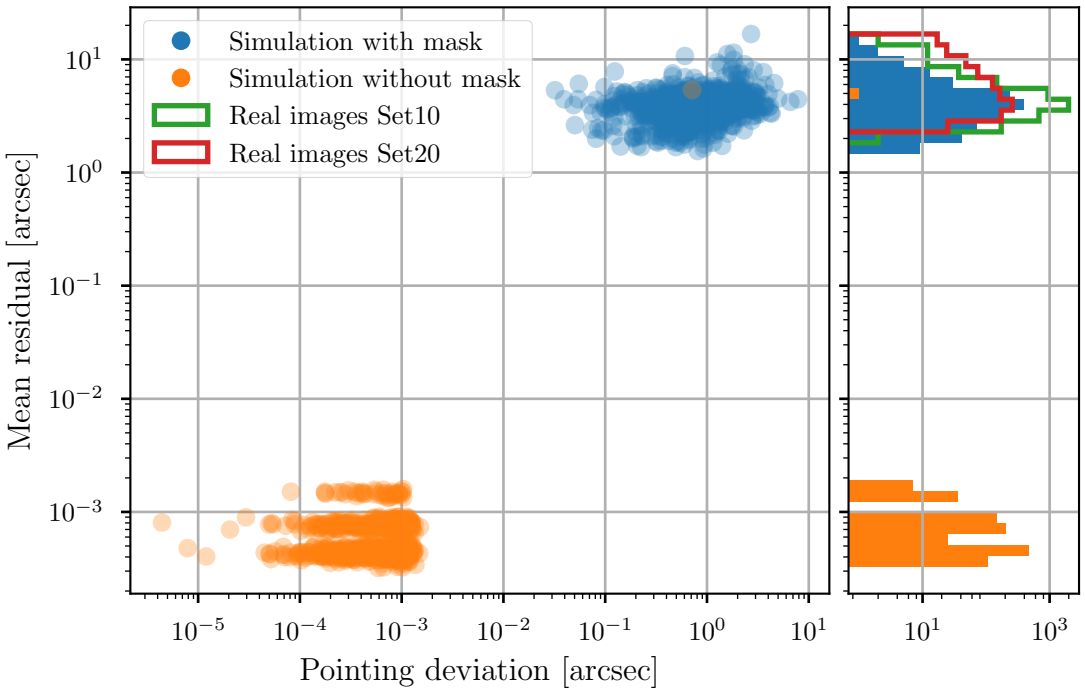

Figure 4.12: Mean residual as a function of pointing deviation for simulated images with and without mask. To the projected histograms to the right, the according distributions which are obtained for the datasets from the MAGIC campaign are added.

image size where no stars are visible or where the spots are much fainter. These areas are always close to the edges where they are not cut away by the field of view mask. So, valuable information in the form of an isotropic star coverage of the available field of view is not available to the algorithm. These areas are most likely caused by clouds because they were observed to move in the timespan of 2 min both relative to stars and relative to the image boundaries. The latter excludes an explanation by condensation on the window of the camera housing or in the optics of the camera. The hypothesis of the failed reconstructions being caused by unfavourable observation conditions is supported by the fact that the unsolvable images of Set10 have all been recorded on four distinct days. This can be seen in the right hand plot of Figure 4.11. It was also observed that the solvability of the images does not depend on the observation position.

Precision

As the exact true pointing direction of the recorded images is unknown, the precision of the astrometric solutions obtained with libPointingMST can only be studied indirectly.

Precision related observables

One way is the study of observables which are available for both real images and simulated images and which are related to the precision of the reconstructions. One parameter that shows some correlation to the pointing deviation of simulated images is the mean residual Σ. This correlation is visualised in Figure 4.12. The tendency that solutions with smaller Σ are more precise than solutions with larger Σ is visible in the difference between the solutions of simulations with and without a field of view mask. The right panel of the plot shows the distributions of the data points projected to the mean residual axis. Here, one can compare the results from the simulations with those from the MAGIC data sets. The distributions of Σ in the analyses of real images appear quite similar to those of the simulation with field of view mask. This suggests that the mean pointing deviation of the solutions of the real images is somewhere close to that of the simulated images with mask. Of course this estimation depends very much on the assumption that simulated and real images are similar enough and therefore the same errors occur during their analyses. That this is not the case can be seen by comparing the mean number of detected spots N_S. For the simulations with mask, an average number of 82 spots was extracted from an image, while in the images of Set10 a mean N_S of 259 was obtained.

Pointing model

Another possibility to obtain an estimate of the precision of the pointing reconstruction of real images is the construction of a pointing model. Such a model f predicts the reconstructed pointing direction of an image by using the pointing information provided by the drive data as input:

$$f : (\phi, \vartheta)^\top \rightarrow (\tilde{\phi}, \tilde{\vartheta})^\top, \tag{4.18}$$

were ϕ and ϑ denote the nominal azimuth and altitude that is provided by the drive system of the telescope and $\tilde{\phi}$ and $\tilde{\vartheta}$ denote the modelled azimuth and altitude that are expected to be the reconstructed pointing direction of an image which has been recorded at that same time. Once a model that includes all systematics has been constructed, the residual deviation between a reconstructed pointing direction $(\phi', \vartheta')^\top$ and the modelled one can be calculated. This residual, which can not be modelled because it originates from random fluctuations in the pointing reconstruction, can be used for an estimation of the precision of the image analysis.
The first and simplest pointing model that was constructed for this study models only a constant angular offset $(\Delta\phi, \Delta\vartheta)^\top$ between the optical axes of telescope and pointing camera. The model function is defined by two rotations:

$$f(\phi, \vartheta)_{\Delta\phi, \Delta\vartheta} = R_y(-\phi) \cdot R_z(\vartheta) \cdot \begin{pmatrix} \Delta x \\ \Delta y \\ \Delta z \end{pmatrix} \tag{4.19}$$

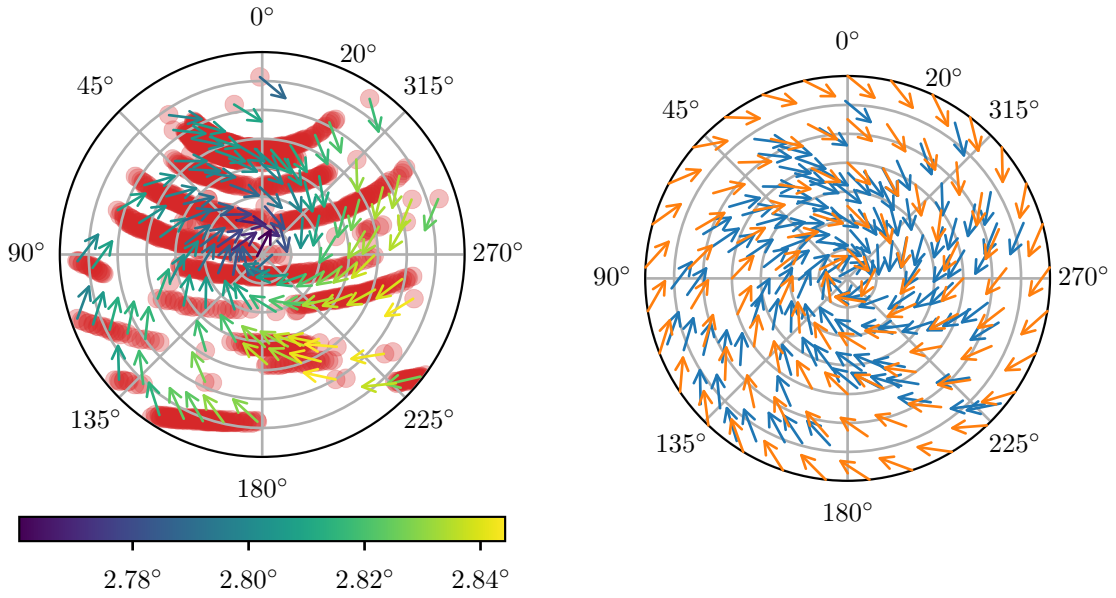

Figure 4.13: Left: Nominal pointing directions of SetT (red points) in azimuth and altitude. The altitude ranges from 20° (outer circle) to 90° (centre). The data points selected for pointing model generation are indicated with arrows whose tips point towards the reconstructed pointing direction of the CCD images. The arrow lengths are scaled by a factor of 4 for better visibility. The color code denotes the absolute angular differences between nominal and reconstructed pointing direction. **Right:** Comparison of modelled deviations (orange) to measured deviations (blue) of SetT with fitted mechanical model with constant camera offset. Arrow scale: 4.

where $(\Delta x, \Delta y, \Delta z)^\intercal$ corresponds to the vector $(\Delta\phi, \Delta\vartheta)^\intercal$ transformed to Cartesian coordinates:

$$\begin{pmatrix} \Delta x \\ \Delta y \\ \Delta z \end{pmatrix} = \begin{pmatrix} \cos(\Delta\phi) \cdot \cos(\Delta\vartheta) \\ \sin(\Delta\vartheta) \\ \sin(\Delta\phi) \cdot \cos(\Delta\vartheta) \end{pmatrix}. \tag{4.20}$$

To obtain a model for a given set of $(\phi_i, \vartheta_i)^\intercal$ and corresponding $(\phi'_i, \vartheta'_i)^\intercal$, the values for $\Delta\phi$ and $\Delta\vartheta$ that minimise the summed squared angular distance between all $(\tilde{\phi}_i, \tilde{\vartheta}_i)^\intercal$ and $(\phi'_i, \vartheta'_i)^\intercal$ have to be found.
In order to not bias the model towards denser sampled regions, it is favourable for the construction of a pointing model to use a dataset that includes coordinates isotropically distributed over the whole sky hemisphere. As the datasets available for this study have been taken during observations of gamma ray sources, they do in general not fulfil this requirement. To compensate this, a selection algorithm was applied to the datasets that selects only members with a nominal pointing direction that has a minimum angular distance d to all other members. The order in which members are chosen is determined via a random number generator. The seed of this random number generator can be chosen arbitrarily so that different subsets that all fulfil the distance criteria can be obtained.
Figure 4.13 (left) shows a specific selection of nominal pointing directions from SetT

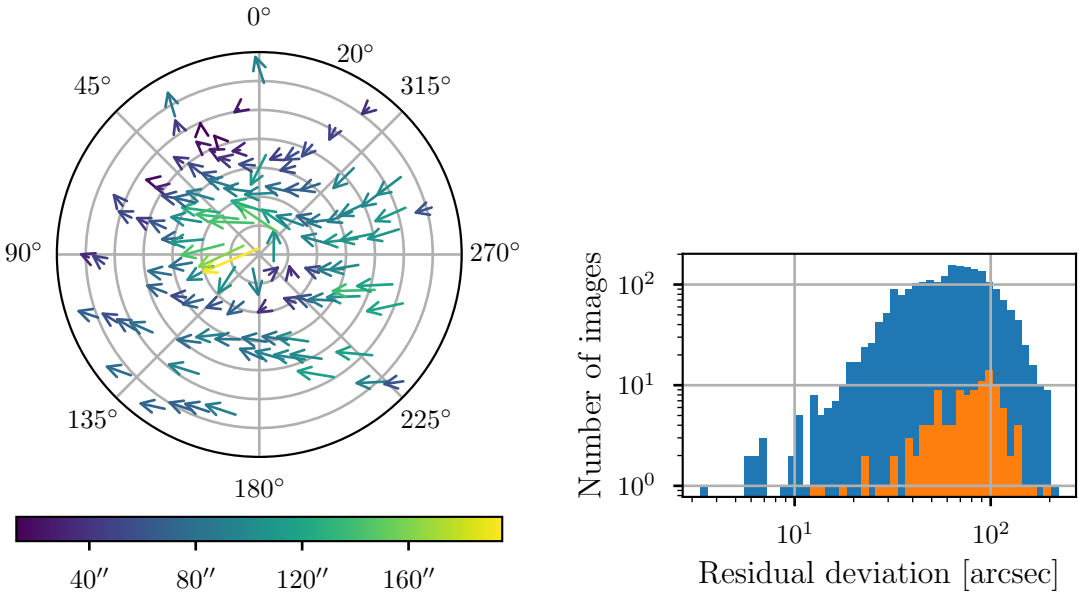

Figure 4.14: Left: Residual deviations between pointing directions modelled with a constant camera offset and reconstructed from camera images for a subset of SetT. Arrows are scaled by a factor of 400 for better visibility. The color code represents the absolute angular deviation. **Right:** Distribution of absolute angular residuals of the same model evaluated for the data points in the selection (orange) and for all data in SetT (blue).

with a minimum distance of $d = 5°$ and their deviation from reconstructed pointing directions. The selection in this case comprises 115 data points. A pointing model with a constant camera offset in azimuth and altitude was fit to this data. The best fit parameters obtained for this particular set are $(\Delta\phi, \Delta\vartheta) = (-1°58'7.0'', 2°0'30.7'')$. In the right hand panel of the figure, the results of the obtained model evaluated at fixed grid points are shown together with the data used for the fit. To first order, the data seems to be described well by the model. The residuals are visualised in the left panel of Figure 4.14. A mean residual deviation of 79.8″ was obtained for the selected set. The residual deviations for the whole dataset were also derived by applying the obtained model to all data points of SetT. The resulting distribution with a mean of 67.7″ is also shown in the right panel of Figure 4.14.
To test the dependence of the model residuals on the choice of data points for performing the fit, 100 different realisations of a subset were constructed by varying the seed for the selection algorithm. Of course the different realisations are not completely independent due to regions of the sky with low sampling density. In these regions, data points have a higher probability of being selected than in more densely sampled regions. In this study, the mean best fit parameters are $\overline{\Delta\phi} = -1°58'5.5''$ and $\overline{\Delta\vartheta} = 2°0'28.8''$ with standard deviations of 1.3″ and 1.8″, respectively. The mean values of the obtained residual deviations scatter around 79.4″ with a standard deviation of 1.0″. By applying the fit models to all data of SetT, it was discovered that a smaller mean residual of, in average, 67.7″ with a standard deviation of 0.6″ is reached. These smaller residuals of the whole datasets are likely explained by the larger relative

weight of measurements in less densely sampled regions of the sky hemisphere when calculating the residuals of the subsets. Measurements in these less densely sampled regions have few close neighbours and therefore are part of practically every subset. If these data points are not well describable by the applied model, they may cause larger residuals in the smaller datasets as opposed to the full dataset where their effect largely averages out.
The distribution of the two dimensional residuals like visible in Figure 4.14 (left) suggests that there is some systematic in the relation between measured pointing and nominal pointing which can not be modelled by a constant camera offset alone. One possibility to refine the model would be to add further components that are mechanically motivated. In order to understand the pointing capabilities of the MAGIC telescope better, this approach would be desirable. But as the goal of this thesis is the study of a pointing solution for the MST, the approach of applying a mathematically motivated correction model was chosen for the following studies. For this, the parameters $\Delta\phi(\phi,\vartheta)$, $\Delta\vartheta(\phi,\vartheta)$ were made dependent on the nominal pointing direction. As the dependence is expected to be periodic and continuous in both parameters ϕ and ϑ, it can be described by a Fourier series. For technical simplicity, a purely real representation is chosen:

$$\Delta\xi(\phi,\vartheta) = \sum_{i=0}^{m}\sum_{j=0}^{n}\Big(\alpha_{\xi,i,j}\cos(i\phi)\cos(j\vartheta) + \beta_{\xi,i,j}\cos(i\phi)\sin(j\vartheta) \tag{4.21}$$

$$+\gamma_{\xi,i,j}\sin(i\phi)\cos(j\vartheta) + \delta_{\xi,i,j}\sin(i\phi)\sin(j\vartheta)\Big) \tag{4.22}$$

with $\xi \in \{\phi,\vartheta\}$, Fourier coefficients $\alpha_{\xi,i,j}$, $\beta_{\phi,i,j}$, $\gamma_{\xi,i,j}$, and $\delta_{\xi,i,j}$, and orders m and n. Of the coefficients, $k = 8(m+1)(n+1)-4(m+n)-6$ correspond to non-vanishing terms, i.e. terms that do not include $\sin(0)$. The special case where $\Delta\phi$ and $\Delta\vartheta$ are constant is retrieved in this representation with $m = n = 0$. The coefficients that minimise the residuals for a given dataset can be calculated analytically as the solution of a system of linear equations. This was done analogous to the procedure described in 4.1.
In the following, the showcase construction of a specific Fourier model is shown using the same subset of SetT as for the constant offset model described above. This model consists of a Fourier series of third order ($m = n = 3$). With these values of m and n, good results are expected because $k = 98$ is smaller than the number of data points ($115 \cdot 2 = 230$), which prevents overfitting, but still large enough to model the data satisfactory. In Figure 4.15 (left), it can be seen that the obtained model reproduces the residuals of the constant offset model quite well. The residual deviations after application of the Fourier model are also visualised in this figure. One large outlier with 81.1″ is clearly visible. The mean residual pointing deviation obtained for the subset that was used for the model construction is 8.2″ with a standard deviation of 8.6″. When the correction model is applied to the complete dataset, the obtained mean residual is 14.1″ while the standard deviation increases to 13.5″.
In a more systematic way of finding a Fourier pointing model that describes the data well, different configurations of Fourier orders were tested with different minimum distances d between the data points used for selecting subsets for the model construction. For each combination of Fourier order and minimum distance, the minimum

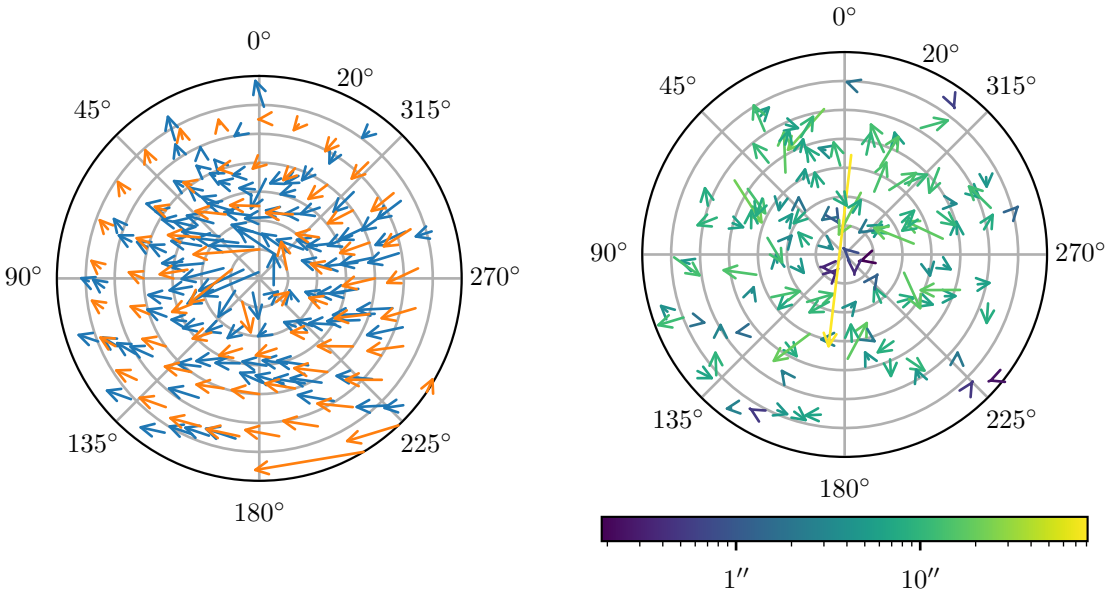

Figure 4.15: Left: Residual pointing deviations of the constant camera offset model (blue) and the difference between the constant camera offset model and the more precise Fourier model (orange). Arrow scale: 400. **Right:** Residual pointing deviations of the Fourier model. Arrow scale: 3000.

mean residual from 100 different realisations of the data selection (i.e. 100 different seeds were used) was calculated. The results are shown in Figure 4.16. It can be seen that the Fourier order that yields the model with the smallest mean residuals increases with decreasing d. This is expected as denser sampling means more available data points for the model construction and these allow for higher orders of the Fourier series. The smallest residuals could be reached with $d = 1°$. As the improvement over $d = 2°$ is only marginal and in order to not run into the limit of using all available data for model construction ($d = 1°$ corresponds to a selection of $\sim 1/3$ of the available data), smaller values of d were not tested.
For the data sets Set10, Set20, and SetT, a model with $d = 1°$ and with a Fourier order of 4, 2, and 6, respectively, is considered optimal. The reached mean and maximum values of the residuals can be found in Table 4.3. The corresponding residual distributions are visualised in Figure 4.17. Despite their different coverage of the sky, image recording modes, and camera operation modes, all three data sets yield very similar pointing model residuals. This makes no evaluation of the different data acquisition parameters like exposure time and CCD chip temperature possible.
The obtained residuals, which are quite large in comparison to the pointing deviations obtained in simulation studies, can be caused by multiple reasons. One possible explanation is that the telescope was subject to inelastic deformations during the data acquisition. Naturally, such effects can not be modelled. Another effect could be that there are errors in the identification of pointing measurements and information from the drive system of MAGIC which can not be sorted out with the level of access to the MAGIC systems that for available for this thesis. It could also be that real images

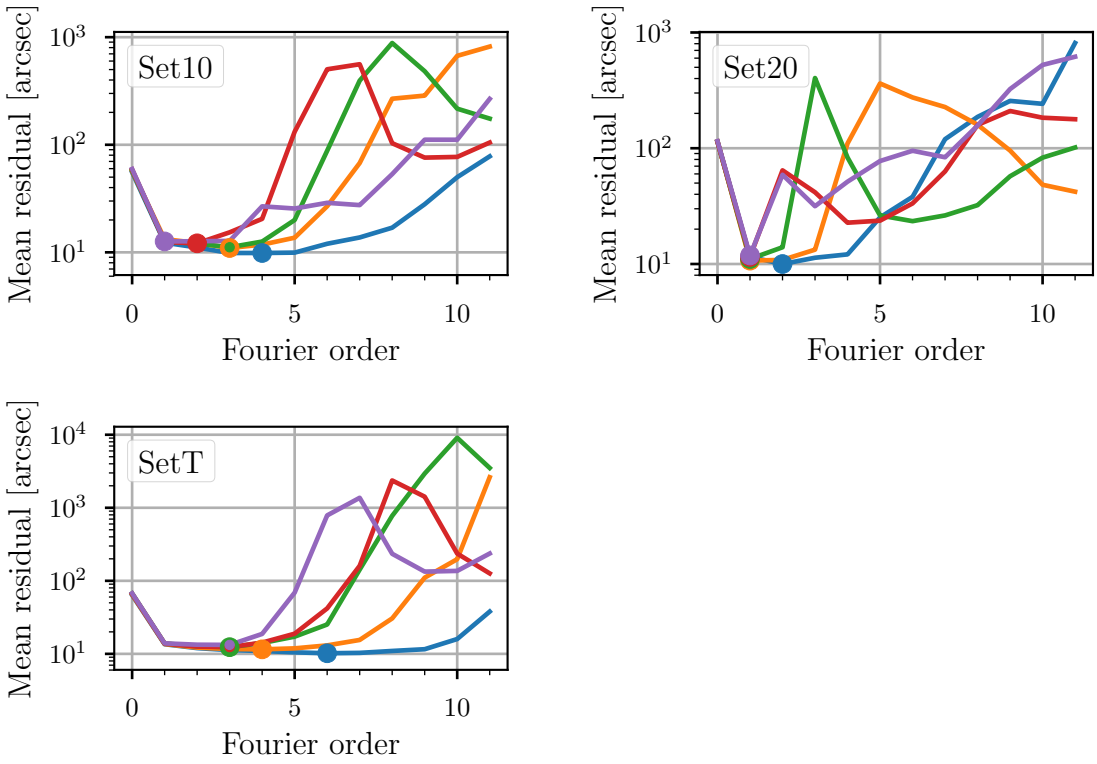

Figure 4.16: Mean residual deviation between modelled and reconstructed pointing direction as a function of the order of the used Fourier model. Different minimum selection radii are represented with different colours: blue: 1°, orange: 2°, green: 3°, red: 4°, purple: 5°. The minimum of each curve is marked with a circle.

of the sky comprise effects like distortions and spots that do not correspond to stars which are not included in the software used for the simulation studies.

4.4 Conclusion

In this chapter, the software framework libPointingMST has been introduced and it has been shown that it is a promising candidate for the analysis of pointing images of the future medium size telescope of CTA. Simulated data was used to show that the reconstruction of the pointing direction from the information in a set of exactly known star spots in an image works as expected. Simulation studies with pixelated images showed that precisions in the range of few arcseconds can be reached. The analysis of real images taken at the site of the MAGIC telescopes, where conditions close to the later application at CTA are available, showed that the pointing directions of these images can be reconstructed with a precision of at least 10″ on average. Whether these 10″ are a hard limit of the hardware and software system or whether they are caused by systematics in the data acquisition process of the test campaign is not yet clear. The efficiency with which images from the test campaign could be solved is

Table 4.3: Overview over residuals of the optimal pointing models derived for data from the test campaign at MAGIC.

Dataset	Mean residual	Maximum residual
Set10	9.9″	104″
Set20	10.0″	158″
SetT	10.2″	100″

close to 100 %.
In order to disentangle errors in the data acquisition and in the image recording and analysis, a test campaign at one of the H.E.S.S. telescopes is planned. A new simulation software which can simulate more realistic images and that does only depend on publicly available Python packages is also currently worked on. If future tests show that the precision of the current pointing system is not sufficient for the requirements of CTA, the most promising possibility of improvement is suggested to by an update of the imaging system. Using a camera chip with higher pixel resolution could decrease the uncertainties in the spot extraction while a lens with a shorter focal length would increase the image area with visible star spots. For a complete pointing solution, it is also necessary to analyse pointing images that are taken during pointing runs and also the information that is contained in the positions of LED spots in the images. This is currently investigated in a further PHD-thesis.

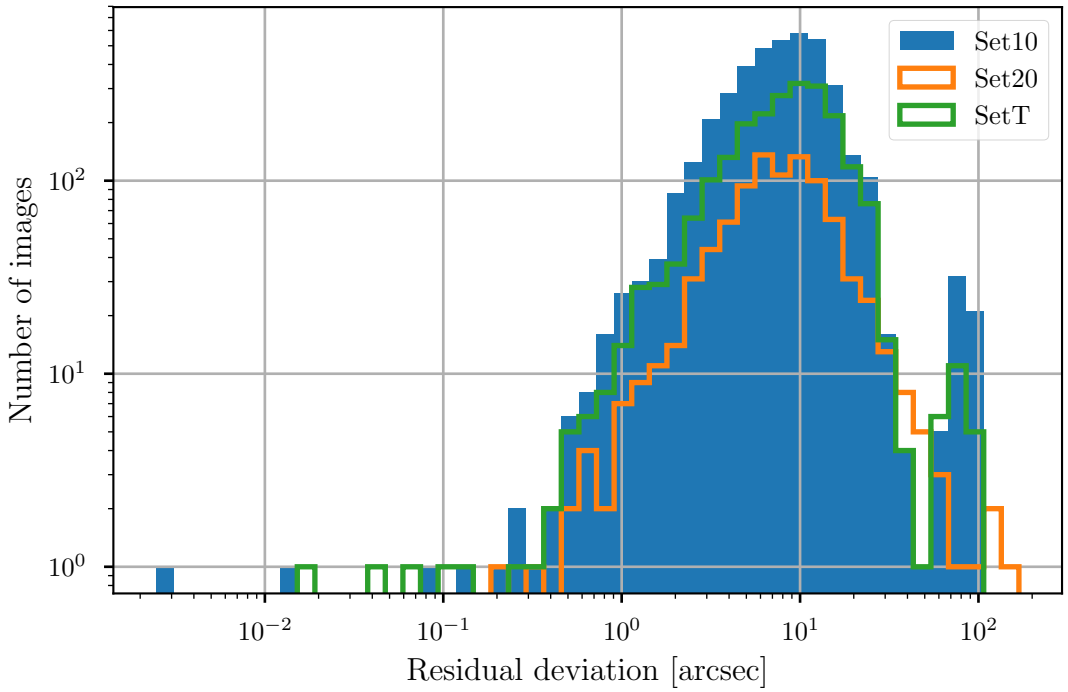

Figure 4.17: Distribution of residual deviations between optimal pointing models and reconstructed pointing directions for the three different data sets of the MAGIC campaign.

Chapter 5

3D likelihood analysis of the Large Magellanic Cloud

The Large Magellanic Cloud (LMC) is a dwarf galaxy in the Local Group at a distance of $\sim 50\,\mathrm{kpc}$ [Pietrzyński et al. 2013]. As a starforming galaxy, it constitutes an interesting source region for many different wavelength bands and different observatories. For VHE gamma ray astronomy, the LMC is of particular importance because it can be spatially resolved as opposed to more distant galaxies like M31, M82, and NGC 253. Its companion, the Small Magellanic Cloud (SMC), is also spatially resolvable by IACTs, but its geometry is less favourable for observations due to its disturbed shape (Scowcroft et al. [2016], Nikolaev et al. [2004]) and its starforming regions are less active. The LMC provides gamma-ray astronomy with an outside view of a galaxy where the interpretation of signals is not influenced by uncertainties due to imprecise distance estimations and line-of-sight confusion like it is the case for the Milky Way.
There are two main goals of the analysis in this thesis. The first is to re-investigate LMC data from the H.E.S.S. telescopes with the ctools software package and the maximum likelihood method to provide a further verification of this method and the software. The second aim is to use the advantages of the maximum likelihood method to study whether diffuse gamma-ray emission is detected coming from the LMC in addition to the already known point sources. The search for diffuse emission with classical on-off region based analysis methods is strongly limited by the lack of suitable off regions for the large on regions.
In the first section of this chapter, the astrophysical objects in the LMC that are of interest for VHE gamma-ray astronomy are introduced. In the second section, the analysed dataset is introduced. The analysis of the already detected point sources is described in the third section before remaining excess and diffuse emission are investigated in the last two sections.

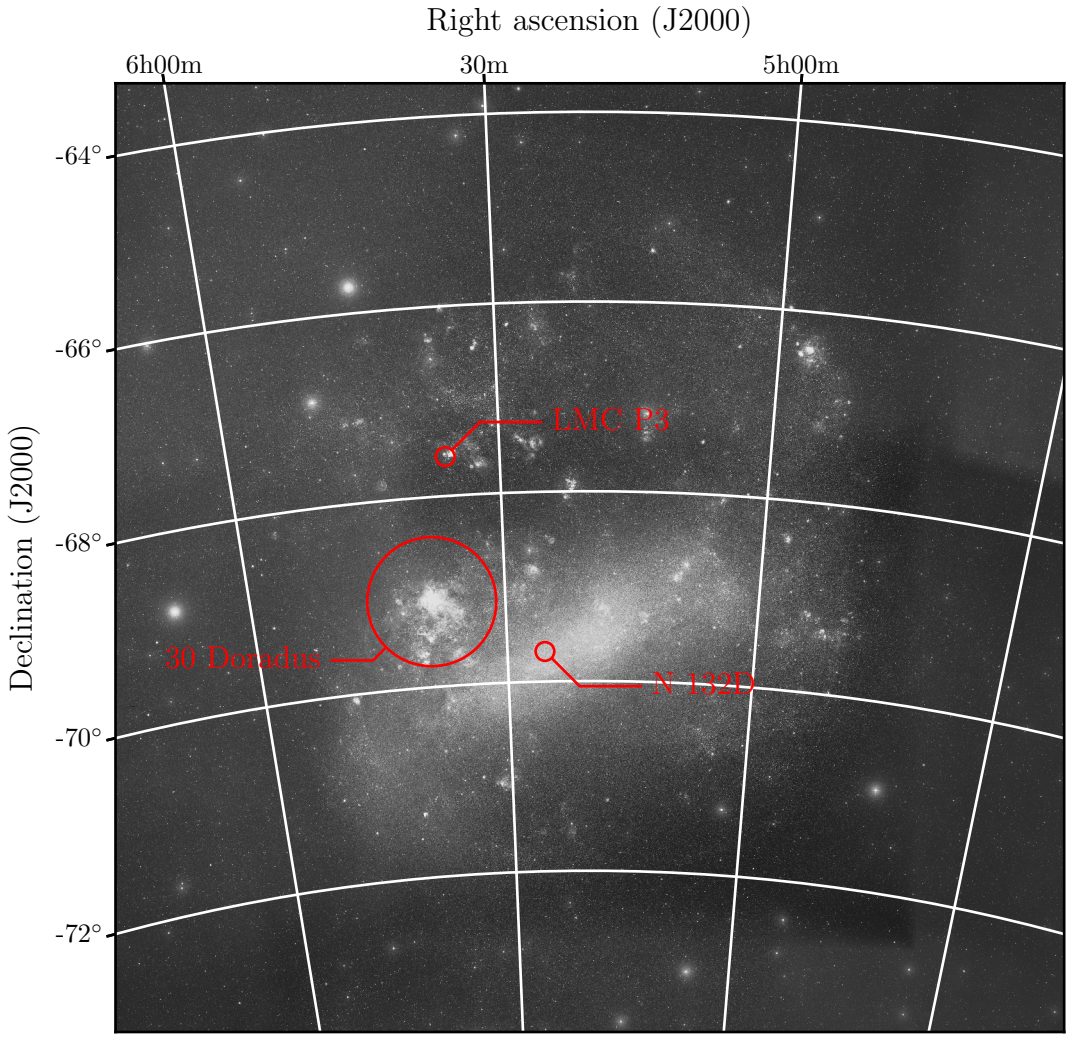

Figure 5.1: Image mosaic of the Large Magellanic Cloud in visible light. The positions of the known emitters of VHE gamma-rays, LMC P3 and N 132D, are indicated together with the 30 Doradus region. Image data was obtained from the Digitized Sky Survey (`http://gsss.stsci.edu/SkySurveys/SkySurveys.htm`).

5.1 Introduction to the region

The LMC can be observed in a region with a diameter of ~ 11.5° centred around the position RA = $05^{h}23^{m}34^{s}$, Dec = -69°45.4′ (epoch J2000) [Vaucouleurs et al. 1976] in many different wavelength regimes. In Figure 5.1, an optical view of the dwarf galaxy is shown. One of the most prominent features of the LMC is the 30 Doradus region in the north-eastern part, centred around RA = $05^{h}38^{m}42^{s}$, Dec = −69°6′3″ [Høg et al. 2000]. An optical image zoomed into 30 Dor can be seen in Figure 5.2. This region, also known as the Tarantula Nebula, is one of the most active starburst regions in the

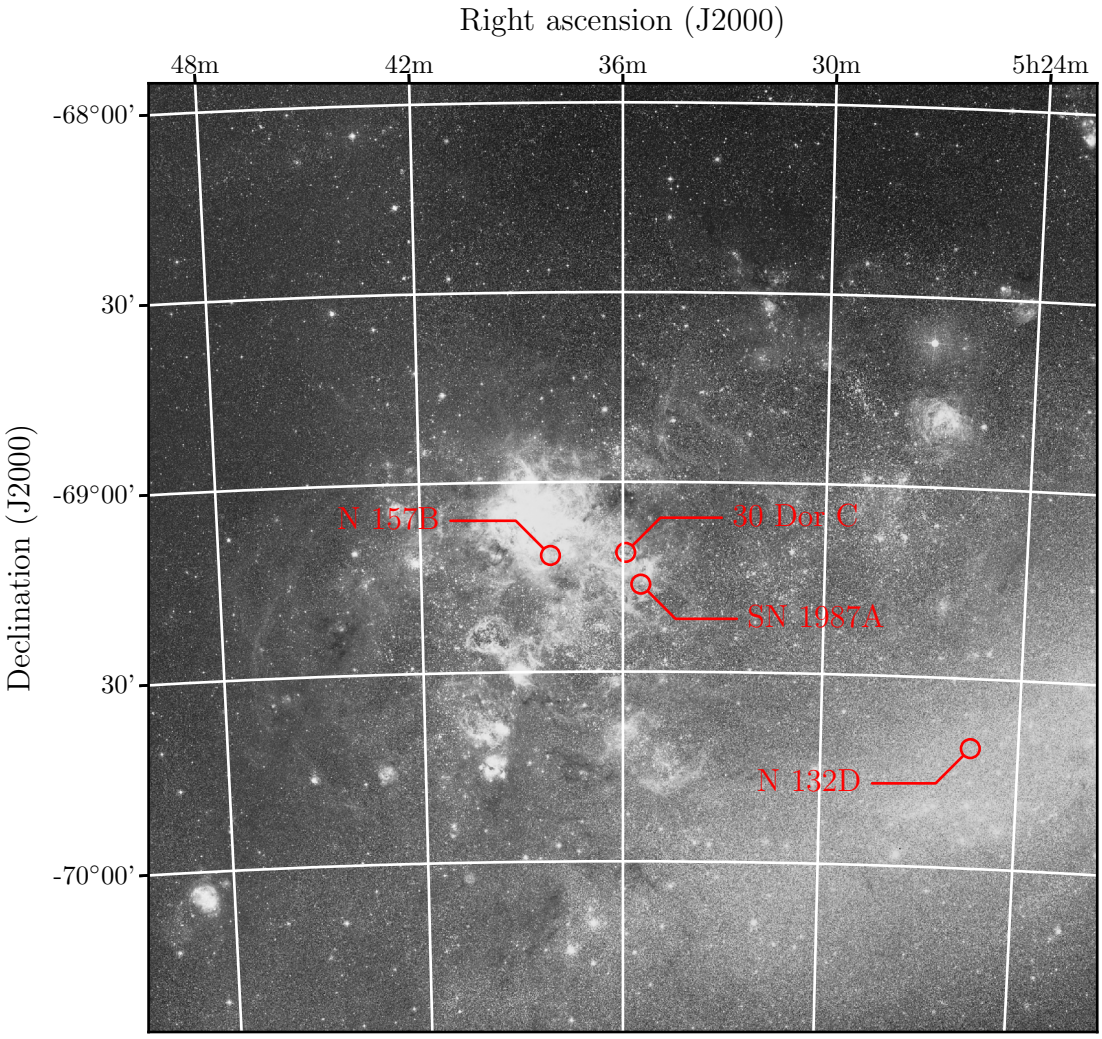

Figure 5.2: Zoomed version of image mosaic in visible light showing the 30 Doradus region in more detail. The sources of VHE gamma-rays N 157B, 30 Dor C, and N 132D are marked together with the position of the supernova remnant of SN 1987A. Image data is the same as used for Figure 5.1

Local Group. It hosts several star clusters like e.g. NGC 2060. Within this cluster, the VHE gamma-ray source HESS J0537–691 was detected by H.E.S.S. Collaboration et al. [2012] at the position of the supernova remnant (SNR) N 157B. The emission of this source was associated with the pulsar wind nebula (PWN) of the pulsar PSR J0537–6910 inside the remnant. With a spin-down power of $\dot{E} = 4.8 \times 10^{38}\,\mathrm{erg\,s^{-1}}$, this pulsar is the most powerful known pulsar, surpassing even the Crab with a spin-down power of $\dot{E} = 4.6 \times 10^{38}\,\mathrm{erg\,s^{-1}}$. Coincident emission from this source was also detected in the HE band by Fermi-LAT [Ackermann et al. 2016].
Another source that was detected in the VHE band previously is the superbubble

30 Dor C. A superbubble is a cavity in the interstellar medium (ISM) with a dense shell that was swept up by stellar wind of massive stars and their supernovae [Smith et al. 2004]. 30 Dor C has been detected in x-rays [Wang et al. 1991] and in the VHE band but not in HE gamma rays. The gamma-ray emission can be explained by either IC scattering of VHE electrons which are also producing the measured x-ray photons in synchrotron radiation or by hadronic processes. The superbubble resides within the 30 Dor region, to the west of N 157B.
The remnant of SN 1987A, the nearest supernova that was observable with the naked eye in modern times, is located at the edge of the 30 Dor region at RA = $05^{\mathrm{h}}35^{\mathrm{m}}28^{\mathrm{s}}$ Dec= $-69°16'11''$ [Whitney et al. 2008]. The evolution of the core-collapse supernova has been observed with various instruments in different wavelengths. This has led to invaluable insights into the processes within such an object. VHE gamma-ray emission from SN 1987A has been predicted [Berezhko et al. 2015] but not yet detected.
To the north of the 30 Dor region, variable emission from the position of the x-ray source CAL 60 [Long et al. 1981] has been detected in the VHE-regime [H.E.S.S. Collaboration et al. 2018a]. The source, which will in the following be called LMC P3 and which lies within the SNR DEM L241, was also observed to have a modulation with a period of 10.3 d in HE gamma-rays [Corbet et al. 2016]. The variability can be explained by a binary system of two massive objects. This is likely a neutron star with a massive star companion. Crampton et al. [1985] identified a positionally coincident O5 III(f) star as a candidate for the massive star. There are two proposed scenarios for the origin of the emission of such a gamma-ray binary: Electrons can be accelerated close to the neutron star or in the shock-front between pulsar wind and stellar wind. These relativistic electrons can produce VHE gamma-rays via IC upscattering of stellar photons. In the other proposed scenario, the emission is caused by mass-accretion of stellar wind onto the dense companion object.
Close to the centre of the LMC, at RA = $05^{\mathrm{h}}25^{\mathrm{m}}02^{\mathrm{s}}$, Dec= $-69°38'29''$, the SNR N 132D is located. This remnant is observable in a variety of wavelengths ranging from radio [Dickel et al. 1995] to x-ray [Hughes et al. 1998]. Models predict that it is quite young with an age of few thousand years and that the supernova had a huge explosion energy of 6×10^{51} erg. The source has been detected both in the HE band by Fermi-LAT [Ackermann et al. 2016] and in the VHE band by H.E.S.S. [H.E.S.S. Collaboration et al. 2015].
In addition to the already described point sources, Fermi-LAT detected diffuse HE gamma-ray emission in the LMC. This diffuse emission was modelled with four two-dimensional Gaussian shaped model components, each spectrally described by a power law. There is no unambiguous explanation for these large scale signals with $1\,\sigma$ sizes of 0.4° to 1.95°. One possibility is that the photons originate from a set of individual point sources that can not be spatially resolved by the instrument. It is also proposed that the diffuse radiation is caused by a large population of cosmic rays that interact with interstellar gas.

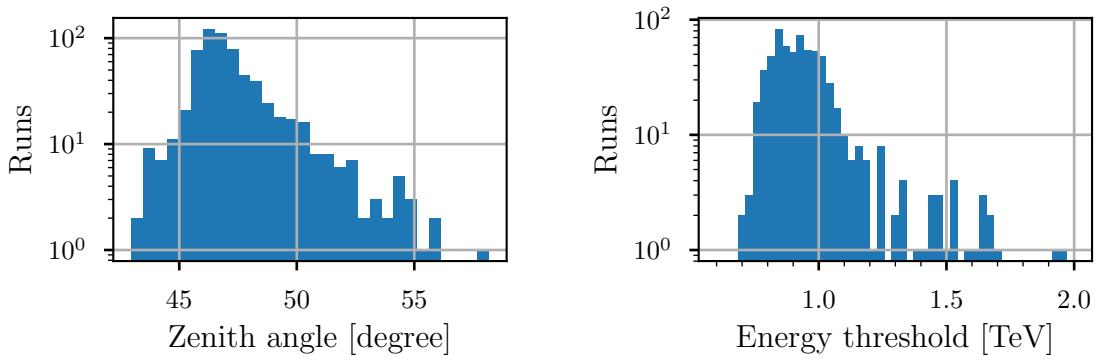

Figure 5.3: Left: Histogram of pointing zenith angles of all runs in the dataset used for the analysis. **Right:** Histogram of lower energy thresholds of all observations.

5.2 Data selection

The dataset that was used for the analysis of the LMC in this thesis includes in total 643 H.E.S.S. runs from phase I and phase II. These are all available runs that have a pointing position that deviates less than 8° from the position RA = $05^{h}34^{m}21.6^{s}$, Dec = $-68°52'0.12''$ and that pass standard spectral quality cuts [Hahn et al. 2013]. In the analysis, only data acquired with the smaller telescopes CT1-4 was taken into account. The low level data was reconstructed via the Hillas-parameter based approach while the gamma-hadron separation was performed with the boosted decision tree method described in 2.4 (analysis configuration = std_zeta_fullEnclosure). The high level data is part of the H.E.S.S. FITS export Prod05 of the Heidelberg analysis chain. For estimations of the residual background level, the template background model that is described in 2.5 is applied.
The data accumulates to a total lifetime of 292.6 h, during which 1 990 884 gamma-like events have been measured. H.E.S.S. can only observe the LMC under relatively large zenith angles. The runs in the used dataset where performed with zenith angles between 43° and 58°. The corresponding distribution of zenith angles is shown in the left panel of Figure 5.3.
Further selection cuts were applied to the described data to obtain the final dataset for the analysis. A spatial cut removes all events that were reconstructed with an arrival direction with a larger angular separation than 1.5° from the pointing direction of the corresponding run. This rather low value was chosen in order to be able to analyse lower energetic photons with fewer systematic errors. For each run, save energy thresholds within which systematic uncertainties are considered sufficiently low were derived individually. The lower energy thresholds were chosen such that the absolute value of the energy bias in the photon reconstruction is lower than 10 % over the whole field of view. As shown in 2.5, the energy at which E_{bias} exceeds a certain value rises with increasing distance to the pointing direction. Choosing a field of view selection cut of 1.5° therefore yields lower thresholds than selection cuts with a larger field of view. For each individual observation, it was also checked

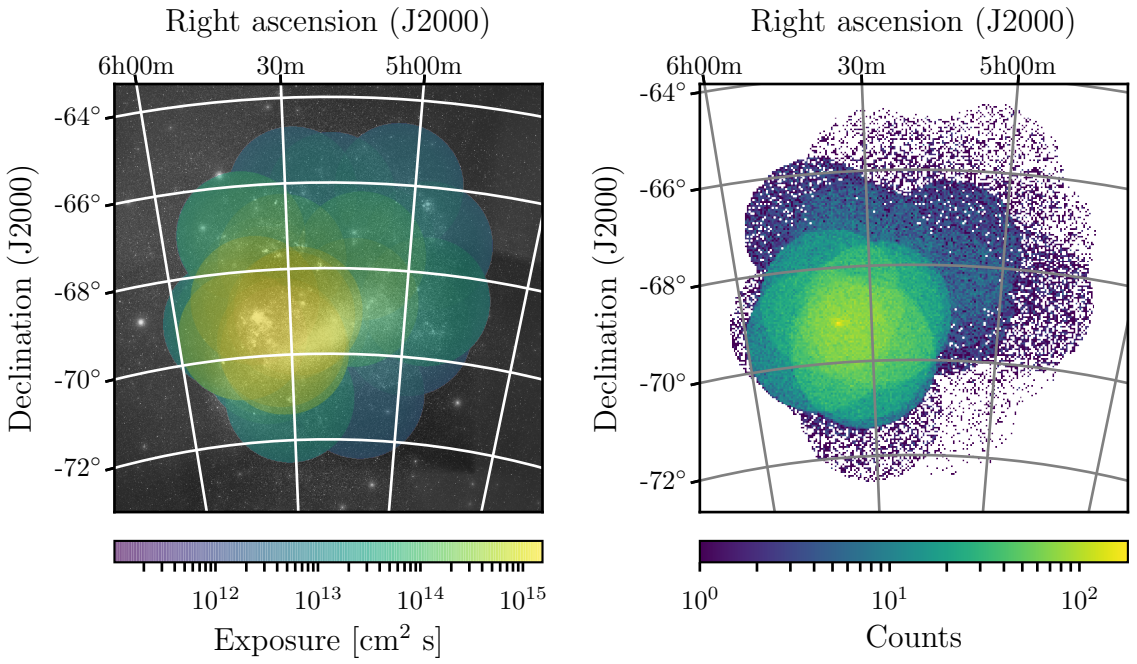

Figure 5.4: Left: Map of effective exposure at 1 TeV after event selection, summed up over all observations used in the analysis. The underlying image is the optical mosaic from Figure 5.1. **Right:** A spatial histogram of all events used for the analysis after selection cuts (counts map).

whether the low energy threshold is above a critical energy that is defined by the corresponding background template: Experience showed that a suitable energy cut is the energy at which the background template predicts the most events, integrated over the field of view [Mohrmann et al. 2019]. Below this energy, the background construction is dominated by threshold effects of the different generating observations. For the observations used for this analysis, the lower energy threshold defined by the background template is always lower than the threshold defined by the maximum energy bias. The obtained distribution of all lower energy thresholds is plotted in the right panel of Figure 5.3. The upper energy threshold was chosen as either 100 TeV, which is larger than any photon energy in the dataset, or as the upper energy above which E_{bias} is larger than 10 % at 1.5° offset from the pointing position.
After the application of the described cuts, 408 977 events remain in the dataset. The spatial shape of the effective exposure, i.e. the exposure time × effective area at a given location summed up over all runs, is depicted in the left panel of Figure 5.4. A map showing a histogram of the selected events is plotted in the right panel. It is evident that the area with the deepest exposure coincides with the 30 Dor region, where the largest density of gamma-ray sources is expected.

5.3 Modelling of point sources

The first step carried out in the analysis was the modelling of the point sources whose detections had already been reported in earlier publications. For this, model descriptions of the sources N 157B, 30 Dor C, N 132D, and LMC P3 were added to the background template model in successive steps. Each of the sources was spatially modelled as a point source and spectrally described by a simple power law (see Equation 2.15). For each combined model consisting of background and point sources, the best fit parameters were derived with the maximum likelihood optimiser ctlike. The free parameters of each fit are given by a normalisation factor and a spectral tilt for each background template (1286 parameters) and four parameters, namely right ascension, declination, flux normalisation, and spectral index, for each point source. Spectral and spatial values of earlier publications were used as starting values for the fit. Sky maps of the model and the residuals after each step, integrated over the whole energy range, are depicted in Figures 5.5 and 5.6. Table 5.1 shows the best fit values derived in the analysis together with reference values from other analyses. The table also lists the TS values which measure the improvement of the likelihood between the different steps. The derived significances $S = \sqrt{\mathrm{TS}}$ are also included.
All listed point sources besides N 132D were detected with a significance larger than 5 σ. For latter supernova remnant, evidence with a significance of only 3.9 σ was found. It is not surprising that the measured significance of this source is lower than the 4.7 σ obtained with the on-off-region based analysis in H.E.S.S. Collaboration et al. [2015] because this classical approach is more sensitive to point source emission. From the position of SN 1987A, no excess was detected and attempts to fit a corresponding model component resulted non-converging fits.
In the following, the differences of the obtained spatial and spectral parameters to the reference values will be discussed.
When comparing the results of this analysis with those from the reference publications, one has to keep in mind that different analysis techniques were applied. One big difference is that in earlier analyses, position fits have been carried out with spatially binned data, while an unbinned approach has been chosen for this analysis. This likely has an influence on the best fit positions found for point sources.
The position of N 157B is subject to some uncertainties due to emission leakage by 30 Dor C. The superbubble was not detected in Komin et al. [2012] where the reference position of the PWN was taken from. The discrepancy might be explained by the fact that the system of the two sources is now described with two point source models in this analysis. The detected hotspot (see Section 5.4) might also contribute to the deviation. This hotspot, that is detected as a spatially separate source in this analysis but was likely part of the emission detected in the reference publication, might also be the reason for the difference in the measured flux normalisation. The normalisation obtained with the composite model case is closer to the reference than that obtained with the single point source case.
The positional deviation of 30 Dor C of 77″ in declination is not understood and the only explanation might be the difference between a binned and an unbinned fit.

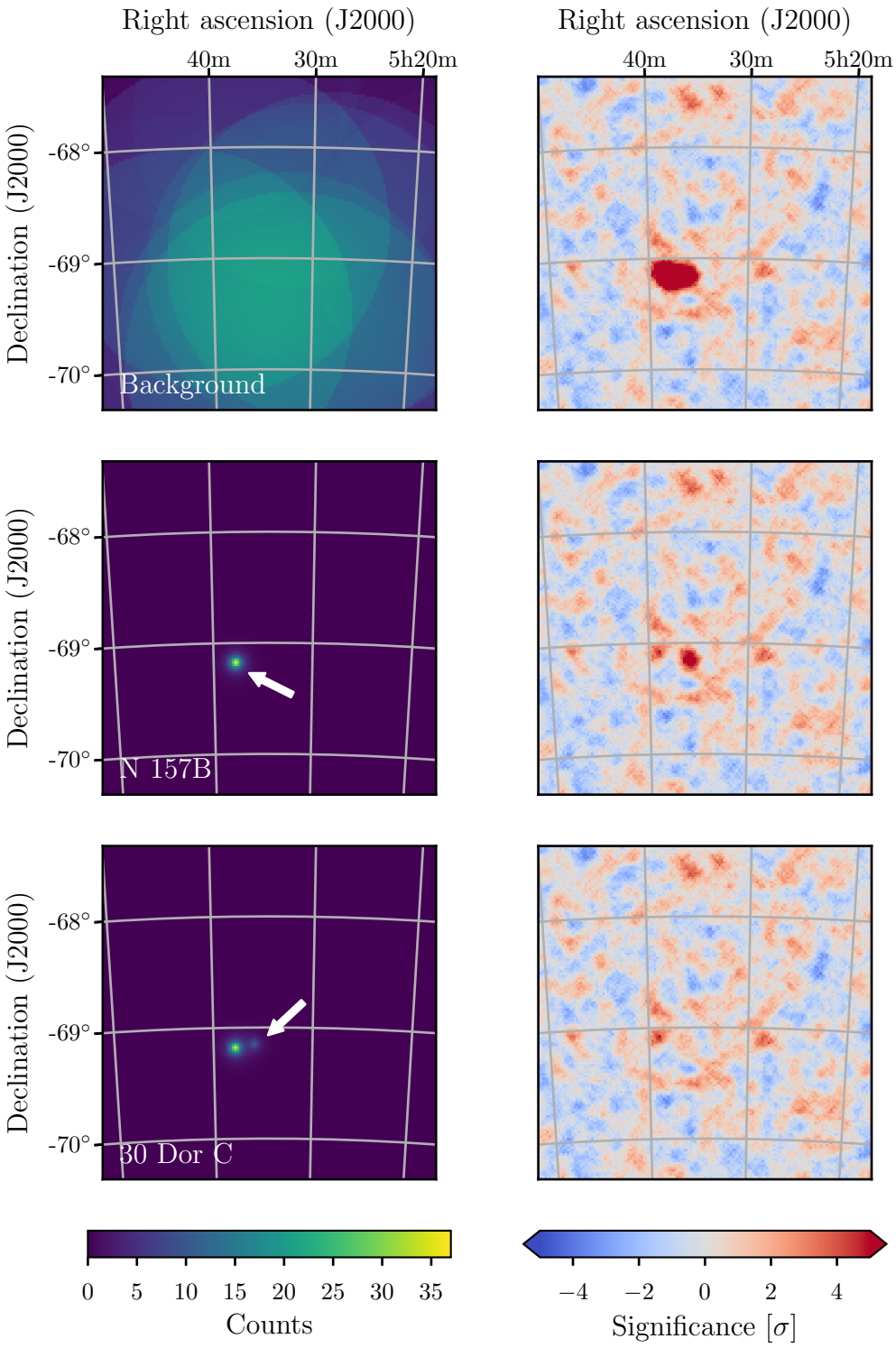

Figure 5.5: First three iterations of successive build of a model description of known point sources in the LMC. **Left:** Sky maps showing the predicted counts of the corresponding model. The predicted counts of the background template are only shown in the first iteration and are omitted in the other plots for better visibility of the other components. **Right:** Residual significance maps that show the remaining excess. Detected and modelled counts are correlated with a top-hat kernel of radius 0.08° prior to the calculation of the residuals.

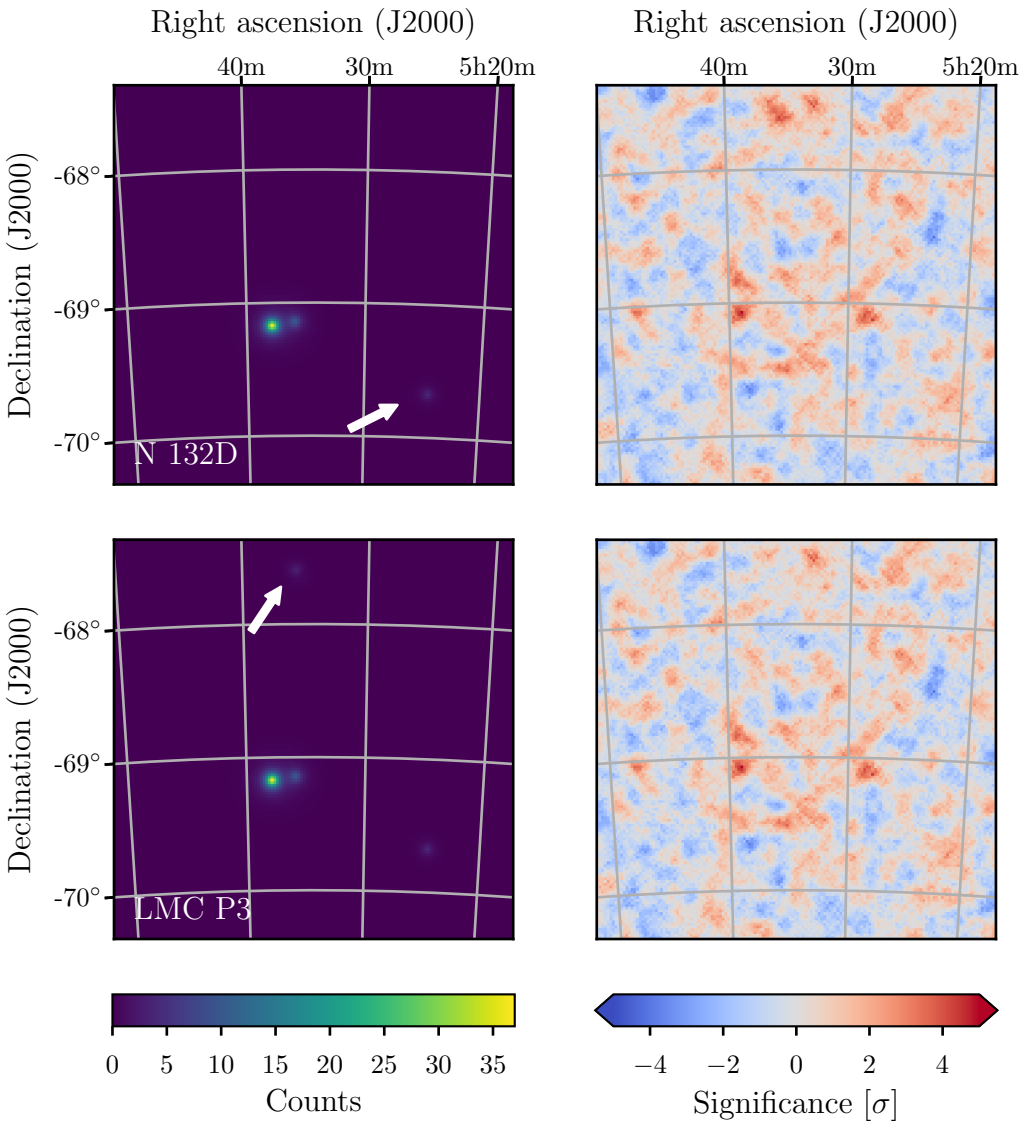

Figure 5.6: Same as Figure 5.5 but for the last two iteration steps of model generation.

The measured flux at 1 TeV might be a bit higher than in the reference due to the correlation of this parameter with the spectral index, which was in turn fit to a bit softer values.
The position of N 132D is difficult to compare to the reference, because the cited position was derived in radio-band observations.
The choice of the field of view cut of 1.5° might have introduced some systematic in the determination of the position of LMC P3. Because this source is close to the edge of the field of view for some pointing positions, the best fit position might be shifted a bit towards the centre due to the exclusion of some of the emission.

5.4 Analysis of residuals

After the four known point sources had been modelled, the residuals after model subtraction were investigated for hints of incompleteness of the model. In the residual significance map of the last modelling iteration (see bottom left panel of Figure 5.6), which is produced with the model of four point sources, there is exactly one position left where the residual significance exceeds a value of five standard deviations. This hotspot, which is in the close vicinity of N 157B, was tested for whether an additional point source at that position would lead to a significant improvement of the model description. A dedicated fit of a suitable model revealed that the likelihood can indeed be increased with a TS value of 26.0, corresponding to a significance of $5.1\,\sigma$. The best fit model parameters are listed in Table 5.1. Because this component has been found by searching for hotspots in the residual significance map, without any a priori assumption where an additional source might be found, the look-elsewhere effect should be considered when evaluating the significance of the signal. The trial factor was estimated via the number of times a point source fits inside the field of view in which the search has been carried out. With a size of the map of $\sim 3° \times 3°$ and a typical PSF with a width of 0.08°, a trial factor of 1406 is obtained. Applying this factor yields an estimated post-trial significance of the modelled point source of $3.5\,\sigma$. This shows that the detection of a new point source can not be claimed with certainty.
Another possible interpretation of the observed hotspot in the residual map is that it is part of the emission of N 157B and that this source shows some extension. This was tested by combining the spatial models of the new point source and of N 157B into a single model component with one spectral description. This was achieved with the composite model functionality of gammalib. The fit with this composite model has one free parameter fewer than the fit treating the hotspot as a separate source: the spectral index of the new point source component is omitted, while its flux normalisation is replaced by a scale factor between the two model constituents. Thus, the model with two separate sources can be seen as a more general description of the composite case. The parameters derived via the fit are also listed in Table 5.1. The resulting scale factor that models the quantitative relation between the flux of the stronger and the weaker part is 4.7 and the measured separation between

Table 5.1: Results from analysis of the four known point sources. The best fit values are presented above reference values in brackets. The corresponding references are given via footnotes. The results of the modelling attempts of the hotspot presented in Section 5.4 are given at the bottom.

Source	TS	σ	Right ascension (J2000)	Declination (J2000)	Flux at 1 TeV $[1 \times 10^{-12}\,\mathrm{cm^{-2}\,s^{-1}\,TeV^{-1}}]$	Spectral index
N 157B	634.8	25.2	$5^{\mathrm{h}}37^{\mathrm{m}}(50 \pm 2)^{\mathrm{s}}$	$-69°10'(39 \pm 10)''$	1.1 ± 0.1	-2.7 ± 0.1
			$[5^{\mathrm{h}}37^{\mathrm{m}}(44 \pm 2)^{\mathrm{s}}]$ [a]	$[-69°09'(57 \pm 11)'']$ [a]	[1.3 ± 0.1] [b]	[-2.8 ± 0.1] [b]
30 Dor C	45.9	6.8	$5^{\mathrm{h}}35^{\mathrm{m}}(52 \pm 6)^{\mathrm{s}}$	$-69°08'(53 \pm 31)''$	0.3 ± 0.07	-2.8 ± 0.2
			$[5^{\mathrm{h}}35^{\mathrm{m}}(55 \pm 5)^{\mathrm{s}}]$ [b]	$[-69°11'(10 \pm 20)'']$ [b]	[0.16 ± 0.04] [b]	[-2.6 ± 0.2] [b]
N 132D	15.6	4.0	$5^{\mathrm{h}}24^{\mathrm{m}}(33 \pm 9)^{\mathrm{s}}$	$-69°40'(44 \pm 40)''$	0.12 ± 0.06	-2.3 ± 0.3
			$[5^{\mathrm{h}}25^{\mathrm{m}}02^{\mathrm{s}}]$ [c]	$[-69°38'39'']$ [c]	[0.13 ± 0.05] [b]	[-2.4 ± 0.3] [b]
LMC P3	25.8	5.1	$5^{\mathrm{h}}35^{\mathrm{m}}(44 \pm 6)^{\mathrm{s}}$	$-67°36'(19 \pm 42)''$	0.32 ± 0.12	-2.5 ± 0.3
			$[5^{\mathrm{h}}36^{\mathrm{m}}(00 \pm 04)^{\mathrm{s}}]$ [d]	$[-67°35'(11 \pm 23)'']$ [d]	[0.20 ± 0.04] [d]	[-2.5 ± 0.2] [d]
Hotspot	26.0 [e]	5.1	$5^{\mathrm{h}}39^{\mathrm{m}}(08 \pm 8)^{\mathrm{s}}$	$-69°05'(36 \pm 40)''$	0.2 ± 0.1	-2.9 ± 0.3
Composite	25.2 [e]	5.0	$5^{\mathrm{h}}38^{\mathrm{m}}(03 \pm 2)^{\mathrm{s}}$ [f]	$-69°09'(50 \pm 11)''$ [f]	1.2 ± 0.1	-2.7 ± 0.1

[a] Komin et al. [2012]
[b] H.E.S.S. Collaboration et al. [2015]
[c] Mauch et al. [2003] (radio band observation)
[d] H.E.S.S. Collaboration et al. [2018a]
[e] Relative to model with four known point sources
[f] Centre of gravity position of composite model constituents

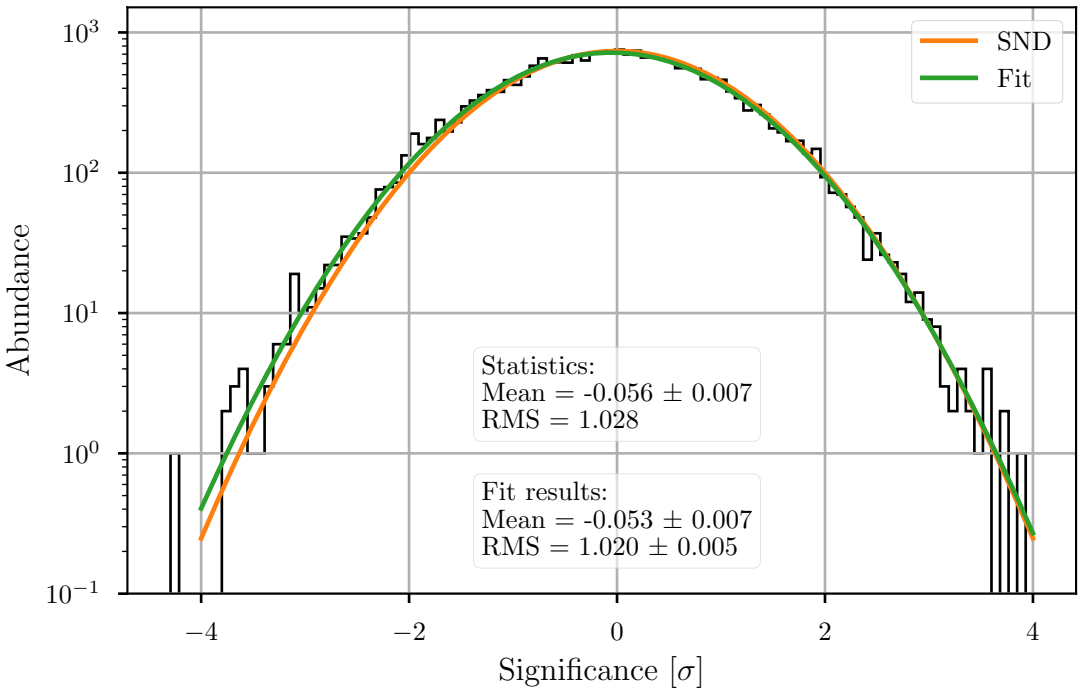

Figure 5.7: Residual significance entry distribution for the zoomed skymap centred at the 30 Dor region. The entries of the spatial bins have not been correlated with any kernel. Residuals have been summed up for all energies. The shape of a standard normal distribution with a width of 1 and centred at zero is shown together with a Gaussian fit. The statistics of the histogram and the best fit parameters are also given.

the two constituents is 0.15°. Over the description with only one point source at the position of N 157B, the composite model is favoured with a TS value of 25.2. The improvement of the likelihood when switching from the composite case to the case with two different spectra corresponds to a TS of 0.8. Due to this insignificant improvement, the simpler composite model was used to complete the model describing the emission of all point sources. This model, consisting of the composite source (N 157B + Hotspot), 30 Dor C, N 132D, and LMC P3, was used as the starting point for the search for diffuse emission described in the following section.
With this complete model of all point sources, the field of view already seems to be well described. This can be seen in the residual significance entry distribution, shown in Figure 5.7. The distribution is very well described by a standard normal distribution and the histogram has no entries at significances larger than 4, which would be a hint for additional emission that is not described by the model.
Also the distributions of the background best fit parameters of normalisation and spectral tilt, which are depicted in Figure 5.8, suggest a good description of the data. The obtained width of the normalisation distribution of 0.12 is close to the one that was reached in the checks when constructing the background model [Mohrmann et al. 2019].

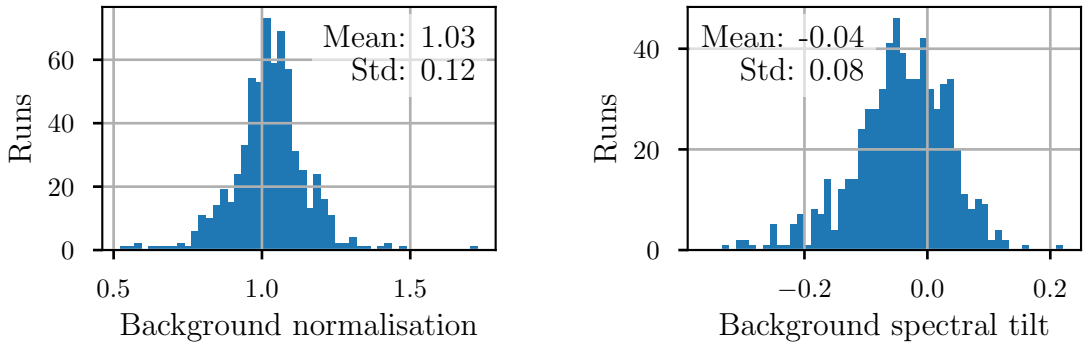

Figure 5.8: Left: Distribution of best fit normalisation factors of the background templates for the optimised model consisting of the point sources and the background. **Right:** Distribution of best fit spectral tilts of the background templates. A positive tilt means that the spectrum was fit harder than it originally is in the template.

5.5 Search for diffuse emission

For a first check whether large scale diffuse emission from the LMC is detected, residual significance maps after modelling all point sources were examined. These maps were correlated with a large radius in the range of the expected emission. Such a map is depicted in the top left panel of Figure 5.9. In this map, some positive excess is visible coincident with the extended emission region G2 detected in HE gamma-rays. The G2 region was modelled in Ackermann et al. [2016] with a 2-dimensional Gaussian with a $1\,\sigma$ extend of 0.7° centred at the position RA = $5^{\mathrm{h}}33^{\mathrm{m}}36^{\mathrm{s}}$, Dec = −69°9′0″. A logical step here is now to describe this excess with an extended, Gaussian shaped model component. Several fits of different spatial and spectral models have been carried out to reach such a description. All of these either did not converge or resulted in flux values compatible with zero. The failure of these fits is likely explained by an inadequate description of the spectral shape of the excess. In Figure 5.9, the same residual significance map is also depicted split up in three energy bands. It is evident that the excess at the position of G2 is only significant in the range between 1.8 TeV and 5.6 TeV. In this energy range, the significance of diffuse emission exceeds a value of $5\,\sigma$. In higher and lower energies, no significant diffuse emission is visible.
Figure 5.10 depicts profiles along the right ascension axis for counts summed up along the declination axis within a spatial band through the region of the excess. This representation shows that the measured data is well described by the combined model of background and point sources. The residual excess between RA = $5^{\mathrm{h}}30^{\mathrm{m}}$ and RA = $5^{\mathrm{h}}40^{\mathrm{m}}$ can not be seen clearly in the plot for the middle energy range. This is likely the case because, in this representation, the data have not been correlated along the direction of right ascension.
In order to investigate the spectral shape of the excess, an energy-binned, counts-based residual analysis was carried out because spectral modelling via maximum likelihood fit was not possible as described above. In this analysis, the measured counts and

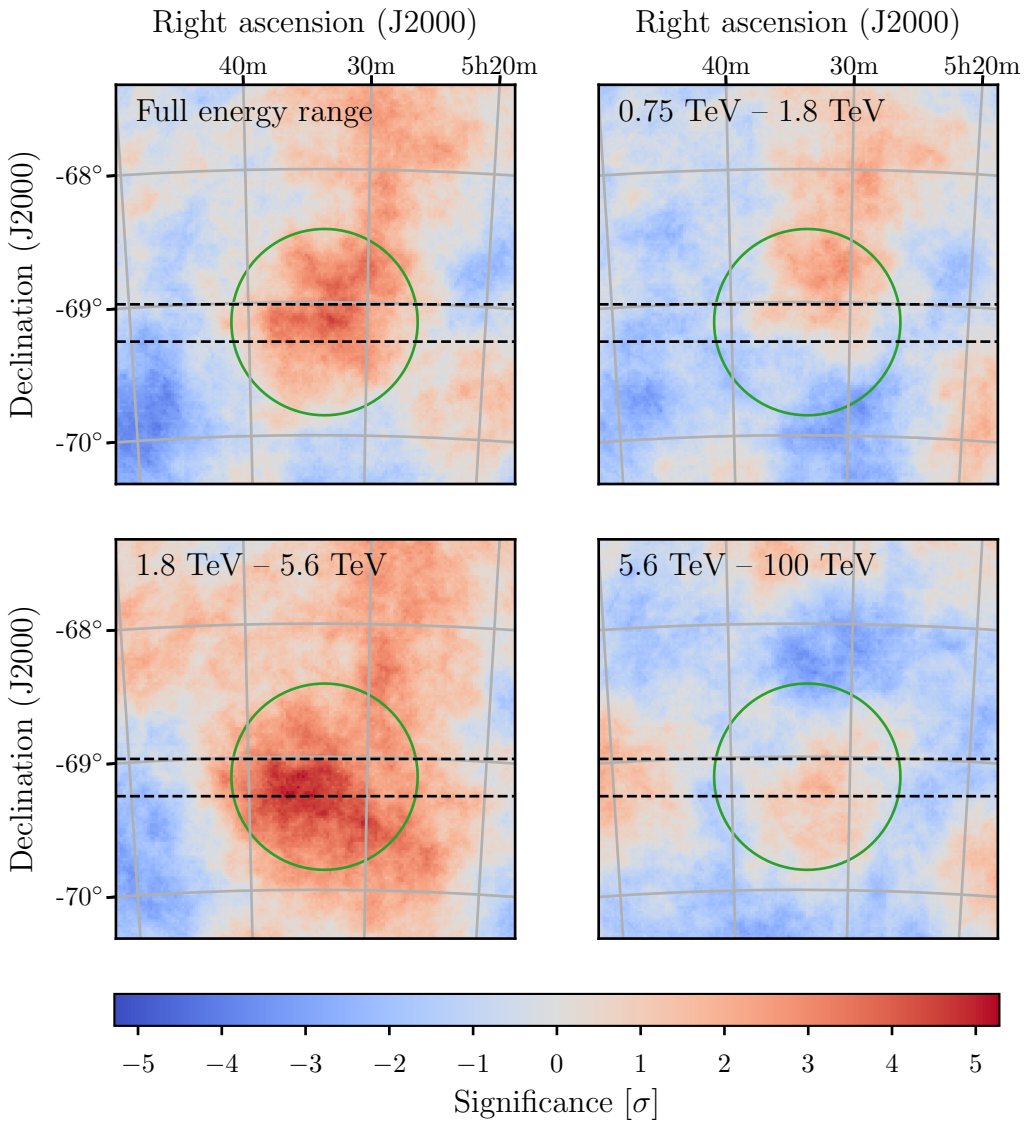

Figure 5.9: Residual significance maps of the region around 30 Dor after modelling of all point sources, divided into different energy bands. The top left plot shows the residiuals for the whole analysed energy range while the other plots depict the energy ranges that are given in the top left corners. Measured and modelled counts are correlated with a top-hat kernel of radius 0.5°. The green circle corresponds to the $1\,\sigma$ radius of region G2 where diffuse emission was detected with Fermi-LAT. The black dashed lines mark the band from which the data was used for generating the profile plots in 5.10.

the modelled counts within the G2 region were summed up for each energy bin. A spatially averaged exposure was also derived for each energy bin. From these values, energy binned flux values can be derived by subtracting model counts from measured counts and dividing by the mean exposure. The such derived flux points are plotted in Figure 5.11. For each flux point, the statistical significance, calculated via the Li & Ma formula, is also given. The 95 % confidence upper limits, derived with the algorithm introduced by Feldman et al. [1998] replace the flux points in the plot for all energy bins where the significance is below $2\,\sigma$. The high significance of the three flux points between 1.8 TeV and 10 TeV confirms the findings in the energy binned residual maps. Outside this energy range, no significant flux is detected. The upper flux limits at the high energy end of the spectrum are notably low. This is caused by the negative excess in this regime, which might be a hint for problems in the background description at the highest energies. The visible flux is in the order of magnitude of ~ (3–4) % of the background level, which can also be seen in the figure. The flux is also significantly lower than an extrapolation of the spectrum measured by Fermi-LAT predicts for the G2 region.

5.6 Limits of the analysis

This section is dedicated to systematic limitations of the counts based analysis of diffuse emission that was described above.
One of the main assumptions that were made in order to derive the flux points and upper limits is that the effective area and therefore also the effective exposure within each energy bin is well described by its mean value in this energy range. In Figure 5.11, it can be seen that this assumptions holds for high energies but becomes more and more incorrect when analysing lower energies. Below 1 TeV, the exposure varies very quickly with energy. Using the average exposure in the lowest energy band to calculate a residual flux from residual counts results in the lowest energetic events within this bin being scaled with a too large exposure. This in turn yields flux values and consequently also upper flux limits that are too small. For this reason, the upper limit in this low energy regime is plotted with reduced opacity in the spectral plot. This should imply that this upper limit is not to be trusted and is expected to be higher in reality than shown in the plot. Another source of errors for the calculated fluxes in the lower energy regime is the fact that the number of detected counts is also influenced by the different energy thresholds of the individual runs. The effect of cut off events is partially mitigated by appropriate weighting factors in the analysis but it can not be compensated completely on a bin-by-bin basis.
Another assumption that was made in the analysis is the correctness of the modelled background level. As discussed in detail in Mohrmann et al. [2019], the background template model is subject to uncertainties. To estimate the impact that a slightly higher or lower background level have on the results of the residual counts analysis, its normalisation was artificially both increased and decreased by 3 % from its best fit value. The value of 3 % was chosen because this corresponds to the deviation of the

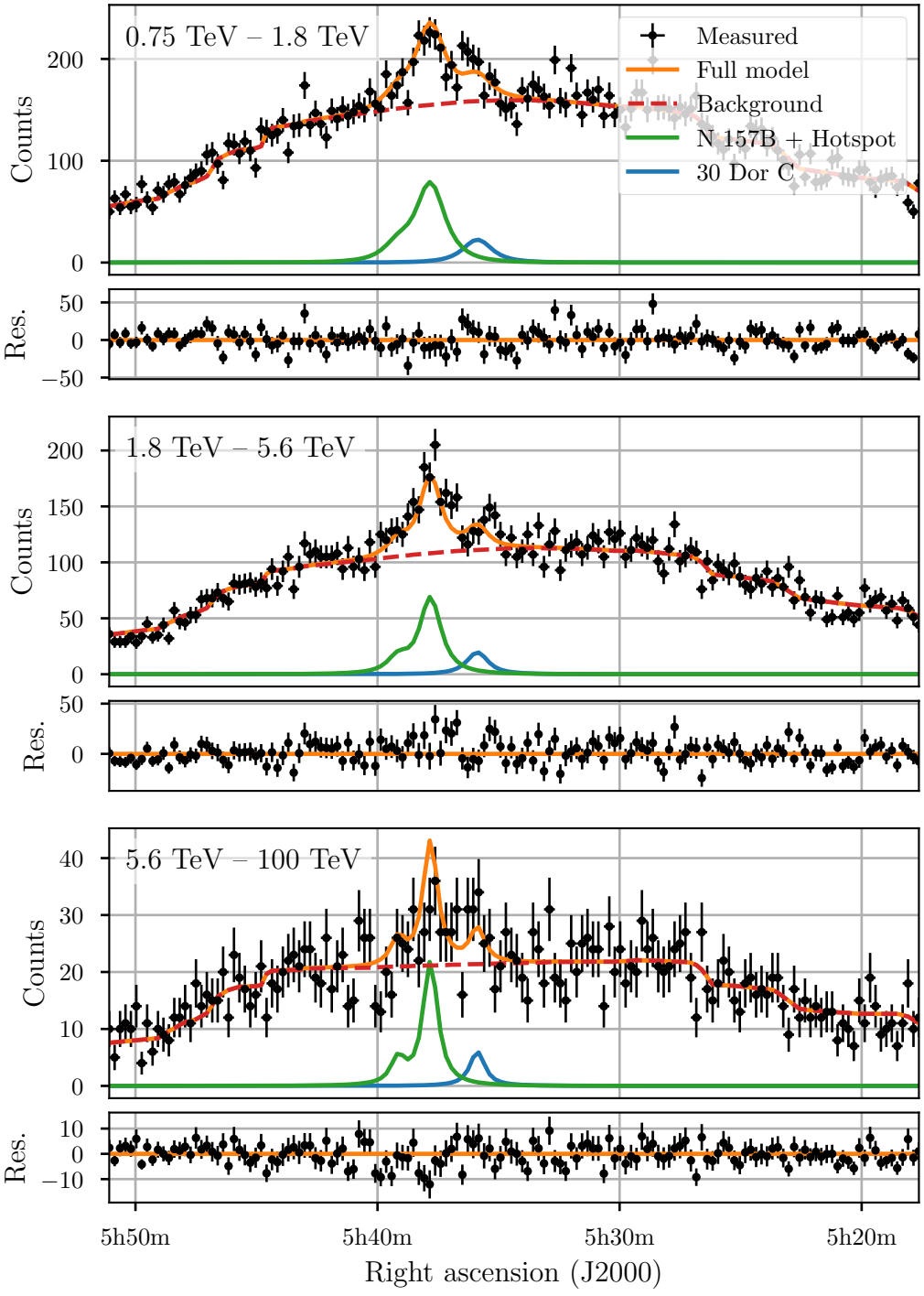

Figure 5.10: Profile plots for the spatial band indicated in Figure 5.9 that compare measured with modelled counts in three energy bands. The individual model components are shown as well as the complete model. The larger panels show the absolute values while the smaller ones visualise the residual counts that are obtained by subtracting modelled from the measured counts.

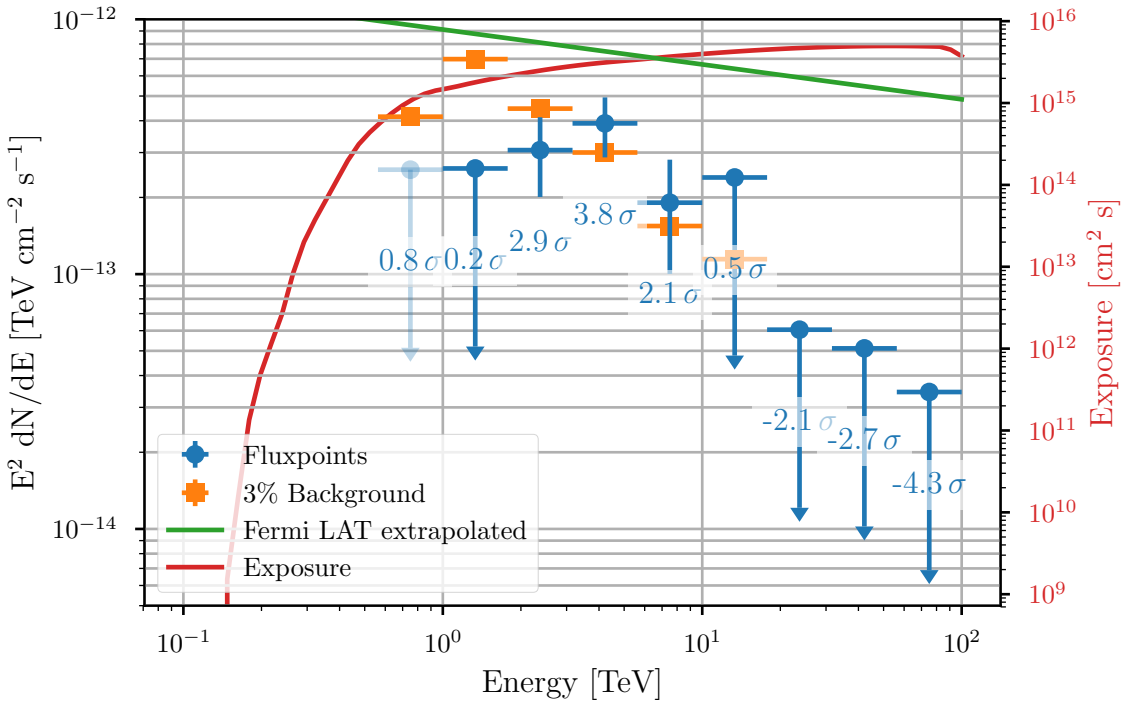

Figure 5.11: Energy spectrum for the diffuse emission excess derived for Fermi-LAT region G2 with a counts-based analysis. The statistical significance of the flux point is given for each energy bin. Fluxpoints with significances below $2\,\sigma$ are replaced by the corresponding upper limits at 95 % confidence level. The flux limit below 1 TeV is plotted with reduced opacity in order to indicate the large systematic uncertainties in this regime (see explanation in 5.6). The level of 3 % of the background is shown for comparison. The best fit power law spectrum of the diffuse emission measured with Fermi-LAT, extrapolated to TeV energies, is plotted as a green line. The red line depicts the effective exposure as a function of the energy.

mean fitted normalisation from unity (see Figure 5.8). The resulting spectra that were derived with these background levels are shown in Figure 5.12. It becomes clear that if the background normalisation is increased by 3 %, no more significant excess of diffuse emission is detected in any energy bin. In this case, the diffuse excess is completely absorbed by the background model. If, on the other hand, the background level is decreased by 3 %, the residual excess that can be interpreted as diffuse emission rises by a factor between 1.7 for high energies and 22 for low energies. The significances of the residual excess also rises. For example, in the energy bin (1.0 to 1.8) TeV, the significance rises to $5.4\,\sigma$.

This study shows that uncertainties in the background description have a significant impact on the result of the diffuse emission analysis. It could well be that the detected excess is simply caused by an error in the background template model, which leads to an underestimation of the background level in the maximum likelihood fit. It is also possible that the errors in the background template lead to an overestimation

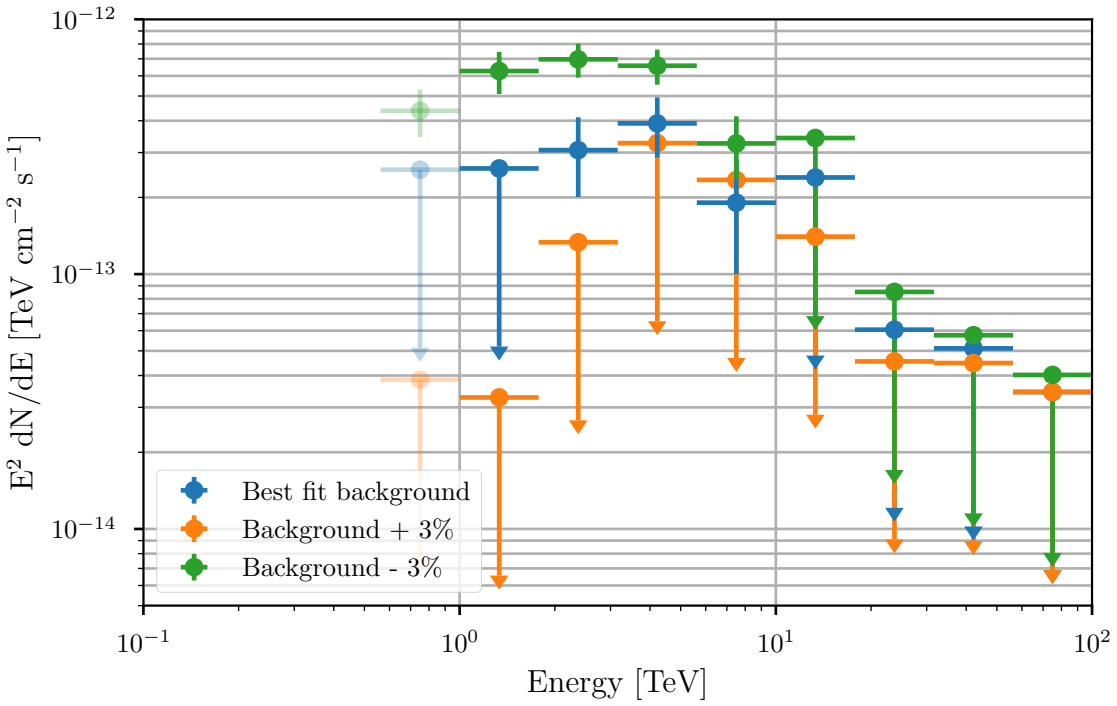

Figure 5.12: Energy spectrum from counts-based analysis like in Figure 5.11. The flux points and upper limits are added for a model description of the field of view where the background normalisation was artificially increased and decreased by 3 % starting at the best fit value.

of the background model in the fit, which might have absorbed parts of a physically present diffuse emission component. However, it should be noted that changing the background normalisation also had a strong influence on the results for the point sources in the analysis. Increasing the background by 3 % for example reduced the significance of LMC P3 to 4.4 σ. This proves that the point source analysis is also quite sensitive to the fitted background normalisation. Thus, the results of this analysis for the point sources, which are reasonably close the expectations, contradict the hypothesis of all diffuse excess being an artefact of incorrect background description. In the end, this can only be sorted out by further checks and refinements of the background template model.

5.7 Conclusion

In this chapter, the first analysis of the VHE gamma-ray emission form the Large Magellanic Cloud with the 3D likelihood analysis approach implemented in ctools has been presented. It was shown that this method provides a straightforward way to extract substantial scientific information from observation data of the dwarf galaxy in the close neighbourhood of the Milky Way.

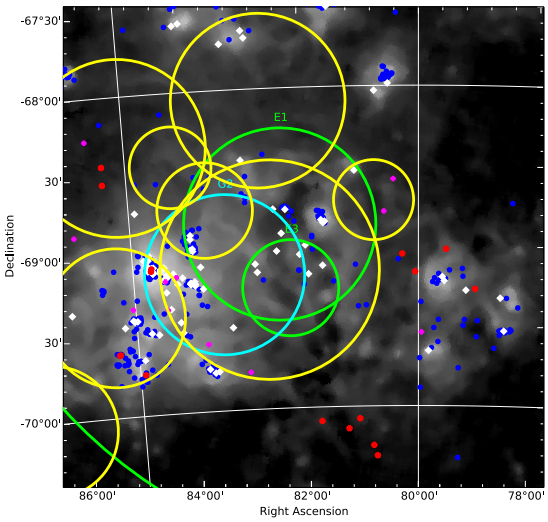

Figure 5.13: Layout of the vicinity of the G2 region, adapted from Ackermann et al. [2016]. The background pixel values correspond to a smoothed map of SHASSA Hα hydrogen line emission in logarithmic scale. The overlaid cyan circle indicates the analytic model component G2 for diffuse emission. The green circles mark the positions and $1\,\sigma$ extend of model components of an alternative diffuse emission model. Positions of known pulsars (magenta pluses), Wolf-Rayet stars (white diamonds), stars with spectral type B0-3 (blue dots), high mass x-ray binaries (red dots), and supergiant shells (yellow circles) are also indicated.

The results of the analysed point sources are, within some limitations, compatible with earlier analyses. A hotspot with a pre-trial significance of $5.1\,\sigma$ was found next to the position of N 157B. Due to its spectral similarity to the PWN, a model description as either an individual source or as a part of N 157B is possible for the hotspot. The residual uncertainties in the modelling of the point sources might be sorted out in future 3D likelihood analyses on event data that was reconstructed from raw data with ImPACT [Parsons et al. 2014], an advanced algorithm that provides a better angular resolution.
In the excess that remains after the emission of all modelled point sources has been subtracted, no unambiguous evidence for diffuse emission was found. Residual significance maps for different energy bands and a residual counts analysis showed some indication for a diffuse emission component at photon energies between 1.8 TeV and 10 TeV, spatially coincident with the region G2, where diffuse emission was detected at lower gamma-ray energies with Fermi-LAT. The maximum significant ($3.8\,\sigma$) diffuse excess was found in the energy interval (3.2 to 5.6) TeV with a mean differential flux of $(2.2 \pm 0.6) \times 10^{-14}\,\mathrm{cm}^{-2}\,\mathrm{s}^{-1}\,\mathrm{TeV}^{-1}$. Because of the missing excess at lower energies, a description of the diffuse emission with a model component and a corresponding maximum likelihood fit could not be carried out successfully.
Due to the measured excess being so low, it can not be ruled out that it is partially or entirely caused by systematic uncertainties in the description of the hadronic background with the applied template model. If the excess signal is of astrophysical

origin, it could be a hint for a cosmic-ray population within the 30 Dor region that interacts with interstellar gas and produces gamma rays up to the VHE regime. In Figure 5.13, it can be seen that high intensities of hydrogen line emission is detected close to the G2 region. This gas might serve as a target for hadronic interactions. An alternative explanation of the diffuse signal could be the combined flux from many individual sources which can not be resolved by the instrument. Candidates for such sources are pulsars, SNRs, and gamma-ray binaries, which are abundant in this active starforming region.
More information about a possible diffuse VHE gamma-ray emission from the LMC might become available in future studies of data taken with CTA, which will offer improved sensitivity in comparison to current experiments.

Bibliography

Aab, A., P. Abreu, M. Aglietta et al. (2018). 'An Indication of Anisotropy in Arrival Directions of Ultra-high-energy Cosmic Rays through Comparison to the Flux Pattern of Extragalactic Gamma-Ray Sources'. In: *The Astrophysical Journal* 853.2, p. L29. ISSN: 2041-8213. URL: http://dx.doi.org/10.3847/2041-8213/aaa66d.

Ackermann, M., A. Albert, W. B. Atwood et al. (2016). 'Deep view of the Large Magellanic Cloud with six years ofFermi-LAT observations'. In: *Astronomy & Astrophysics* 586, A71. ISSN: 1432-0746. URL: http://dx.doi.org/10.1051/0004-6361/201526920.

Aharonian, F., A. G. Akhperjanian, K. -M. Aye et al. (2004). 'Calibration of cameras of the H.E.S.S. detector'. In: *Astroparticle Physics* 22.2, pp. 109–125.

Aharonian, F., A. G. Akhperjanian, K. -M. Aye et al. (2005). 'Discovery of the binary pulsar PSR B1259-63 in very-high-energy gamma rays around periastron with HESS'. In: *A&A* 442.1, pp. 1–10. arXiv: astro-ph/0506280 [astro-ph].

Aharonian, F., A. G. Akhperjanian, A. R. Bazer-Bachi et al. (2006). 'Observations of the Crab nebula with HESS'. In: *A&A* 457.3, pp. 899–915. arXiv: astro-ph/0607333 [astro-ph].

Aharonian, Felix A. (2004). *Very High Energy Cosmic Gamma Radiation*. World Scientific Publishing Co. Pte. Ltd. ISBN: 0521387736.

Auger, Pierre, P. Ehrenfest, R. Maze et al. (1939). 'Extensive cosmic ray showers'. In: *Rev. Mod. Phys.* 11, pp. 288–291.

Axford, W. I., E. Leer and G. Skadron (1977). 'The Acceleration of Cosmic Rays by Shock Waves'. In: *International Cosmic Ray Conference*. Vol. 11. International Cosmic Ray Conference, p. 132.

Barrau, A., R. Bazer-Bachi, E. Beyer et al. (1998). 'The CAT imaging telescope for very-high-energy gamma-ray astronomy.' In: *Nuclear Instruments and Methods in Physics Research A* 416, pp. 278–292. eprint: astro-ph/9804046.

Bell, A. R. (1978). 'The acceleration of cosmic rays in shock fronts - I.' In: *MNRAS* 182, pp. 147–156.

Bentley, Jon Louis (1975). 'Multidimensional Binary Search Trees Used for Associative Searching'. In: *Commun. ACM* 18.9, pp. 509–517. ISSN: 0001-0782. URL: https://doi.org/10.1145/361002.361007.

Berezhko, E. G., L. T. Ksenofontov and H. J. Völk (2015). 'Re-examination of the Expected Gamma-Ray Emission of Supernova Remnant SN 1987A'. In: *ApJ* 810.1, 63, p. 63. arXiv: 1507.03760 [astro-ph.HE].

Berge, D., S. Funk and J. Hinton (2007). 'Background modelling in very-high-energy γ-ray astronomy'. In: *A&A* 466.3, pp. 1219–1229. arXiv: astro-ph/0610959 [astro-ph].

Bernlöhr, K., O. Carrol, R. Cornils et al. (2003). 'The optical system of the H.E.S.S. imaging atmospheric Cherenkov telescopes. Part I: layout and components of the system'. In: *Astroparticle Physics* 20, pp. 111–128. arXiv: astro-ph/0308246 [astro-ph].

Blandford, R. D. and J. P. Ostriker (1978). 'Particle acceleration by astrophysical shocks.' In: *ApJ* 221, pp. L29–L32.

Bolz, O. (2004). 'Absolute Energiekalibration der abbildenden Cherenkov-Teleskope des H.E.S.S. Experiments und Ergebnisse erster Beobachtungen des Supernova-Überrests RX J1713.7-3946'. PhD thesis. Heidelberg.

Bretz, T., H. Anderhub, M. Backes et al. (2013). 'FACT - The First G-APD Cherenkov Telescope: Status and Results'. In: *arXiv e-prints*, arXiv:1308.1512. arXiv: 1308.1512 [astro-ph.IM].

Buzhan, P., B. Dolgoshein, A. Ilyin et al. (2002). 'The Advanced Study of Silicon Photomultiplier'. In: *Advanced Technology - Particle Physics*. Ed. by M. Barone, E. Borchi, J. Huston et al., pp. 717–728.

Calabretta, Mark R. and Boudewijn F. Roukema (2007). 'Mapping on the HEALPix grid'. In: *Monthly Notices of the Royal Astronomical Society* 381.2, pp. 865–872. ISSN: 0035-8711. eprint: https://academic.oup.com/mnras/article-pdf/381/2/865/18575270/mnras0381-0865.pdf. URL: https://doi.org/10.1111/j.1365-2966.2007.12297.x.

Cherenkov, P. A. (1937). 'Visible Radiation Produced by Electrons Moving in a Medium with Velocities Exceeding that of Light'. In: *Physical Review* 52, pp. 378–379.

Corbet, R. H. D., L. Chomiuk, M. J. Coe et al. (2016). 'A LUMINOUS GAMMA-RAY BINARY IN THE LARGE MAGELLANIC CLOUD'. In: *The Astrophysical Journal* 829.2, p. 105. URL: https://doi.org/10.3847%2F0004-637x%2F829%2F2%2F105.

Cortina, J., M. Teshima and for the CTA Consortium (2015). 'Status of the Cherenkov Telescope Array's Large Size Telescopes'. In: *arXiv e-prints*, arXiv:1508.06438, arXiv:1508.06438. arXiv: 1508.06438 [astro-ph.IM].

Crampton, D., A. P. Cowley, I. B. Thompson et al. (1985). 'Further spectroscopy of LMC X-ray candidates.' In: *AJ* 90, pp. 43–48.

CTA Consortium (2019). *Science with the Cherenkov Telescope Array*.

Davies, John M. and Eugene S. Cotton (1957). 'Design of the quartermaster solar furnace'. In: *Solar Energy* 1, pp. 16–22.

Dickel, John R. and D. K. Milne (1995). 'Radio Properties of Three Young Supernova Remnants in the Large Magellanic Cloud'. In: *AJ* 109, p. 200.

Dubus, G. (2006). 'Gamma-ray binaries: pulsars in disguise?' In: *A&A* 456.3, pp. 801–817. arXiv: astro-ph/0605287 [astro-ph].

Dubus, Guillaume (2013). 'Gamma-ray binaries and related systems'. In: *A&A Rev.* 21, 64, p. 64. arXiv: 1307.7083 [astro-ph.HE].

Egelkraut, M. (2019). 'Analysis and Improvement of the Single-CCD Pointing-Image Simulation'. B.S. Thesis. Friedrich-Alexander-Universität Erlangen-Nürnberg.

Feldman, Gary J. and Robert D. Cousins (1998). 'Unified approach to the classical statistical analysis of small signals'. In: *Phys. Rev. D* 57.7, pp. 3873–3889. arXiv: physics/9711021 [physics.data-an].

Fender, Rob (2006). 'Jets from X-ray binaries'. In: *Compact stellar X-ray sources*. Vol. 39, pp. 381–419.

Fermi, Enrico (1949). 'On the Origin of the Cosmic Radiation'. In: *Physical Review* 75.8, pp. 1169–1174.

Funk, Stefan (2015). 'Ground- and Space-Based Gamma-Ray Astronomy'. In: *Annual Review of Nuclear and Particle Science* 65.1, pp. 245–277. eprint: https://doi.org/10.1146/annurev-nucl-102014-022036. URL: https://doi.org/10.1146/annurev-nucl-102014-022036.

Galbraith, W. and J. V. Jelley (1953). 'Light Pulses from the Night Sky associated with Cosmic Rays'. In: *Nature* 171, pp. 349–350.

Garczarczyk, Markus (2016). 'Status of the Medium-Sized Telescopes for the Cherenkov Telescope Array'. In: p. 959.

Giavitto, G., T. Ashton, A. Balzer et al. (2016). 'Upgraded cameras for the HESS imaging atmospheric Cherenkov telescopes'. In: *Ground-based and Airborne Instrumentation for Astronomy VI*. Vol. 9908. Proc. SPIE, 99082H.

Glicenstein, J. F., O. Abril, J. -A. Barrio et al. (2015). 'NectarCAM : a camera for the medium size telescopes of the Cherenkov Telescope Array'. In: *34th International Cosmic Ray Conference (ICRC2015)*. Vol. 34, p. 937. arXiv: 1508.06555 [astro-ph.IM].

Hahn, J., H. Gast, R. de los Reyes et al. (2013). *Heidelberg Data Quality Selection*. H.E.S.S. internal note.

Heitler, W. (1954). *Quantum theory of radiation*.

H.E.S.S. Collaboration, H. Abdalla, A. Abramowski et al. (2018a). 'Detection of variable VHE γ-ray emission from the extra-galactic γ-ray binary LMC P3'. In: *A&A* 610, L17, p. L17. arXiv: 1801.06322 [astro-ph.HE].

H.E.S.S. Collaboration, H. Abdalla, A. Abramowski et al. (2018b). 'H.E.S.S. observations of RX J1713.7-3946 with improved angular and spectral resolution: Evidence for gamma-ray emission extending beyond the X-ray emitting shell'. In: *A&A* 612, A6, A6. arXiv: 1609.08671 [astro-ph.HE].

H.E.S.S. Collaboration, A. Abramowski, F. Acero et al. (2012). 'Discovery of gamma-ray emission from the extragalactic pulsar wind nebula N 157B with H.E.S.S.' In: *A&A* 545, L2, p. L2. arXiv: 1208.1636 [astro-ph.HE].

H.E.S.S. Collaboration, A. Abramowski, F. Aharonian et al. (2014). 'Diffuse Galactic gamma-ray emission with H.E.S.S.' In: *Phys. Rev. D* 90 (12), p. 122007. URL: https://link.aps.org/doi/10.1103/PhysRevD.90.122007.

H.E.S.S. Collaboration, A. Abramowski, F. Aharonian et al. (2015). 'The exceptionally powerful TeV γ-ray emitters in the Large Magellanic Cloud'. In: *Science* 347.6220, pp. 406–412. arXiv: 1501.06578 [astro-ph.HE].

Hess, Victor F. (1912). 'Über Beobachtungen der durchdringenden Strahlung bei sieben Freiballonfahrten'. In: *Phys. Z.* 13, pp. 1084–1091.

Hillas, A. M. (1985). 'Cerenkov light images of EAS produced by primary gamma'. In: *International Cosmic Ray Conference* 3.

Hinton, J. and A. Mitchell (2018). *Pointing Requirements*. `https://indico.cta-observatory.org/event/1520/contributions/14966/attachments/13046/15513/PointingFeb18PC.pdf`. (Visited on 22/07/2020).

Hofmann, W., I. Jung, A. Konopelko et al. (1999). 'Comparison of techniques to reconstruct VHE gamma-ray showers from multiple stereoscopic Cherenkov images'. In: *Astroparticle Physics* 12.3, pp. 135–143. arXiv: `astro-ph/9904234 [astro-ph]`.

Høg, E., C. Fabricius, V. V. Makarov et al. (2000). 'The Tycho-2 catalogue of the 2.5 million brightest stars'. In: *A&A* 355, pp. L27–L30.

Holler, M., A. Balzer, Y. Becherini et al. (2013). 'Status of the Monoscopic Analysis Chains for H.E.S.S. II'. In: *arXiv e-prints*, arXiv:1307.6003, arXiv:1307.6003. arXiv: `1307.6003 [astro-ph.HE]`.

Horn, Roger A and Charles R. Johnson (1985). *Matrix Analysis*. Cambridge University Press.

Hughes, John P., Ichizo Hayashi and Katsuji Koyama (1998). 'ASCA X-Ray Spectroscopy of Large Magellanic Cloud Supernova Remnants and the Metal Abundances of the Large Magellanic Cloud'. In: *ApJ* 505.2, pp. 732–748. arXiv: `astro-ph/9802342 [astro-ph]`.

Johnson, Steven G. (2019). *The NLopt nonlinear-optimization package*. `http://github.com/stevengj/nlopt`. (Visited on 14/06/2020).

Kaelo, P. and Montaz Ali (2006). 'Some Variants of the Controlled Random Search Algorithm for Global Optimization'. In: *Journal of Optimization Theory and Applications* 130, pp. 253–264.

Kennel, C. F. and F. V. Coroniti (1984). 'Confinement of the Crab pulsar's wind by its supernova remnant.' In: *ApJ* 283, pp. 694–709.

Knödlseder, J., M. Mayer, C. Deil et al. (2016). 'GammaLib and ctools. A software framework for the analysis of astronomical gamma-ray data'. In: *A&A* 593, A1, A1. arXiv: `1606.00393 [astro-ph.IM]`.

Knödlseder, J., L. Tibaldo, D. Tiziani et al. (2019). 'Analysis of the H.E.S.S. public data release with ctools'. In: *A&A* 632, A102, A102. arXiv: `1910.09456`.

Komin, Nu., A. Djannati-Ataï, Y. Gallant et al. (2012). 'H.E.S.S. observations of the Large Magellanic Cloud'. In: *arXiv e-prints*, arXiv:1201.0639, arXiv:1201.0639. arXiv: `1201.0639 [astro-ph.HE]`.

Krymsky, G. F. (1977). 'Regular mechanism of charged particle acceleration on the shock wave front '. In: *Dokl. Akad. Nauk SSSR* 234.6, pp. 1306–1308.

Lang, Dustin, David W. Hogg, Keir Mierle et al. (2010). 'Astrometry.net: Blind Astrometric Calibration of Arbitrary Astronomical Images'. In: *AJ* 139.5, pp. 1782–1800. arXiv: `0910.2233 [astro-ph.IM]`.

Lennarz, D. (2012). 'A Study of Transient Very-High-Energy Gamma-Ray Emission from Gamma-Ray Bursts and Supernovae with H.E.S.S.' PhD thesis. Ruperto-Carola University of Heidelberg.

Li, Ti-Pei and YuQian Ma (1983). 'Analysis methods for results in gamma-ray astronomy'. In: *The Astrophysical Journal* 272, pp. 317–324.

Long, K. S., D. J. Helfand and D. A. Grabelsky (1981). 'A solf X-ray study of the Large Magellanic Cloud.' In: *ApJ* 248, pp. 925–944.

Longair, Malcolm S. (2011). *High Energy Astrophysics*. Vol. Third Edition. Cambridge University Press. ISBN: 0521387736.

Lorenz, E. and R. Wagner (2012). 'Very-high energy gamma-ray astronomy. A 23-year success story in high-energy astroparticle physics'. In: *European Physical Journal H* 37.3, pp. 459–513. arXiv: 1207.6003 [physics.hist-ph].

MAGIC Group (2020). *The MAGIC Telescopes*. https://magic.mpp.mpg.de. (Visited on 04/03/2020).

Mattox, J. R., D. L. Bertsch, J. Chiang et al. (1996). 'The Likelihood Analysis of EGRET Data'. In: *ApJ* 461, p. 396.

Mauch, T., T. Murphy, H. J. Buttery et al. (2003). 'SUMSS: a wide-field radio imaging survey of the southern sky - II. The source catalogue'. In: *MNRAS* 342.4, pp. 1117–1130. arXiv: astro-ph/0303188 [astro-ph].

Mayer, Michael (2015). 'Pulsar wind nebulae at high energies'. doctoralthesis. Universität Potsdam, p. 142.

Mirzoyan, R., R. Kankanian, F. Krennrich et al. (1994). 'The first telescope of the HEGRA air Cherenkov imaging telescope array'. In: *Nuclear Instruments and Methods in Physics Research Section A: Accelerators, Spectrometers, Detectors and Associated Equipment* 351.2, pp. 513–526. ISSN: 0168-9002. URL: http://www.sciencedirect.com/science/article/pii/0168900294913811.

Mohrmann, L., A. Specovius, D. Tiziani et al. (2019). 'Validation of open-source science tools and background model construction in γ-ray astronomy'. In: *A&A* 632, A72, A72. arXiv: 1910.08088 [astro-ph.IM].

Moulin, E., C. Diaz, D. Durand et al. (2015). 'Cooling Tests of the NectarCAM camera for the Cherenkov Telescope Array'. In: *arXiv e-prints*, arXiv:1509.04138, arXiv:1509.04138. arXiv: 1509.04138 [astro-ph.IM].

Naurois, Mathieu de and Loic Rolland (2009). 'A high performance likelihood reconstruction of γ-rays for imaging atmospheric Cherenkov telescopes'. In: *Astroparticle Physics* 32.5, pp. 231–252. arXiv: 0907.2610 [astro-ph.IM].

Nikolaev, S., A. J. Drake, S. C. Keller et al. (2004). 'Geometry of the Large Magellanic Cloud Disk: Results from MACHO and the Two Micron All Sky Survey'. In: *The Astrophysical Journal* 601.1, pp. 260–276. URL: https://doi.org/10.1086%2F380439.

Ohm, S., C. van Eldik and K. Egberts (2009). 'γ/hadron separation in very-high-energy γ-ray astronomy using a multivariate analysis method'. In: *Astroparticle Physics* 31.5, pp. 383–391. arXiv: 0904.1136 [astro-ph.IM].

Parsons, R. D. and J. A. Hinton (2014). 'A Monte Carlo template based analysis for air-Cherenkov arrays'. In: *Astroparticle Physics* 56, pp. 26–34. arXiv: 1403.2993 [astro-ph.IM].

Pence, W., J. K. Blackburn and E. Greene (1993). 'FTOOLS—A FITS Utility Package for Multiple Environments'. In: *Astronomical Data Analysis Software and Systems*

II. Ed. by R. J. Hanisch, R. J. V. Brissenden and J. Barnes. Vol. 52. Astronomical Society of the Pacific Conference Series, p. 541.

Pierre Auger Collaboration, A. Aab, P. Abreu et al. (2017). 'Observation of a large-scale anisotropy in the arrival directions of cosmic rays above 8×10^{18} eV'. In: *Science* 357.6357, pp. 1266–1270. arXiv: 1709.07321 [astro-ph.HE].

Pietrzyński, G., D. Graczyk, W. Gieren et al. (2013). 'An eclipsing-binary distance to the Large Magellanic Cloud accurate to two per cent'. In: *Nature* 495.7439, pp. 76–79. arXiv: 1303.2063 [astro-ph.GA].

Pühlhofer, G., C. Bauer, S. Bernhard et al. (2015). 'FlashCam: a fully-digital camera for the medium-sized telescopes of the Cherenkov Telescope Array'. In: *34th International Cosmic Ray Conference (ICRC2015)*. Vol. 34, p. 1039. arXiv: 1509.02434 [astro-ph.IM].

Pühlhofer, G., C. Bauer, A. Biland et al. (2012). 'FlashCam: A fully digital camera for CTA telescopes'. In: *American Institute of Physics Conference Series*. Ed. by Felix A. Aharonian, Werner Hofmann and Frank M. Rieger. Vol. 1505. American Institute of Physics Conference Series, pp. 777–780. arXiv: 1211.3684 [astro-ph.IM].

Rees, M. J. and J. E. Gunn (1974). 'The origin of the magnetic field and relativistic particles in the Crab Nebula'. In: *MNRAS* 167, pp. 1–12.

Rockwell, Ken (2014). *Nikon 50mm f/1.8 D Review*. https://www.kenrockwell.com/nikon/5018daf.htm. (Visited on 13/01/2020).

Scowcroft, Victoria, Wendy L. Freedman, Barry F. Madore et al. (2016). 'The Carnegie Hubble Program: The Distance and Structure of the SMC as Revealed by Mid-infrared Observations of Cepheids'. In: *ApJ* 816.2, 49, p. 49. arXiv: 1502.06995 [astro-ph.GA].

Sedov, L. I. (1959). *Similarity and Dimensional Methods in Mechanics*.

Seidelmann, P. and S. Urban (2010). 'Explanatory Supplement to the Astronomical Almanac, Third Edition'. In:

Smith, David A. and Q. Daniel Wang (2004). 'Confronting the Superbubble Model with X-Ray Observations of 30 Doradus C'. In: *ApJ* 611.2, pp. 881–891. arXiv: astro-ph/0405122 [astro-ph].

Taylor, Geoffrey (1950a). 'The Formation of a Blast Wave by a Very Intense Explosion. I. Theoretical Discussion'. In: *Proceedings of the Royal Society of London Series A* 201.1065, pp. 159–174.

Taylor, Geoffrey (1950b). 'The Formation of a Blast Wave by a Very Intense Explosion. II. The Atomic Explosion of 1945'. In: *Proceedings of the Royal Society of London Series A* 201.1065, pp. 175–186.

Tiziani, D. (2015). 'Investigations towards a Single-CCD Pointing-Solution for the Medium-Sized Telescopes of the Cherenkov Telescope Array'. MA thesis. Friedrich-Alexander-Universität Erlangen-Nürnberg.

Vaucouleurs, G. de, A. de Vaucouleurs and J. R. Corwin (1976). 'Second reference catalogue of bright galaxies'. In: *Second reference catalogue of bright galaxies* 1976.

Wang, Q. and D. J. Helfand (1991). 'The Detection of X-Ray Emission from the OB Associations of the Large Magellanic Cloud'. In: *ApJ* 373, p. 497.

Weekes, T. C., M. F. Cawley, D. J. Fegan et al. (1989). 'Observation of TeV gamma rays from the Crab nebula using the atmospheric Cerenkov imaging technique'. In: *ApJ* 342, pp. 379–395.

Wells, D. C. and E. W. Greisen (1979). 'FITS - a Flexible Image Transport System'. In: *Image Processing in Astronomy*. Ed. by G. Sedmak, M. Capaccioli and R. J. Allen, p. 445.

Whitney, B. A., M. Sewilo, R. Indebetouw et al. (2008). 'Spitzer Sage Survey of the Large Magellanic Cloud. III. Star Formation and ~1000 New Candidate Young Stellar Objects'. In: *AJ* 136.1, pp. 18–43.

Wilks, S. S. (1938). 'The Large-Sample Distribution of the Likelihood Ratio for Testing Composite Hypotheses'. In: *Ann. Math. Statist.* 9.1, pp. 60–62. URL: https://doi.org/10.1214/aoms/1177732360.

Wong, Y. (2018). 'Characterization and Optimization of a Single-CCD Concept for the Pointing of Medium-Sized Telescopes (MSTs) for the Cherenkov Telescope Array (CTA)'. MA thesis. Friedrich-Alexander-Universität Erlangen-Nürnberg.

Zinnecker, Hans (2003). *Formation of massive binaries*. arXiv: astro-ph/0301078 [astro-ph].

Danksagung

Natürlich wäre diese Arbeit nicht ganz ohne die Unterstützung von einigen lieben Kollegen möglich gewesen. Deshalb möchte ich mich an dieser Stelle bei Allen bedanken, die mich während meiner Arbeit am ECAP unterstützt haben. Mein ganz besonderer Dank gilt

- Herrn Prof. Dr. Christopher van Eldik. Vielen Dank, Christopher, dass Du mir diese Doktorarbeit ermöglicht hast. Vielen, vielen Dank auch für die zahlreichen konstruktiven Diskussionen, dass Du Dir stets Zeit genommen hast und für Deine Geduld.
- Der gesamten Erlanger Gamma-Gruppe für die tolle Arbeitsatmosphäre. Die gemeinsamen Pub-Abende, Tagungen, Ausflüge und vielen Diskussionen während der Mensabesuche weit über die Physik hinaus werden mir stets in Erinnerung bleiben.
- Lars für die hilfreichen Tipps und Diskussionen zum Thema 3D Likelihood Analyse und seine Zeit beim Korrekturlesen.
- Johannes für seine Unterstützung, vor allem bei technischen Problemen, für die gute Zusammenarbeit bezüglich MST Pointing und für das Korrekturlesen meiner Arbeit.
- Wun für die gute Zusammenarbeit im Büro und in der Targethalle bei den Tests des Gehäuse-Prototypen.
- Alex, der mir bezüglich der ctools-Analyse immer beratend zur Seite stand.
- Andi, meinem Bürokollegen, für die angenehme Atmosphäre und dass er nie zögerte, Probleme bei der Python- und C++-Programmierung zu besprechen.
- Markus Garczarczyk für seinen Einsatz bei den Prototypentests in Adlershof und auf La Palma.